

Quantum-Classical Correspondence in Two Simple Systems

by

Bradley Clarke Hughes

B.Sc., Dalhousie University, 1992

A THESIS SUBMITTED IN PARTIAL FULFILLMENT
OF THE REQUIREMENTS FOR THE DEGREE OF
MASTER OF SCIENCE
in the Department
of
Physics

© Bradley Clarke Hughes 1995
SIMON FRASER UNIVERSITY
August, 1995

All rights reserved. This work may be
reproduced in whole or in part, by photocopy
or other means, if it is attributed to the author.

APPROVAL

Name: Bradley Clarke Hughes
Degree: Master of Science
Title of thesis: Quantum-Classical Correspondence in Two Simple Systems

Examining Committee: Dr. J.R. Dahn
Chair

Dr. L.E. Ballentine
Senior Supervisor

Dr. D.H. Boal
Department of Physics

Dr. D. Loss
Department of Physics

Dr. J.L. Bechhoefer
Department of Physics

Date Approved: August 4, 1995.

PARTIAL COPYRIGHT LICENSE

I hereby grant to Simon Fraser University the right to lend my thesis, project or extended essay (the title of which is shown below) to users of the Simon Fraser University Library, and to make partial or single copies only for such users or in response to a request from the library of any other university, or other educational institution, on its own behalf or for one of its users. I further agree that permission for multiple copying of this work for scholarly purposes may be granted by me or the Dean of Graduate Studies. It is understood that copying or publication of this work for financial gain shall not be allowed without my written permission.

Title of Thesis/Project/Extended Essay

Quantum-Classical Correspondence in Two Simple Systems.

Author:

(signature)

Bradley C Hughes
(name)

August 14th 1995
(date)

Abstract

In this thesis, a comparison between quantum and classical mechanics was made for two systems whose classical behaviour can be chaotic. The general correspondence between classical mechanics and quantum mechanics in the classical regime has always been assumed but never proved. Recent research in the field of quantum chaos has brought this assumption into question. For some systems, such as the kicked rotor in the classically chaotic regime, quantum mechanics does not display the classical behaviour of unbounded momentum. It has been suggested that quantum mechanics will fail to produce classical chaos for a broad range of simple systems.

A comparison of quantum and classical mechanics was made using numerical simulations, without recourse to taking limits such as \hbar going to zero. The two systems studied were a driven pendulum and a pair of pendula joined by a spring. The quantum and classical expectation values for a number of observables were computed, as were the probability distributions in phase space. For periodic motion of the driven pendulum it was found that the theories agreed well for times up to 150 driving periods. Similar agreement was found for initial conditions whose classical behaviour was chaotic, but only for times up to a few tens of driving periods. For longer times, it was found that the quantum system displayed a boundedness in position and/or momentum that was absent in the classical system. A possible explanation was given in terms of the quasienergy expansion. In the coupled-pendula system no such disagreements between the theories were found.

Acknowledgments

I would like to thank Dr. Ballentine for his continued support during this project and his help in editing and revising this thesis. I would like to thank the members of my committee, Drs. Bechhoefer, Boal and Loss for their many suggestions. For many helpful discussions, I would like to thank Dominic Mimmagh and Jim Zibin. I also owe many thanks to Dominic for his repeated help with the figure-producing software. I am most grateful to my family for their support and lastly, I wish to give a mole of thanks to Tamara, Calliope, Morganna and Twoey.

To my parents.

Contents

Abstract	iii
Acknowledgments	iv
List of Tables	viii
List of Figures	ix
1 Introduction	1
1.1 Quantum Signatures of Classical Chaos	1
1.2 Semi-Classical Analysis of Quantum Chaos	2
1.3 Quantum and Classical Dynamics in Phase Space	3
1.4 Quasienergies and Momentum Localization	6
2 The Driven Pendulum System	8
2.1 The Classical Driven Pendulum	8
2.1.1 Classical Numerical Methods	9
2.1.2 Classical Dynamics	10
2.2 The Quantum Driven Pendulum	15
2.2.1 Quantum Numerical Methods	15
2.3 Quantum-Classical Comparison	17
2.3.1 The Classical Probability Distribution	17
2.3.2 The Quantum Husimi Distribution	18
2.3.3 Calculation of Expectation Values.	18
3 Results For the Driven Pendulum	20
3.1 Regular Dynamics	22
3.2 Chaotic and Resonant Dynamics	33
3.3 Application of Quasienergies to Results	49

4	Coupled Pendula	64
4.1	The Classical System	64
4.1.1	Classical Numerical Methods	66
4.1.2	Classical Dynamics	66
4.2	The Quantum System	77
4.2.1	Quantum Numerical Methods	77
4.2.2	Quantum-Classical Comparison	78
5	Results for the Coupled Pendula System	79
6	Conclusion	97

List of Tables

3.1	A summary of the results presented in sections 3.1 and 3.2 for the driven pendulum.	36
3.2	Magnitude and phase of $\langle U_T \rangle$ for various initial conditions when $\gamma = -.5$ and $\epsilon = 3$	62

List of Figures

2.1	The parametrically driven pendulum.	9
2.2	Poincaré section for the driven pendulum when $\gamma = -.5$ and $\epsilon = 3$. . .	11
2.3	The potential as a function of position and time for the driven pendulum where $\gamma = -.5$ and $\epsilon = 3$	12
2.4	Poincaré section for the resonant driven pendulum when $\gamma = -.5$ and $\epsilon = 2$	13
2.5	The potential as a function of position and time for the driven pendulum when $\gamma = -.5$ and $\epsilon = 2$	13
2.6	Poincaré section for the inverted driven pendulum. Here $\gamma = 36.3$ and $\epsilon = 11$	14
2.7	The potential as a function of position and time for the driven pendulum here $\gamma = 36.3$ and $\epsilon = 11$	14
3.1	Position and position-squared expectation values for ensembles centered at $(.1, 0)$ for $\gamma = -.5$ and $\epsilon = 3$	20
3.2	Momentum and momentum-squared expectation values for ensembles centered at $(.1, 0)$ for $\gamma = -.5$ and $\epsilon = 3$	21
3.3	Standard deviation of position and momentum for ensembles centered at $(.1, 0)$ for $\gamma = -.5$ and $\epsilon = 3$	21
3.4	Kinetic and total-energy expectation values for ensembles centered at $(.1, 0)$ for $\gamma = -.5$ and $\epsilon = 3$	22
3.5	Quantum probability distributions for the ensemble in Figure 3.1 for times = 0, 1, 100, and 150 periods.	23

3.6	Classical probability distributions for the ensemble in Figure 3.1 for times = 0, 1, 100, and 150 periods.	24
3.7	Position and position-squared expectation values for the ensembles centered at (1.7, 3) for $\gamma = -.5$ and $\epsilon = 3$	25
3.8	Momentum and momentum-squared expectation values for the ensembles centered at (1.7, 3) for $\gamma = -.5$ and $\epsilon = 3$	25
3.9	Standard deviations for momentum and position expectation values for quantum and classical ensembles centered at (1.7, 3) for $\gamma = -.5$ and $\epsilon = 3$	26
3.10	Potential and total-energy expectation values for quantum and classical ensembles centered at (1.7, 3) for $\gamma = -.5$ and $\epsilon = 3$	26
3.11	Quantum probability distributions for time = 0,1,100, and 150 drive cycles for the same ensemble as Figure 3.7.	27
3.12	Classical probability distributions for time = 0,1,100, and 150 drive cycles for the same ensemble as Figure 3.7.	28
3.13	Expectation values for position and position squared for ensembles centered at (0, 0) for $\gamma = 36.3$ and $\epsilon = 11$	29
3.14	Expectation values for momentum and momentum squared for ensembles centered at (0, 0) for $\gamma = 36.3$ and $\epsilon = 11$	30
3.15	Standard deviations for position and momentum for ensembles centered at (0, 0) for $\gamma = 36.3$ and $\epsilon = 11$	30
3.16	Kinetic and total-energy expectation values for quantum and classical ensembles centered at (0, 0) for $\gamma = 36.3$ and $\epsilon = 11$	31
3.17	Expectation values for position and position squared for quantum and classical ensembles centered at $(\pm\pi, 0)$ for $\gamma = 36.3$ and $\epsilon = 11$	31
3.18	Expectation values for momentum and momentum squared for quantum (large dots) and classical (small dots) ensembles centered at $(\pm\pi, 0)$ for $\gamma = 36.3$ and $\epsilon = 11$	31
3.19	Standard deviation of position and momentum for quantum and classical ensembles centered at $(\pm\pi, 0)$ for $\gamma = 36.3$ and $\epsilon = 11$	32

3.20	Expectation values of kinetic and total energy for quantum and classical ensembles centered at $(\pm\pi, 0)$ for $\gamma = 36.3$ and $\epsilon = 11$	32
3.21	Position and position-squared expectation values for quantum and classical ensembles centered at $(-1, 1.7)$ for the simple pendulum.	33
3.22	Momentum and momentum-squared expectation values for quantum and classical ensembles centered at $(-1, 1.7)$ for the simple pendulum.	34
3.23	The standard deviations for position and momentum for the quantum and classical ensembles centered at $(-1, 1.7)$ for the simple pendulum.	34
3.24	The expectation values of kinetic and total energy for quantum and classical ensembles centered at $(-1, 1.7)$ for the simple pendulum.	35
3.25	Quantum probability distributions for the same ensemble as Figure 3.21.	35
3.26	Classical probability distributions for the same ensemble as Figure 3.21.	36
3.27	Expectation values for position and position squared for ensembles that were initially centered at $(-3, -1.7)$ and $\gamma = -.5$ and $\epsilon = 3$	37
3.28	Expectation values for momentum and momentum squared. The ensembles were initially centered at $(-3, -1.7)$ and $\gamma = -.5$ and $\epsilon = 3$	37
3.29	The standard deviations for position and momentum. The ensembles were initially centered at $(-3, -1.7)$ and $\gamma = -.5$ and $\epsilon = 3$	38
3.30	Expectation values for kinetic and total energy. The ensembles were initially centered at $(-3, -1.7)$ and $\gamma = -.5$ and $\epsilon = 3$	39
3.31	Quantum probability distributions for time = 0, 1, 4 and 8 drive cycles for the same ensemble as in Figure 3.27.	40
3.32	Quantum probability distributions for time = 16, 48, 100, and 150 drive cycles for the same ensemble as in Figure 3.27	41
3.33	Classical probability distributions for time = 0, 1, 4 and 8 drive cycles for the same ensemble as in Figure 3.27.	42
3.34	Classical probability distributions for time = 16, 48, 100 and 150 drive cycles for the same ensemble as in Figure 3.27.	43
3.35	Expectation values for position and position squared for quantum and classical ensembles centered at $(-2.3, 0)$ for $\gamma = -.5$, $\epsilon = 3$ and $c = 100$	43

3.36	Expectation values for momentum and momentum squared for the same ensemble as Figure 3.35.	44
3.37	Expectation values for the standard deviation of position and momentum for the same ensemble as Figure 3.35.	44
3.38	Expectation values for potential and total energy for the same ensemble as in Figure 3.35.	44
3.39	Quantum probability distributions for time = 0, 1, 4, 8 drive cycles for the ensemble centered at $(-2.3, 0)$ for $\gamma = -.5$, $\epsilon = 3$ and $c = 100$	45
3.40	Quantum probability distributions for time = 16, 48, 100, and 150 drive cycles for the same ensembles as in Figure 3.39.	46
3.41	Classical probability distributions for time = 0, 1, 4, and 8 drive cycles for the same ensembles as in Figure 3.39.	47
3.42	Classical probability distributions for time = 16, 48, 100, and 150 drive cycles for the same ensembles as in Figure 3.39.	48
3.43	Position and position-squared expectation values for quantum and classical ensembles centered at $(-2.3, 0)$ for $\gamma = -.5$, $\epsilon = 3$ and $c = 250$	48
3.44	Momentum and momentum-squared expectation values for the same ensembles as Figure 3.43.	49
3.45	Momentum and position standard deviations for the same ensembles as Figure 3.43.	49
3.46	Potential and total energy for the same ensembles as Figure 3.43. . . .	50
3.47	Expectation values of position and position squared for quantum and classical ensembles centered at $(-2.3, 0)$ for $\gamma = -.5$, $\epsilon = 3$ and $c = 50$	50
3.48	Expectation values of momentum and momentum squared for the ensembles centered at $(-2.3, 0)$ for $\gamma = -.5$, $\epsilon = 3$ and $c = 50$	51
3.49	Standard deviations for momentum and position for the ensembles centered at $(-2.3, 0)$ for $\gamma = -.5$, $\epsilon = 3$ and $c = 50$	51
3.50	Potential and total energy for the same ensembles as Figure 3.49. . . .	52
3.51	Expectation values of position and position squared for quantum and classical ensembles centered at $(0, 0)$ for $\gamma = -.5$, $\epsilon = 2$ and $c = 100$	52

3.52	Expectation values of momentum and momentum squared for the ensembles centered at (0,0) for $\gamma = -.5$, $\epsilon = 2$ and $c = 100$	52
3.53	Standard deviations for position and momentum for the ensembles centered at (0,0) for $\gamma = -.5$, $\epsilon = 2$ and $c = 100$	53
3.54	Expectation values for kinetic and total energy for the same ensembles centered at (0,0) for $\gamma = -.5$, $\epsilon = 2$ and $c = 100$	53
3.55	Quantum probability distributions for the ensemble centered at (0,0) for $\gamma = -.5$, $\epsilon = 2$ and $c = 100$	54
3.56	Quantum probability distributions for the same ensemble as Figure 3.55.	55
3.57	Classical probability distributions for the same ensemble as Figure 3.55.	56
3.58	Classical probability distributions for the same ensemble as Figure 3.57.	57
3.59	Position and position-squared expectation values for quantum and classical ensembles centered at (0,0) for $\gamma = -.5$, $\epsilon = 3$ and $c = 250$	57
3.60	Momentum and momentum-squared expectation values for the same ensemble as Figure 3.59.	58
3.61	Standard deviation of position and momentum for the same ensemble as Figure 3.59.	58
3.62	Kinetic and total energy expectation values for the same ensemble as Figure 3.59.	59
3.63	Expectation values of position and position-squared for quantum and classical ensembles centered at (0,0) for $\gamma = -.5$, $\epsilon = 3$ and $c = 50$	59
3.64	Expectation values of momentum and momentum-squared for the same ensembles as Figure 3.63.	60
3.65	Standard deviations for position and momentum for the same ensemble as Figure 3.63.	60
3.66	Kinetic and total energy expectation values for the same ensembles as Figure 3.63.	60
4.1	The coupled pendula system.	65
4.2	Poincaré section for the coupled pendula system when $\alpha = .9$, $\beta = 1.4$, $\gamma = .6$, $\delta = 1.6$, $e = 1.7$	67


4.3	Potential for the coupled pendula system with the same parameters as in Figure 4.2.	68
4.4	A random dot stereogram of the coupled pendula potential. The image may be seen by focusing one's eyes behind the page. An inside-out image may be seen by focusing in front of the page. The axes run from $-\pi$ to π , y_1 runs from left to right and y_2 from bottom to top.	69
4.5	Quasi-periodic trajectory with initial conditions $y_1 = .3$, $y_2 = .36$, $p_1 = p_2 = 0$	70
4.6	Chaotic trajectory with initial conditions $y_1 = .5$, $y_2 = -1.5$, $p_1 = p_2 = 0$	71
4.7	Chaotic trajectory with initial conditions $y_1 = 2.0$, $y_2 = .38$, $p_1 = p_2 = 0$	72
4.8	Quasi-periodic trajectory with initial conditions $y_1 = 1.7$, $y_2 = -.3$, $p_1 = .5$, $p_2 = 0$	73
4.9	Quasiperiod 3 trajectory with initial conditions $y_1 = -1.8$, $y_2 = -.4$, $p_1 = -.6$	74
4.10	Quasi-periodic trajectory with initial conditions $y_1 = -2.0$, $y_2 = -.66$	75
4.11	A section through the quasi-periodic trajectory shown in Figure 4.10. The slice is taken when $y_1 = 1.85$ and $\dot{y}_1 > 0$	76
5.1	The position and position squared expectation values calculated for classical and quantum ensembles initially centered at $(-2.0, -.66)$, in the quasiperiodic regime, with zero average momentum as a function of time. The large dots are the quantum values and the small dots are the classical values.	80
5.2	The expectation values of momentum and momentum squared, calculated for the quasiperiodic ensembles in Figure 5.1	81
5.3	The standard deviations for position and momentum, calculated for the quasiperiodic ensembles in Figure 5.1	82
5.4	The potential, kinetic, and total energy expectation values, calculated for the quasiperiodic ensembles in Figure 5.1	83

5.5	The position and position squared expectation values calculated for classical and quantum ensembles, initially centered in the chaotic regime at $(.5, -1.5)$ in position, with zero average momenta, as a function of time. The large dots are the quantum values and the small dots are the classical values.	85
5.6	The momentum and momentum squared expectation values calculated for the same chaotic ensembles as in Figure 5.5.	86
5.7	The standard deviations of position and momentum expectation values calculated for the same chaotic ensembles as in Figure 5.5. The large dots are the quantum values and the small dots are the classical ensembles.	87
5.8	The expectation values for potential, kinetic, and total energy for the same chaotic ensembles as in Figure 5.5.	88
5.9	The probability distributions in position space for the quasiperiodic quantum ensemble centered at $(-2.0, -.66)$ This is for time = 0, 1, 2, and 4 periods. The time ordering is from right to left and from top to bottom. The position expectation values are shown in Figure 5.1. The black represents .2 of the initial greatest probability. Zero probability is white. The same grey scale scheme is used for all the probability distributions in this chapter.	89
5.10	More probability distributions in position space for the quantum ensemble centered in the quasiperiodic regime at $(-2.0, -.66)$ This is for time = 10, and 32 periods. The position expectation values are shown in Figure 5.1.	90
5.11	The probability distributions in position space for the classical ensemble centered in the quasiperiodic regime at $(-2.0, -.66)$ This is for time = 0, 1, 2, and 4 periods. The position expectation values are shown in Figure 5.1.	91

5.12	More probability distributions in position space for the classical ensemble centered at $(-2.0, -0.66)$ in the quasiperiodic regime. This is for time = 10, and 32 periods. The position expectation values are shown in Figure 5.1.	92
5.13	The probability distributions in position space for the quantum ensemble centered in the chaotic regime at $(.5, -1.5)$ This is for time = 0, 1, 2, and 4 periods. The time ordering is from left to right and from top to bottom. The position expectation values are shown in Figure 5.5.	93
5.14	More probability distributions in position space for the chaotic quantum ensemble centered at $(.5, -1.5)$ Reading from left to right this is for time = 10 and 32 periods. The position expectation values are shown in Figure 5.5.	94
5.15	The probability distributions in position space for the chaotic classical ensemble centered at $(.5, -1.5)$ Reading from left to right and top to bottom, this is for time = 0, 1, 2, and 4 periods. The position expectation values are shown in Figure 5.5.	95
5.16	More probability distributions in position space for the classical ensemble centered at $(.5, -1.5)$ This is for time = 10, and 32 periods. The position expectation values are shown in Figure 5.5.	96

Chapter 1

Introduction

he study of dynamical chaos has spread with an exponential growth akin to that which characterizes the model systems with which it began. Over the last ten years, this spread has entered the realms of quantum physics, gradually coagulating into the recognized field of “quantum chaos”. In this domain, the interest has been in determining which, if any, features of dynamical chaos survive quantization. Given the differences in the two theories, what will chaos look like in a quantum system? Reversing this approach, can classical chaos be described by quantum mechanics? It is this question which this thesis addresses.

There have been numerous approaches to these questions: the search for quantum “signatures” of classical chaos; the use of semi-classical approximations, and direct comparison of classical and quantum mechanics in phase space and/or via expectation values.

1.1 Quantum Signatures of Classical Chaos

Signatures of classical chaos have been found in quantum energy eigenfunctions, via Ehrenfest’s theorem, and in the phase of the wavefunction. The study of energy eigenfunctions has been used for the stadium potential [1] and coupled quartic oscillators.[2][3] The stadium potential is shaped like a rectangle with semi-circular ends. The potential is constant inside and infinite on the boundary. For appropriate

choices of the lengths of the sides, the classical phase space consists of chaos interspersed with unstable periodic trajectories. The quantum energy eigenfunctions fill the entire area in position space, as do the classical chaotic orbits. The eigenfunctions also reveal increased probability, or “scars,” along some of the unstable periodic orbits within the chaotic regime. This scarring is also seen in the coupled quartic oscillator potential.[2][3] It is taken as a general quantum signature of classical chaos.[4]

Ehrenfest’s theorem has also been used to identify quantum chaos. It was found that in the chaotic regime of the anharmonic oscillator, Ehrenfest’s theorem holds for much shorter times than it does in the regular regime of the system.[5][6]

Randomness of the phase of the wave function in the Husimi representation (see section 2.3.2) has also been used as an indicator of chaos. This randomness occurs because the classical stretching and folding of phase space causes the wavefunction to overlap itself. The resulting interference serves to randomize the phase of the wave function in the Husimi representation.[7] It has also been shown that wavefunctions in the classically chaotic regime are more sensitive to perturbations than in the regular regime.[8]

1.2 Semi-Classical Analysis of Quantum Chaos

Semi-classical analysis builds on the work of Gutzwiller.[9] Semi-classical approximations are based on integrating along a number of classical paths to determine a quantum probability distribution. This process works well for classically regular dynamics. A number of systems have been explored to determine means of making such approximations in the chaotic regime. Such systems include: coupled quartic oscillators[2] and a driven cosine potential that is not a pendulum due to the absence of periodic boundary conditions.[10][11] In the driven cosine potential, Helmkamp and Browne were able to show that the quantum interference effects in the neighbourhood of a fixed point are due to a beating phenomenon between semi-classical paths. This interference is seen in the systems that were studied in this thesis. The semi-classical approach is not used in this thesis in favour of simply comparing quantum mechanics and classical mechanics without any approximations.

1.3 Quantum and Classical Dynamics in Phase Space

Ford has suggested that quantum mechanics should be used to calculate the results of a purely classical experiment. This would determine any differences between quantum and classical predictions of behaviour in the *classical* regime.[12] Using algorithmic complexity as the measure of chaos in both the classical and chaotic cases, he demonstrates that “eigenvalues, eigenfunctions, and time development of wavefunctions in finite, bounded, undriven systems cannot be chaotic.”[12][13][14] The algorithmic-complexity argument amounts to describing the rate of loss of precision in one’s knowledge of the system as a function of time. Put the other way around, a chaotic or algorithmically-complex system will require as many, or more, digits of precision in specifying the initial conditions than will be retained in the final answer. He concludes from this that the quantum description of a classically chaotic system cannot contain chaos, contrary to the classical description. To see why this lack of chaos may be so, consider the bound wavefunction as a finite superposition of energy eigenfunctions:

$$\psi(x, t) = \sum_E e^{-iEt/\hbar} A_E \phi_E(x) \quad (1.1)$$

Here, the $\phi_E(x)$ are the energy eigenfunctions with eigenvalue E , and the A_E are the expansion coefficients of the wavefunction at time $t = 0$. The wavefunction is then doomed to motion that is at most quasiperiodic; it can never be chaotic. There is no exponential loss of precision in the time-dependent exponential, as there must be for chaotic motion.

The Arnol’d cat map is a mapping of the unit square onto itself. Imposing periodic boundary conditions, and taking the axes to represent position and momentum, turns this mapping into a classically chaotic system. The cat map is an example of the lack of quantum chaos, in that, for the correct choice of parameters, the quasiperiodic quantum wavefunction returns nearly to its initial state in as little as 12 iterations of the map.[14] When the Arnol’d cat mapping is taken, instead, from two position axes onto themselves, the quantum and classical descriptions no longer show the disagreement found by Ford.[15]

Ford's argument makes the assumption that the chaotic motion of a single trajectory can be compared to that of a wavefunction. It has been shown that both theories lose precision at a similar rate, if one demands that the accuracy of a position measurement be the same for both.[6] The demand for a comparison of the two formalisms on a single classical system is, however, a valid one. If quantum mechanics is a more complete portrayal of experimental reality than classical mechanics, it should give correct predictions for a simple, few-degrees-of-freedom, classical system.

Some of the systems that have been investigated include the kicked rotor and coupled rotors (both mentioned below), the kicked top [16], the kicked pendulum [17], the discrete quantum pendulum [18], the double kicked rotor [19], the Arnol'd cat map [14], the Arnol'd cat map acting only on two position co-ordinates [15], driven cosine potential [11], driven double-well oscillator [20] and the driven anharmonic oscillator[21][6].

In their analysis of the kicked top [16] and the kicked pendulum [17], Fox and Elston have shown that for a sharply peaked Gaussian wavefunction, its initial growth, in phase space, is related to the Lyapunov exponents of the classical trajectories. They also found that both quantum and classical theories agree well with each other up until the large scale occurrence of quantum interference. Similar results, regarding the time at which disagreement begins, were found in the case of the driven cosine potential.[11] This behaviour was also seen in the two systems that were studied in this thesis.

For the discrete pendulum mapping, it has been shown that the eigenfunctions of the Hamiltonian fill regions in phase space similar to that of the classical trajectories.[18]

For a driven double-well oscillator, the expectation values of quantum dynamical variables, such as the energy and the position, demonstrate quasiperiodic and irregular time series. The former occurs for initially Gaussian wavefunctions localized in the periodic area, and the latter occurs in the chaotic area of phase space. Quantum tunnelling between islands of periodicity in the chaotic sea was also observed.[20] Such time series will be presented in this thesis also.

Much research has been devoted to the driven anharmonic oscillator.[6][21][22] The classical phase space of this system (for the parameter values studied) consists of an

island of regular orbits within a sea of chaos which is itself surrounded by periodic orbits. Ben-Tal *et. al.* found that chaotic spreading was observed for both quantum and classical mechanics in the chaotic regime.[21][22] Comparing the two theories in phase space, Zibin found that both quantum and classical expectation values and probability distributions agreed well with each other for short times in the regular and chaotic regime. In the regular case, they also agreed well for long times. There was disagreement between the theories for the chaotic case that decreased as the classical regime was approached. The approach to classicality was made by varying the value of a scaled \hbar . [6] This approach was also used in this thesis.

The method that was followed in this thesis was that of Ford[13], Fox[16][17], Helmkamp[10], and Ben-Tal[21], which is to compare quantum and classical mechanics directly in phase space without the use of any limiting procedures or approximations. Two systems were investigated by numerically solving the classical and quantum equations of motion. The probability distributions and expectation values were compared. The first system, a one-degree-of-freedom parametrically driven pendulum, is introduced in chapter 2. This system was chosen for its simplicity and its absence from the literature on quantum chaos. The numerical methods and equations of motion for this system in both theories are outlined therein. The third chapter details the numerical investigation and presents the results. The second system studied was two-dimensional and energy conserving: a pair of pendula coupled by a linear massless spring. This simple, chaotic, conservative system is also absent from the literature. The equations of motion and the numerical methods for the coupled pendula system are given in chapter 4. The penultimate chapter concerns itself with the results of this numerical investigation. Unsurprisingly, the final chapter contains a summary of the results and the conclusions to be drawn from them. The remainder of this chapter explains quasienergies, which were useful in the discussion of the kicked rotor[23], and will help to explain some of the behaviour of the driven pendulum.

1.4 Quasienergies and Momentum Localization

In quantum chaos, one of the first, and most popular systems has been the kicked rotor.[23][24][25] In the classical system there is a regime where the momentum increases unboundedly with each kick. In the quantum system this momentum diffusion is not observed.[23] The explanation for this disagreement stems from a mapping of this system to Anderson localization in a disordered crystal. Here, the momentum is localized as a purely quantum effect, just as the position of electrons is localized in a random crystal. Similar difficulties have been encountered in other systems, such as the double kicked rotor.[19] This disagreement has been found to disappear upon including measurement[26], more degrees of freedom[24][26], and by coupling the system to an environment[27][28] or to another kicked rotor[24].

This momentum localization is not always observed in chaotic systems. One such system which does not display this phenomena is the periodically driven anharmonic oscillator.[21][22][6] This localization is best explained using the quasienergy representation, which will be elaborated on below.

In the analysis of classical time-independent Hamiltonian systems, it is often useful to plot trajectories in phase space. This is especially true in systems with one spatial degree of freedom. The resulting plot of position and its conjugate momentum resides entirely in two dimensions. A single trajectory in this space will be composed of a collection of points that all have the same energy. This ensemble then must have some equivalence to the quantum energy eigenstates. (For a numerical exploration of a few such states see reference [18].) When moving to periodic time-dependent Hamiltonians, one often uses a Poincaré section to display the dynamics of the system in two dimensions. (See, for example, Figure 2.2.) A trajectory in this section will be mapped back onto itself after one period. Considered as classical ensembles, each of the lines and blotches that cover this plot have as their natural quantum analog the eigenfunctions of the one-period time-development operator (U_T).

The quasienergy eigenfunctions are these eigenstates. They are the solutions to Schrödinger's equation which have the same periodicity, up to a constant phase, as the Hamiltonian. Formally: consider a Hamiltonian with period T so that $H(t) = H(t +$

T). The one-period time-development operator is designated U_T . The quasienergy eigenfunctions are then such that

$$U_T \psi_u(x) = e^{-iu} \psi_u(x) \quad (1.2)$$

where $E = \hbar u/T$ is the quasienergy of $\psi_u(x)$. This is a restatement of Floquet's theorem for a potential which is periodic in time rather than space. An arbitrary wavefunction at time t may be expanded in terms of the quasienergy eigenfunctions:

$$\Psi(x, t) = \sum_E e^{-iEt/\hbar} A_E \psi_E(x, t) \quad (1.3)$$

Here, the A_E are the expansion coefficients for $\Psi(x, 0)$. [29] As in the case of a time-independent Hamiltonian, the behaviour of a wavefunction, whose quasienergy spectrum is discrete, can be no more complex than quasiperiodic.

The boundedness in momentum of the quantum kicked rotor may now be explained by the use of quasienergies. For the kicked rotor it has been shown that the quasienergy-eigenfunctions are localized in momentum space. [25] The momenta of the quantum system are bounded because of the localization of the quasienergy eigenfunctions. Any momenta that are not included in the initial distribution of quasienergies will never be reached by the dephasing of the wavefunction with time. This argument will be used in the discussion of the driven pendulum.

Chapter 2

The Driven Pendulum System

2.1 The Classical Driven Pendulum

A parametrically driven pendulum is a simple system that exhibits chaotic behaviour.[30] This frictionless pendulum is driven by a sinusoidally oscillating gravitational field. (Should one be so inclined, these oscillations may be produced in a constant gravitational field by vertically driving the pivot in a sinusoidal manner.) In classical mechanics the position of a pendulum of length ℓ , with a bob of mass m , in a gravitational field g , may be described by a function $\theta(\tau)$. Here $\theta \in [-\pi, \pi]$ is the angular displacement as a function of time, τ . (See Figure 2.1). The driving potential has an amplitude of γ and frequency ϵ . The Hamiltonian is then:

$$H = \frac{m}{2}(l\dot{\theta})^2 - mgl(1 + \gamma \sin \epsilon t) \cos \theta \quad (2.1)$$

The following substitutions are made to convert this into dimensionless units. The time is taken in units of the small angle frequency, $t = \sqrt{\frac{\ell}{g}} \tau$. The position may now be taken to be $x(t) = \theta(\tau)$. The rest position of the pendulum, hanging straight down, is at $x = 0$. From the rest position, counter-clockwise was taken as the positive direction, and the top of the pendulum is therefore at $x = +\pi$. Starting at zero and moving in the clockwise, or negative, direction also brings the pendulum to the top, thus periodic boundary conditions are imposed such that the top is at $x = \pm\pi$. The gravitational potential, without driving, is zero at $x = \pm\frac{\pi}{2}$, $+1$ at $x = \pm\pi$

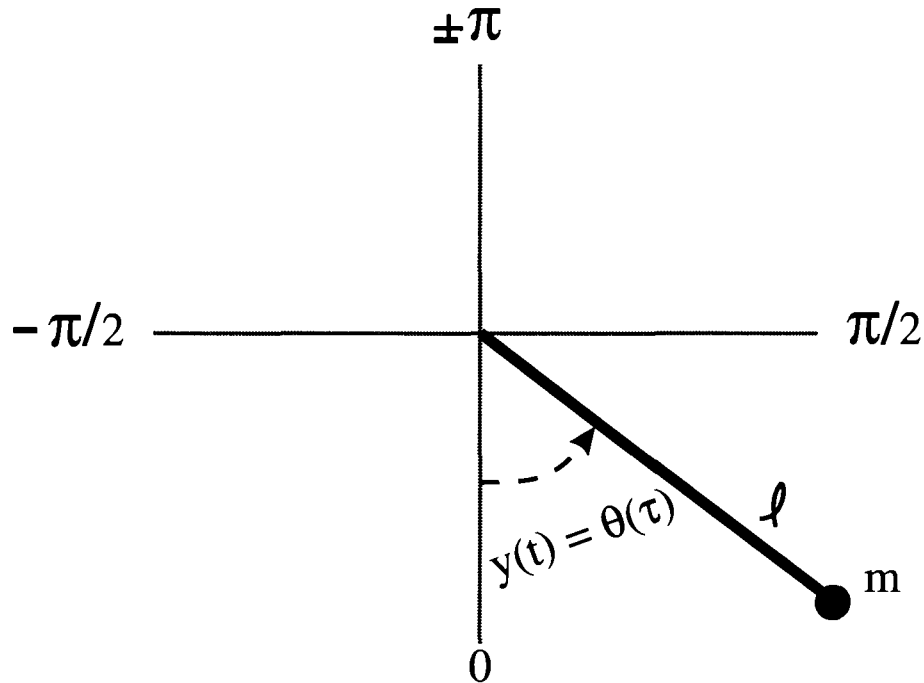


Figure 2.1: The parametrically driven pendulum.

and -1 at $x = 0$. Next, we replace the conjugate momentum to x , P , with the dimensionless momentum $p = \frac{P}{m(g\ell)^{1/2}}$. Lastly we divide the Hamiltonian by mgl to give the dimensionless Hamiltonian :

$$\mathcal{H} = \frac{p^2}{2} - (1 + \gamma \sin \epsilon t) \cos x \quad (2.2)$$

The classical equation of motion in dimensionless units is:

$$\ddot{x} = -(1 + \gamma \sin \epsilon t) \sin x \quad (2.3)$$

2.1.1 Classical Numerical Methods

The classical equation of motion was numerically integrated to give the position and momentum as a function of time. A Runge-Kutta-Nystrom variable time-step routine from the NAG library (D02LAF) was used.[31]

The accuracy of this routine is controlled by setting the error tolerance. An appropriate value was determined by comparing the numerical and analytical solutions

of the equation of motion for a one-dimensional harmonic oscillator. This is unsatisfying; it reassures one little that the method is indeed working for the driven pendulum. An additional, and perhaps more useful, way of gauging the accuracy is to compare results from the driven pendulum with smaller and smaller values of the tolerance. Once the end results converge, one may be reasonably satisfied with them. The most compelling demonstration of the accuracy of the numerical methods was the agreement of expectation values between the quantum and classical ensembles as shown in section 3.1.

2.1.2 Classical Dynamics

The driven pendulum exhibits both periodic and chaotic dynamical behaviour. These behaviours are demonstrated in the Poincaré sections shown in Figures 2.2, 2.4, and 2.6. The section taken is the position-momentum plane when $t = n\frac{2\pi}{\epsilon}$, $n = 0, 1, 2, 3, \dots$, *i.e.* once each period of the driving force. Points in phase space will be referred to as pairs (x, p) , where x is the position and p is the momentum. If these points are on the Poincaré section this is enough to uniquely specify a classical trajectory. Trajectories cannot cross on the Poincaré section. The potentials (as a function of time and position) which gave rise to these behaviours are shown in Figures 2.3, 2.5, and 2.7.

Figure 2.2 is a typical Poincaré section for the driven pendulum, in that it includes both regular and chaotic sections. The parameter values which produced this were $\gamma = -0.5$ and $\epsilon = 3$. This means that the gravitational field oscillations increase and decrease the potential by a factor of $\frac{1}{2}$, and that the frequency of these oscillations is 3 times that of the small-angle frequency of the pendulum. (In dimensionless units, the small angle frequency is 1.) For these parameters, the origin, $(0, 0)$, is a fixed point of the system and thus also of the Poincaré map. The rings surrounding it are sections of regular orbits. They, in turn, are surrounded by a chaotic area of phase space. The two large regular areas centred on $(-1.65, -3.0)$ and $(1.65, 3.0)$ do not share trajectories. The centres of these are fixed points of the Poincaré map, but not of the system. This was verified by taking a different section ($t_n = (n + \frac{1}{4})\frac{2\pi}{\epsilon}$,

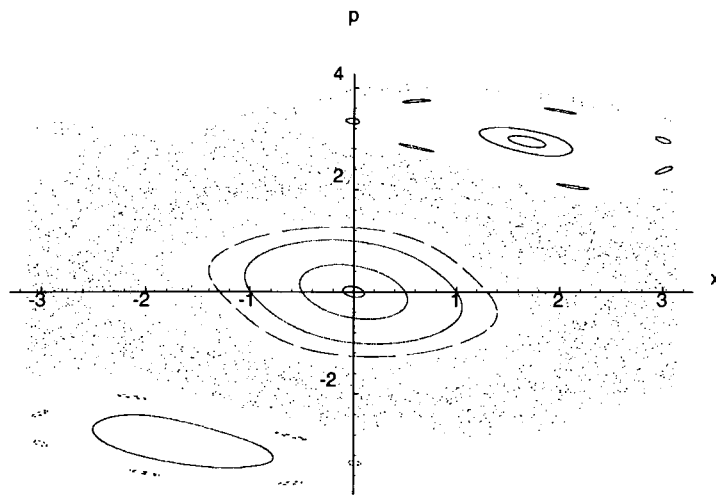


Figure 2.2: Poincaré section for the driven pendulum when $\gamma = -.5$ and $\epsilon = 3$.

for example) in which case the co-ordinates of these fixed points changed. The time dependent potential that produced these behaviours is shown in Figure 2.3.

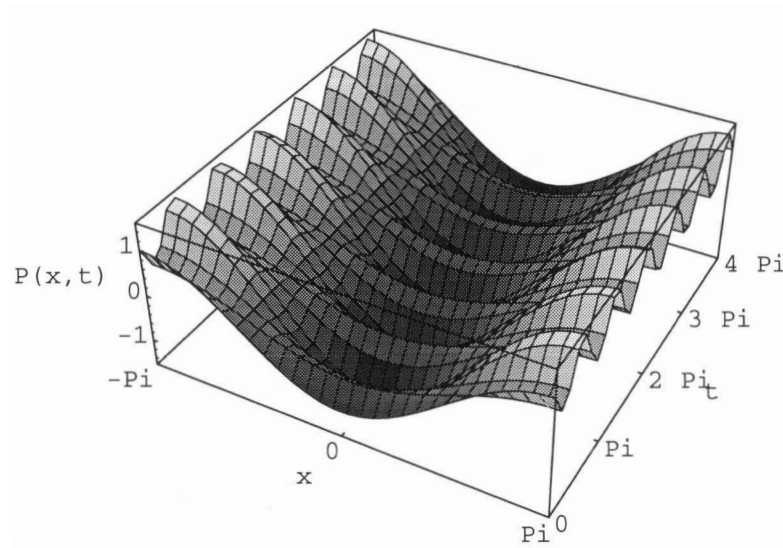


Figure 2.3: The potential as a function of position and time for the driven pendulum where $\gamma = -.5$ and $\epsilon = 3$.

When the driving frequency is twice that of the small-angle frequency (*i.e.* $\epsilon = 2$) there is a resonance, and the fixed point at $(0, 0)$ becomes unstable.[32] A Poincaré section through several orbits is shown in Figure 2.4. The parameter γ remains equal to $-.5$, however, the region of phase space including $(0, 0)$ is now chaotic. There are two regular areas around $(-1, 1)$ and $(1, -1)$ which are both sections through the same orbits; they are centred on a period-2 limit cycle. The potential which produces this is shown in Figure 2.5.

Displaying an unscrupulous contempt for gravity, the driven pendulum may oscillate periodically about the fixed point $\pm\pi$.[33] The Poincaré section shown in Figure 2.6 for $\gamma = 36.3$ and $\epsilon = 11$, displays this behaviour. Both $(0, 0)$ and $(\pm\pi, 0)$ are

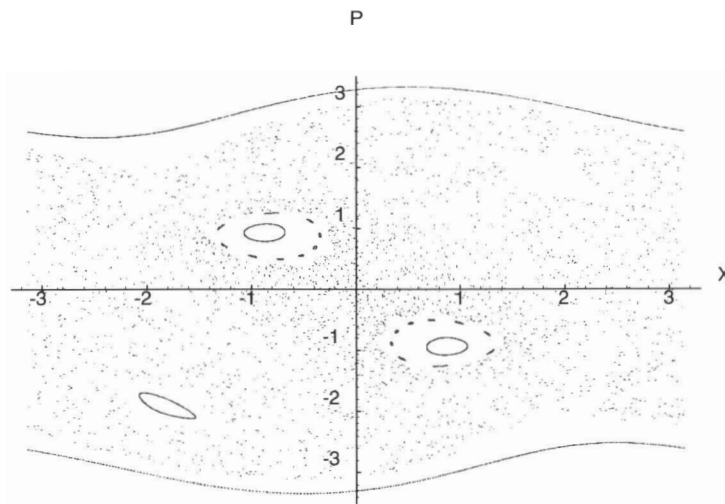


Figure 2.4: Poincaré section for the resonant driven pendulum when $\gamma = -0.5$ and $\epsilon = 2$.

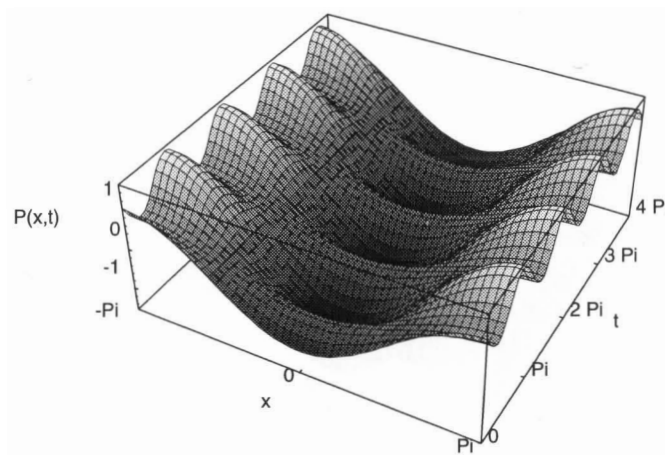


Figure 2.5: The potential as a function of position and time for the driven pendulum when $\gamma = -0.5$ and $\epsilon = 2$.

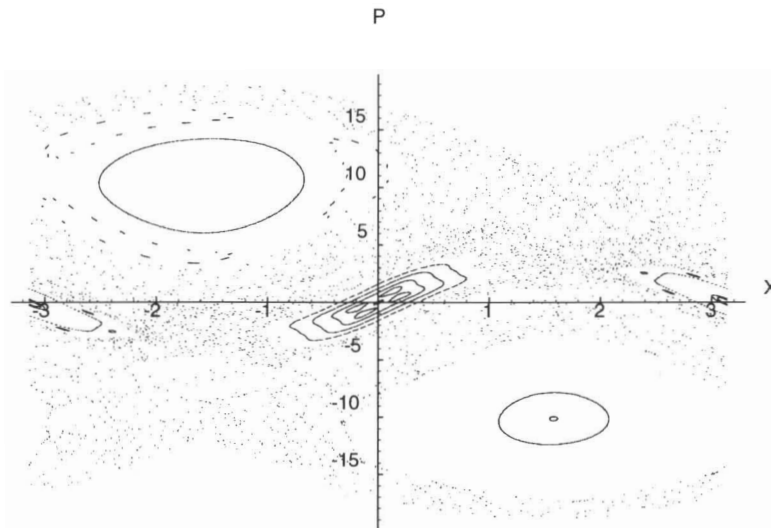


Figure 2.6: Poincaré section for the inverted driven pendulum. Here $\gamma = 36.3$ and $\epsilon = 11$.

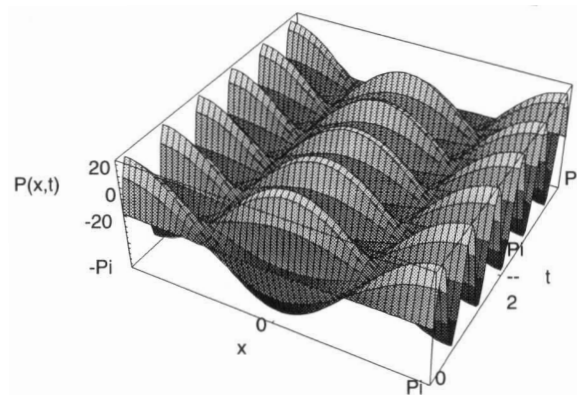


Figure 2.7: The potential as a function of position and time for the driven pendulum here $\gamma = 36.3$ and $\epsilon = 11$.

now centres of stable oscillations. This potential is shown in Figure 2.7.

2.2 The Quantum Driven Pendulum

The quantum-mechanical version of this system is taken to be the system with the same Hamiltonian as equation 2.2, where p and y are now understood to be the momentum and position operators.

To propagate a wave function a time Δt in a potential, we apply the quantum propagator to the wave function: $\psi(t + \Delta t) = U_{\Delta t}\psi(t)$. For time-independent potentials $U_{\Delta t} = e^{-i\Delta t \frac{H}{\hbar}}$, where H is the Hamiltonian. Replacing H with the dimensionless Hamiltonian \mathcal{H} , required the replacement of $\frac{1}{\hbar}$ with a dimensionless constant: $c = \frac{m\ell^3/2g^{1/2}}{\hbar}$. Like \hbar , c is a measure of how far into the quantum regime the system is. As c increases, the size of \hbar decreases relative to the physical constants in the problem—the system becomes more classical.

With these substitutions, the dimensionless quantum time-propagator becomes

$$U_{\Delta t} = e^{-i\Delta t \mathcal{H}c} \quad (2.4)$$

The wave function was chosen at time $t = 0$ to be a minimum uncertainty Gaussian in position representation. A Gaussian is characterized by a width, s , and a position, x_o , for its centre.

$$\Psi(x, 0) = (s\sqrt{2\pi})^{-\frac{1}{2}} e^{-ik_o x} e^{-\frac{(x_o - x)^2}{4s^2}} \quad (2.5)$$

In momentum space this is also a Gaussian, centred at $\frac{k_o}{c}$ with width $(2sc)^{-1}$. This form for the wavefunction was chosen because of its simple analytical form and because it easily provides the minimum uncertainty in position and momentum, *i.e.* $\Delta x \Delta p = 1/(2c)$.

2.2.1 Quantum Numerical Methods

The quantum mechanical wave function in co-ordinate representation was propagated numerically using the split-operator method.[34] The split-operator method works for Hamiltonians that are the sum of two functions: one of the momentum operator, p ,

and one of the position operator, x . Writing $\mathcal{H} = \frac{p^2}{2} + V(x)$, where $V(x)$ is the potential as a function of the position, the propagation operator may then be split:

$$U_{\Delta t} = e^{-i\Delta t\mathcal{H}} \quad (2.6)$$

$$= e^{-ic\Delta t(\frac{p^2}{2} + V(x))} \quad (2.7)$$

$$\simeq e^{-ic\Delta t\frac{p^2}{4}} e^{-ic\Delta tV(x)} e^{-ic\Delta t\frac{p^2}{4}} \quad (2.8)$$

An approximation is made in moving from equation 2.7 to equation 2.8. This symmetric form of the approximation is more accurate than the more obvious two-exponential form.[34] To use this time-independent propagator for our time-dependent potential, we also make the approximation that the potential is constant throughout the time Δt . This approximation is easily achieved by keeping Δt small. The operation of exponentials of position and momentum may be treated as multiplication in the position and momentum representation respectively.

Thus, to propagate $\psi(x, t)$ to $\psi(x, t + \Delta t)$, we replace $\psi(x, t + \Delta t) = U_{\Delta t}\psi(x, t)$ with

$$\psi(x, t + \Delta t) = \text{FFT}_x e^{-ic\Delta t\frac{p^2}{4}} \text{FFT}_p e^{-ic\Delta tV(x)} \text{FFT}_x e^{-ic\Delta t\frac{p^2}{4}} \text{FFT}_p \psi(x, t) \quad (2.9)$$

The wave function in co-ordinate space is Fourier transformed numerically, using the Fast-Fourier-Transform routine C06FUF from the NAG library[31], into momentum space. Then equation (2.9) amounts to a series of Fourier transforms and multiplications. Here FFT_p is the Fourier transform into momentum-space representation of $\psi(x, t)$. The transform back is FFT_x . This is done n times to propagate a wavefunction over a time T , where $n\Delta t = T$.

The accuracy is modified by adjusting the size of the grid on which the wave function is defined and the size of the time step.[34]. As in the classical case, the size of these parameters was chosen to provide accurate numerical simulation of the one-dimensional harmonic oscillator. However, the most dramatic demonstration of the accuracy was the agreement of expectation values between the formalisms, as shown in chapter 3.

The Fourier transform assumes periodic boundary conditions in both representations. Thus the wavefunction in position or momentum space is free to expand

through the boundary and back over itself. In position space, the continuous wavefunction is represented as a discrete list of n complex numbers at positions running from $-\pi$ to π in increments of $\frac{2\pi}{n}$. The periodic boundary conditions come in at $\pm\pi$: the top of the pendulum's swing.

The momentum of a driven pendulum is not periodic. The problem of the wavefunction in momentum representation crossing over the periodic boundary is avoided by choosing the grid such that $\phi(p, t)$ is close to zero near the boundary. In momentum space the Fourier-transformed wavefunction is represented as a list of n complex numbers on a line from $-\frac{n}{2c}$ to $\frac{n}{2c}$ in increments of c^{-1} . From which it can be seen that the maximum momentum, $\pm\frac{n}{2c}$, allowed by the numerics is proportional to the length, n , of the position grid, and thereby, inversely proportional to the resolution, $\frac{2\pi}{n}$, in position space.

2.3 Quantum-Classical Comparison

2.3.1 The Classical Probability Distribution

Quantum mechanics deals with the probability of outcomes whereas classical mechanics deals with well-defined final conditions. In order to make meaningful comparisons between the two, the ensemble interpretation of quantum mechanics was adopted.[35] The classical equivalent of a quantum wavefunction was taken to be an ensemble of classical points in phase space with the same initial probability distributions in position and momentum as the quantum wavefunction. This was done by assigning a random position and momentum from a Gaussian distribution to each initial condition. These initial conditions were achieved numerically via a Gaussian random number generator: G05DDF, from the NAG library.[31] The classical ensemble then had the same initial probability distribution in position and momentum as did the quantum wave function.

The classical phase space probability distribution was displayed by dividing phase space into bins of side length $\frac{2\pi}{100}$ in position and $\frac{n}{100c}$ in momentum. Here n is the number of positions along the quantum grid. (Recall, from section 2.2.1, that the

number of points in the position representation of the wavefunction determines the length of the momentum representation: $P_{\max} = \pm \frac{\hbar}{2c}$.) The number of particles in each bin divided by the total number of particles gives the classical probability for each of these ten thousand points in phase space. This can then be compared to the quantum probability distribution in phase space: the quantum Husimi distribution.

2.3.2 The Quantum Husimi Distribution

To make the comparison between quantum and classical results more transparent, the quantum wave functions were displayed in the Husimi representation. The Husimi distribution is the quantum mechanical equivalent to a classical phase space distribution function. The Heisenberg uncertainty principle will not allow us to assign an exact probability to a point in phase space, but it will allow us to assign a probability to an area at least the size of \hbar . (That is an area of c^{-1} in dimensionless units). Formally

$$\psi_{\text{hus}}(q, p) = \left(\frac{2\pi}{c}\right)^{-\frac{1}{2}} \int_{-\infty}^{\infty} \phi(x)^* \psi(x) dx \quad (2.10)$$

here

$$\phi(x) = \left(\frac{\pi s^2}{c}\right)^{-\frac{1}{4}} e^{-\frac{(x-q)^2}{2s^2} + icpx} \quad (2.11)$$

is a Gaussian whose width in q is s and $(2sc)^{-1}$ in p . [36] The amplitude squared of $\psi_{\text{hus}}(q, p)$ roughly gives the probability that the system is in a Gaussian area of c^{-1} in phase space centred at (q, p) . It amounts to a gaussian smoothing of the actual distribution. This distribution may be used to compare the filling of phase space by a wavefunction to that of a classical ensemble. [37]

2.3.3 Calculation of Expectation Values.

In addition to comparing the probability distributions in phase space, the expectation values of position, momentum, both squared, the kinetic and potential energies and the total energy as well as the expectation value of the time development operator (see section 3.3) were also calculated.

These operators, excepting the total energy, are all functions of either position or momentum. The expectation value of the total energy was calculated by adding the expectation values of kinetic and potential energy. The quantum expectation value of an operator A corresponds to its average value. When A is diagonal in the position representation, its expectation value is given by:

$$\langle A \rangle_{qm} = \int_{-\infty}^{\infty} a(x) |\psi(x)|^2 dx \quad (2.12)$$

This is the weighted average of the possible values, $a(x)$, which the operator A may produce. The weights are the probabilities of each measured value at the position x . For operators that are diagonal in momentum representation,

$$\langle B \rangle_{qm} = \int_{-\infty}^{\infty} b(p) |\psi(p)|^2 dx \quad (2.13)$$

Here, the weighted average is of the possible values, $b(p)$, which may be measured by the operation B . The weights are the probabilities of measuring the value $b(p)$ at momentum p . In order to numerically calculate the quantum expectation value, the integral was replaced by a sum over the discrete positions, or momenta.

The classical expectation value is an average of the function in question over the ensemble.

These definitions and the classical average were used to calculate the expectation values of those operators that were functions either of position or momentum. The two exceptions were the average energy and the average quasienergy. The average energy is the sum of the average kinetic energy (a function of momentum) and the average potential energy (a function of position). The average quasienergy will be dealt with in section 3.3.

It should be noted that because of the periodic boundary conditions, the average value of x will not appear in the middle of distributions that extend around the edge. For example, the average position of a Gaussian centred at $\pm\pi$ will be zero. In such cases, the physical significance of the expectation value is lost, but for comparison between the two theories the usefulness is retained. There will be a similar effect on the value of $\langle x^2 \rangle$. The momentum does not extend to the boundary and so this will not affect its expectation values.

Chapter 3

Results For the Driven Pendulum

Both quantum and classical ensembles were propagated for times up to 150 drive cycles. The probability distributions and expectation values were calculated for both theories. For both quantum and classical ensembles, the expectation values of x , x^2 , p , p^2 , the one-period time-development operator, the kinetic energy, the potential energy, and, by addition, the total energy were calculated. The stan-

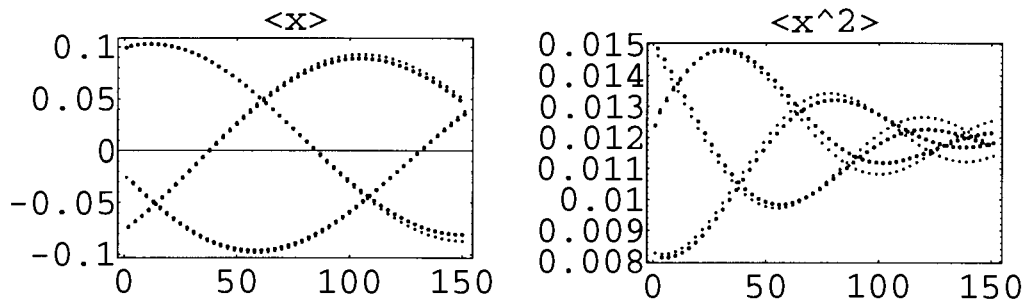


Figure 3.1: Periodic A. Expectation values for position and position squared for quantum and classical ensembles centered at $(.1, 0)$ for $\gamma = -.5$ and $\epsilon = 3$. The Poincaré section for this system is shown in Figure 2.2 The large dots are the quantum values and the small dots are the classical values.

dard deviations $(\langle x^2 \rangle - \langle x \rangle^2)^{\frac{1}{2}}$ in position and momentum were also calculated. Comparison of the expectation values and the phase-space probability distributions showed occasions of great agreement and large disagreement.

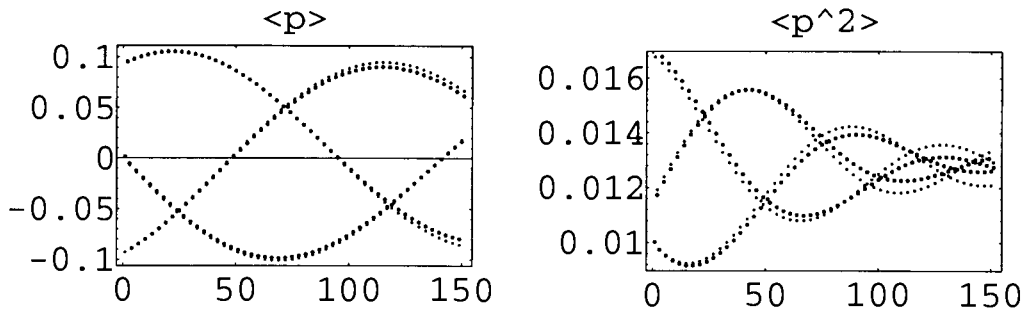


Figure 3.2: Periodic A. Expectation values for momentum and momentum squared for the same ensemble as in Figure 3.1.

Identical initial position distributions were used for three values of c : 50, 100, and 250. Recall that for a fixed width in position, the width in momentum space is inversely proportional to c . The value of $c = 100$ was chosen because it gives a Gaussian whose area in phase space fits easily into either a chaotic or a regular area. The regular area in the centre of the phase space of Figure 2.2 has an area of approximately 9. This is much larger than the size of $c^{-1} = 10^{-2}$, which means that a wavefunction started within this area may be localized entirely within it. This is also true for the chaotic region, which has an approximate area of 26. The more

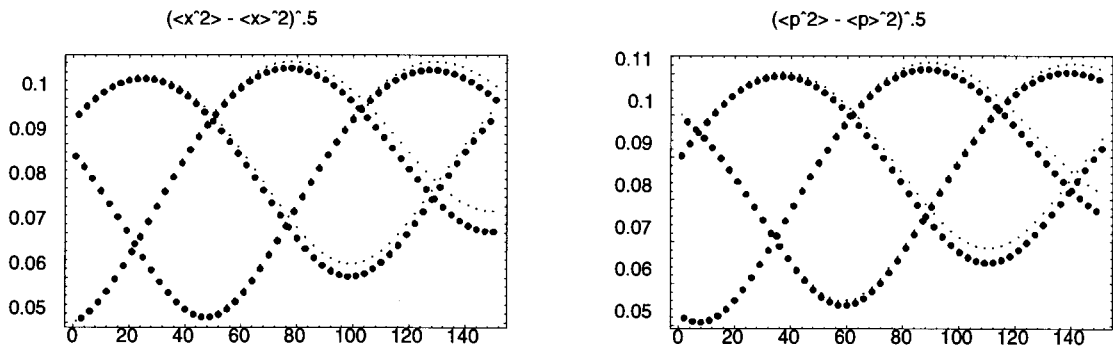


Figure 3.3: Periodic A. Expectation values for the standard deviation in momentum and position for the same ensemble as Figure 3.1.

interesting behaviours were repeated for $c = 50$ and $c = 250$. In the latter case a 2048 point grid still extends far enough in momentum space to contain the wavefunction

as it spreads. The value of $c = 50$ was chosen simply as half of $c = 100$. (Recall that as c increased, the value of \hbar relative to the other physical constants in the problem decreased—the system became more classical.)

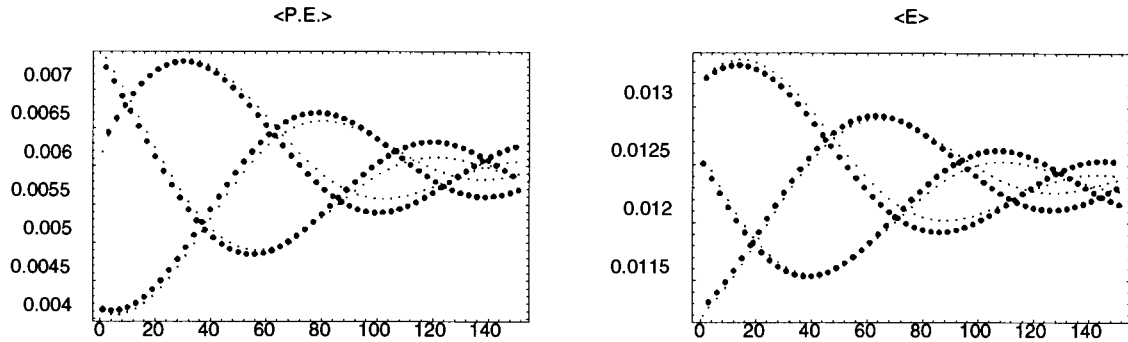


Figure 3.4: Periodic A Expectation values for the kinetic and total energy for the same ensemble as Figure 3.1. The potential energy is $1/2$ of $\langle p^2 \rangle$, which is shown in Figure 3.2.

Ensembles were started for each of the four parameter choices outlined in section 2.1.2. Each is given a label that appears in each Figure to help sort the results. In the typical phase space ($\gamma = -.5, \epsilon = 3$, see the Poincaré section in Figure 2.2) four ensembles were used. Two were centred in the chaotic area: $(-3, -1.7)$, which is called Chaotic A, and $(-2.3, 0)$, called Chaotic B. The other two were centred in regular areas, one at $(.1, 0)$, Periodic A, and the other at $(-1.7, 3)$, Periodic B. A single ensemble was propagated in the resonant case ($\gamma = -.5, \epsilon = 2$, see the Poincaré section in Figure 2.4). It was centred at the unstable fixed point $(0,0)$, and is referred to as Resonant. For the stable inverted pendulum ($\gamma = 36.3, \epsilon = 11$, see the Poincaré section in Figure 2.6), ensembles were used in the regular areas surrounding $(0,0)$, named Inverted A, and $(\pm\pi, 0)$, Inverted B. The results covered in the next two sections, and these names, are summarized in Table 3.1.

3.1 Regular Dynamics

For all initial conditions, both expectation values and probability distributions agreed well for short times of a few tens of drive cycles. For $\gamma = -.5$ and $\epsilon = 3$, gaussian

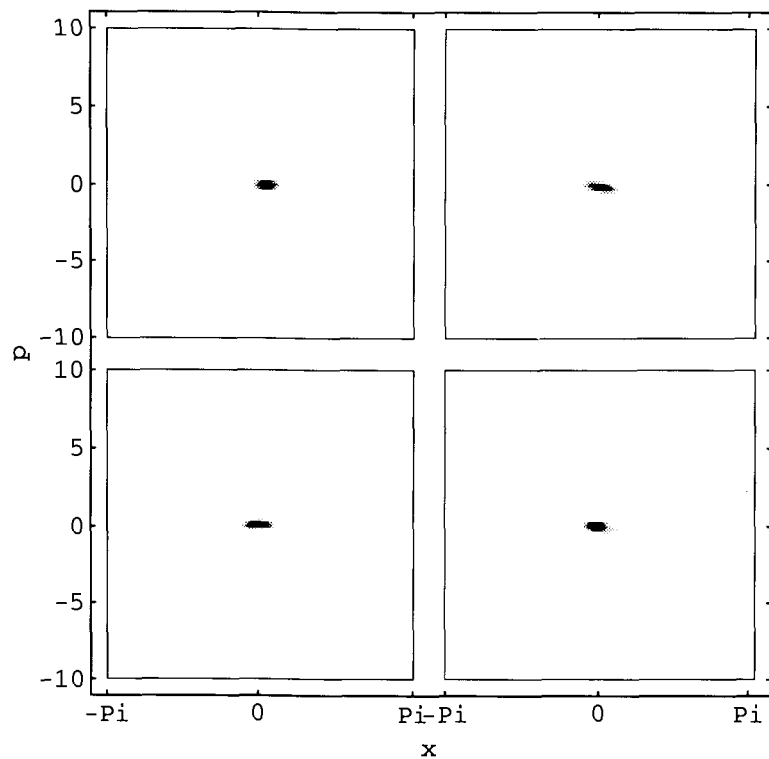


Figure 3.5: Periodic A Quantum probability distributions for times = 0, 1, 100, and 150 periods of the driving force. This is for the same ensemble as Figure 3.1. The black areas represent .2 of the initial peak of the distribution. White is zero probability. The Poincaré section for the classical trajectories is shown in Figure 2.2

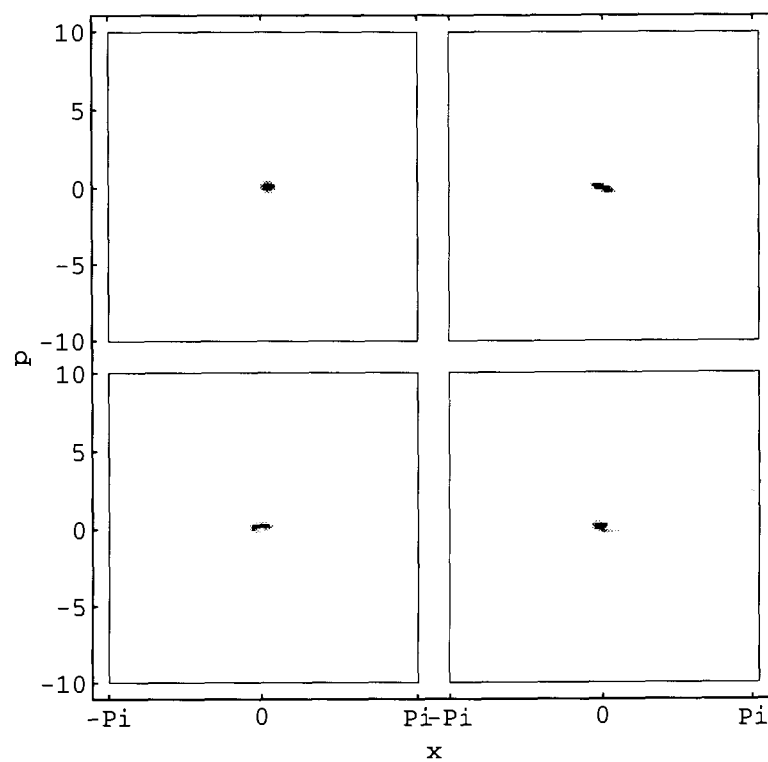


Figure 3.6: Periodic A. Classical probability distributions for time = 0, 1, 100, and 150 periods of the driving force. This is for the same ensemble as Figure 3.1. The grey shades represent the same probability values as in the quantum case in Figure 3.5. The Poincaré section is shown in Figure 2.2

ensembles of width $s = .05$ initially centered in the regular areas of phase space, that is, centred on $(.1, 0)$ Periodic A and $(-1.7, -3)$ Periodic B, there was no significant difference between the classical and quantum expectation values (see Figures 3.1, 3.2, 3.3, 3.4, and Figures 3.7, 3.8, 3.9, and 3.10) and probability distributions (see Figures 3.5, 3.6, 3.11, and 3.12) for times up to 150 cycles of the driving force.

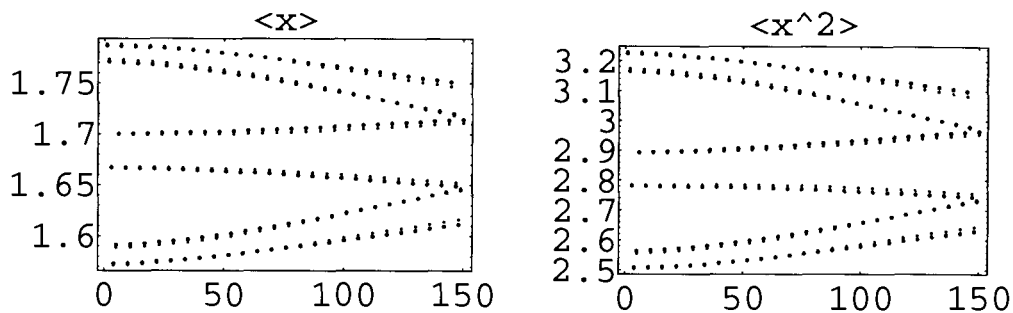


Figure 3.7: Periodic B. Position and position-squared expectation values for quantum and classical ensembles centered at $(1.7, 3)$ for $\gamma = -.5$ and $\epsilon = 3$. The large dots are the quantum values and the small ones are the classical values. The Poincaré section for these parameter values is shown in Figure 2.2.

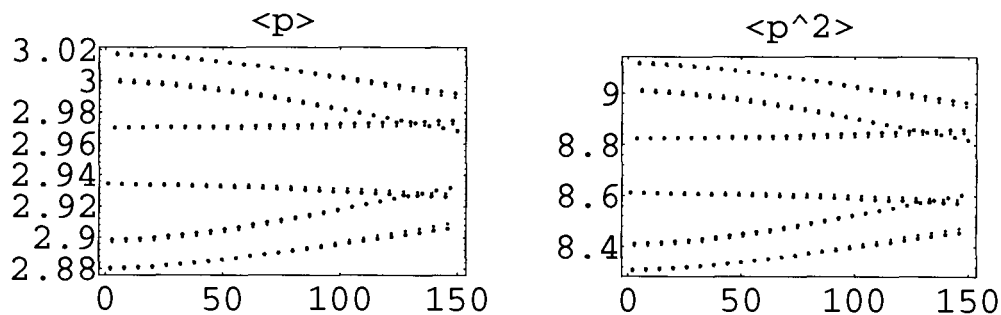


Figure 3.8: Periodic B. Momentum and momentum-squared expectation values for quantum and classical ensembles centered at $(1.7, 3)$ for $\gamma = -.5$ and $\epsilon = 3$. The large dots are the quantum values and the small ones are the classical values. The Poincaré section for these parameter values is shown in Figure 2.2.

For $\gamma = 36.3$ and $\epsilon = 11$, for which the inverted pendulum is stable, ensembles were started in the centres of the regular regions at $(0, 0)$ (Inverted A) and $(\pm\pi, 0)$ (Inverted

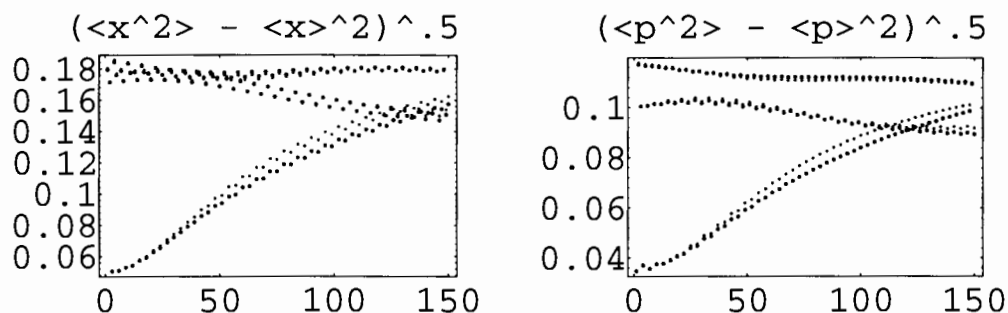


Figure 3.9: Periodic B. Standard deviations for momentum and position expectation values for quantum and classical ensembles centered at $(1.7, 3)$ for $\gamma = -.5$ and $\epsilon = 3$. The large dots are the quantum values and the small ones are the classical values. The Poincaré section for these parameter values is shown in Figure 2.2.

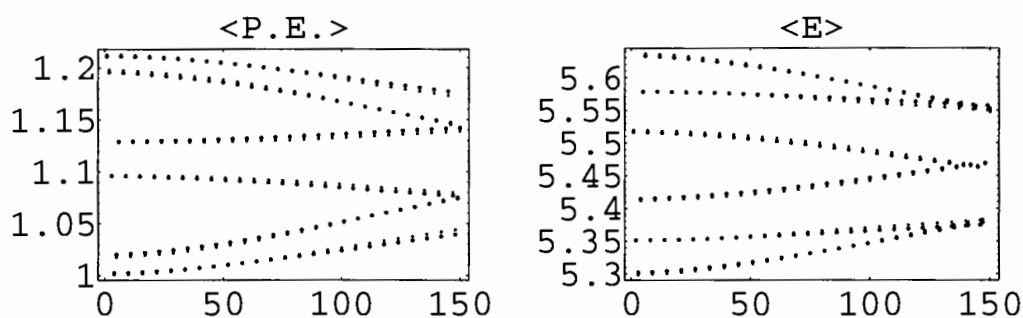


Figure 3.10: Periodic B Potential and total-energy expectation values for quantum and classical ensembles centered at $(1.7, 3)$ for $\gamma = -.5$ and $\epsilon = 3$. The large dots are the quantum values and the small ones are the classical values.

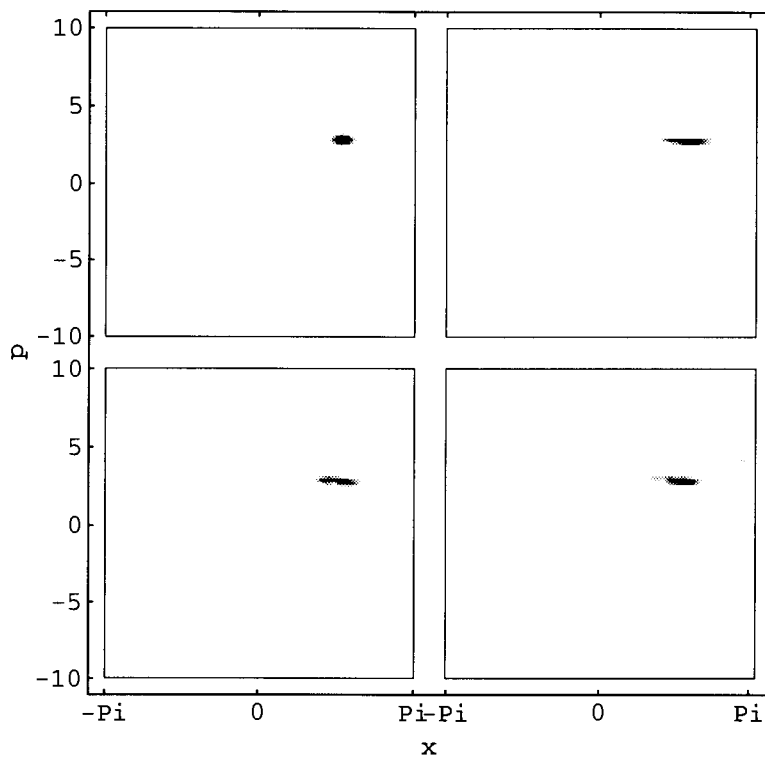


Figure 3.11: Periodic B. Quantum probability distributions for time = 0,1,100, and 150 drive cycles for the same ensemble as Figure 3.7.

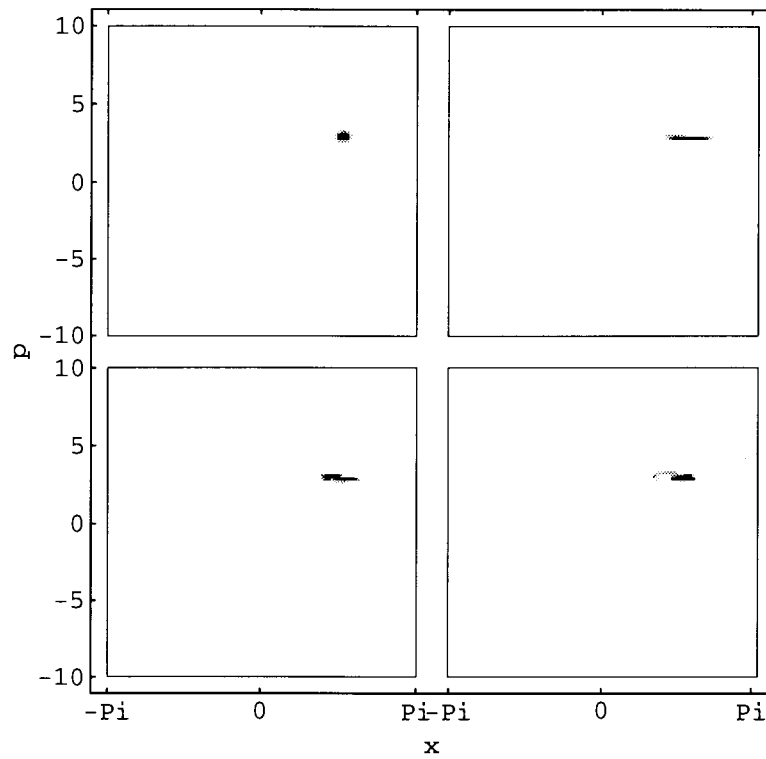


Figure 3.12: Periodic B. Classical probability distributions for time = 0, 1, 100, and 150 drive cycles for the same ensemble as Figure 3.7.

B). (See Figure 2.6.) Here also there was good agreement between the quantum and classical expectation values, as shown in Figures 3.13–3.16 and 3.17–3.20. The position expectation values for Inverted B ($\pm\pi, 0$) show that the quantum average position is offset slightly from the correct value of zero. The position values for Inverted A, centered at $(0,0)$, and the momentum values for both inverted cases, show structure in the classical values that is absent in the quantum one. This reflects small oscillations of the classical ensemble about the centre of the quantum ensemble. The close agreement of the rest of the classical and quantum expectation values show that the ensembles are spreading at the same rate and over the same area. This demonstrated that the dynamical behaviour (regular *versus* chaotic) is more important in determining the amount of agreement than other considerations such as energy. Close agreement in the regular regime has also been observed in other similar systems.[6][10][11][17][16] This agreement demonstrated quite clearly that both numerical methods are sufficiently accurate for this system.

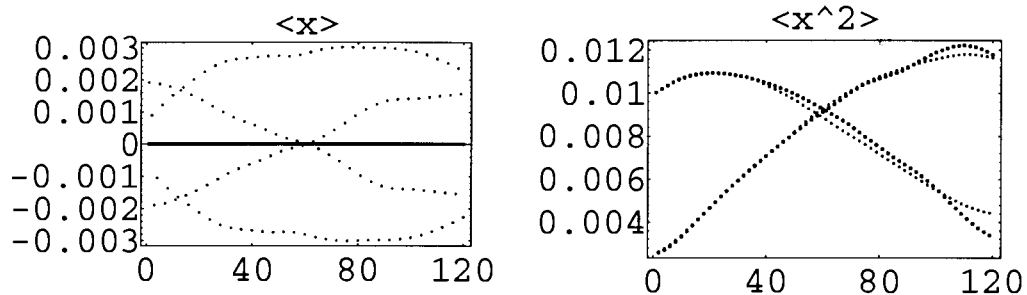


Figure 3.13: Inverted A. Expectation values for position and position squared for quantum and classical ensembles centered at $(0,0)$ for $\gamma = 36.3$ and $\epsilon = 11$. The small points are the classical values, the larger ones are the quantum values.

The results were much more interesting when the ensemble was centred in the chaotic regime. One difference between the regimes was that the wavefunction quickly filled up an area in phase space and thereafter its behaviour was dominated by interference effects. These were not seen in the regular ensembles discussed this far. Thus, it was useful to determine how quantum interference patterns which extend over the whole wave function affect the expectation values, independent of chaos. To this end,

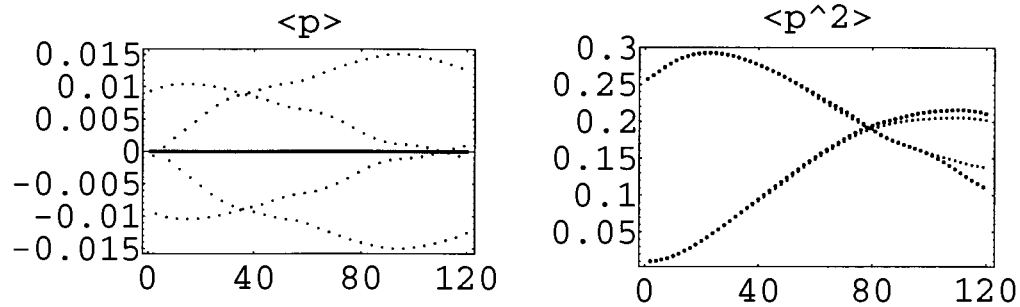


Figure 3.14: Inverted A. Expectation values for momentum and momentum squared for quantum and classical ensembles centered at $(0, 0)$ for $\gamma = 36.3$ and $\epsilon = 11$. The small points are the classical values, the larger ones are the quantum values.

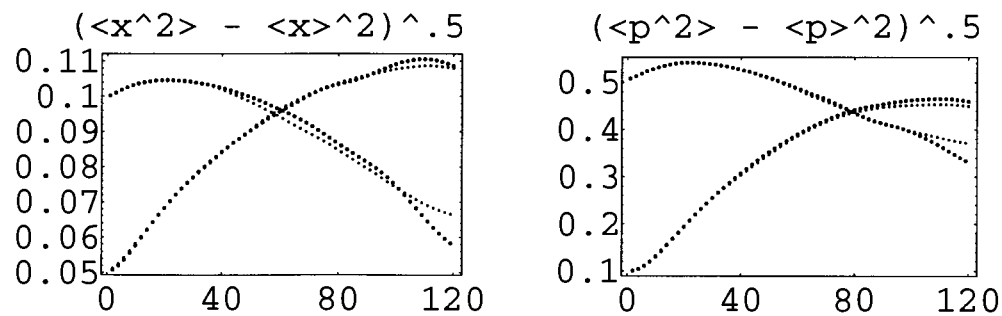


Figure 3.15: Inverted A. Standard deviations for position and momentum for quantum and classical ensembles centered at $(0, 0)$ for $\gamma = 36.3$ and $\epsilon = 11$. The small points are the classical values, the larger ones are the quantum values.

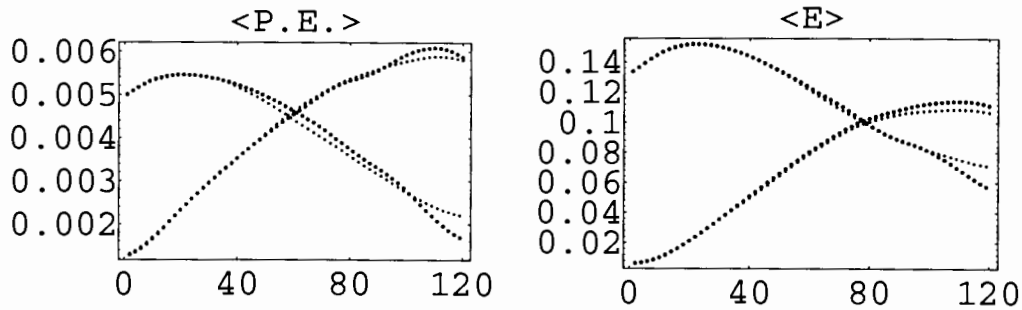


Figure 3.16: Inverted A. Kinetic and total-energy expectation values for quantum and classical ensembles centered at $(0,0)$ for $\gamma = 36.3$ and $\epsilon = 11$. The small points are the classical values, the larger ones are the quantum values.

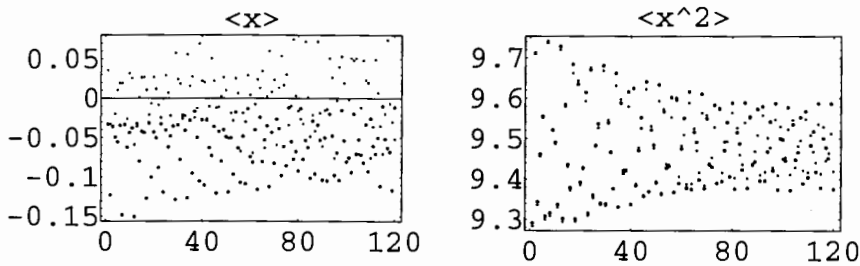


Figure 3.17: Inverted B . Expectation values for position and position squared for quantum (large dots) and classical (small dots) ensembles centered at $(\pm\pi, 0)$ for $\gamma = 36.3$ and $\epsilon = 11$.

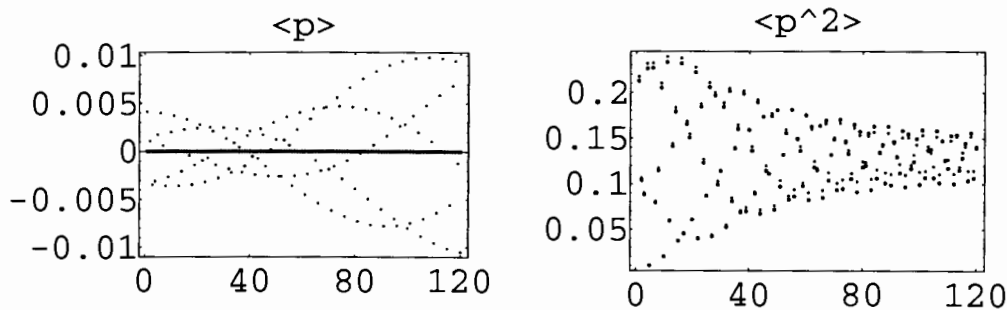


Figure 3.18: Inverted B . Expectation values for momentum and momentum squared for quantum (large dots) and classical (small dots) ensembles centered at $(\pm\pi, 0)$ for $\gamma = 36.3$ and $\epsilon = 11$.

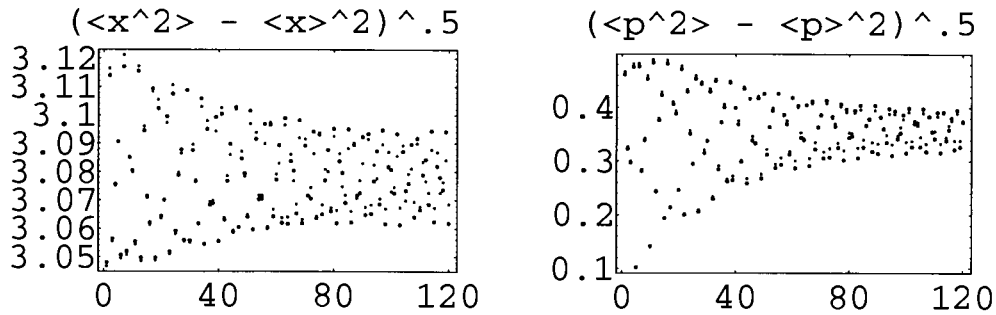


Figure 3.19: Inverted B Standard deviation of position and momentum for quantum (large dots) and classical (small dots) ensembles centered at $(\pm\pi, 0)$ for $\gamma = 36.3$ and $\epsilon = 11$.

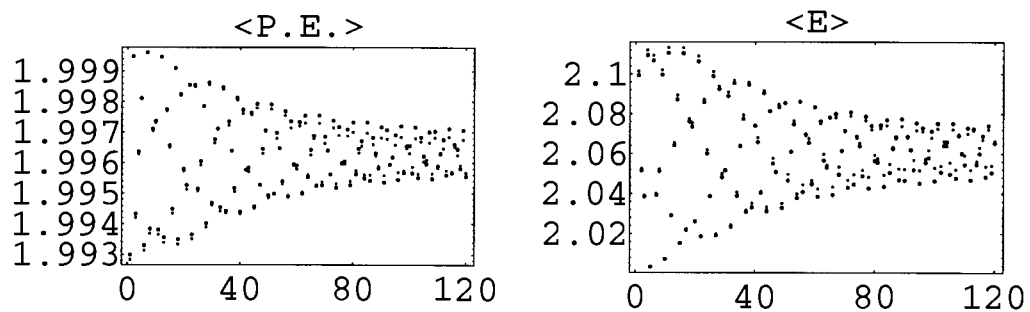


Figure 3.20: Inverted B. Expectation values of kinetic and total energy for quantum (large dots) and classical (small dots) ensembles centered at $(\pm\pi, 0)$ for $\gamma = 36.3$ and $\epsilon = 11$.

a Gaussian ensemble was propagated with initial centre $(-1, 1.7)$ in a system where $\gamma = 0$ (*i.e.* no driving force). The phase space of the simple pendulum contains only regular trajectories. Starting the ensemble with this energy allowed it to travel across the position boundary at $\pm\pi$. This resulted in the creation of large persistent regions of overlap. In quantum mechanics, these show up as interference in the probability distribution and as simple addition in the classical probability distribution. This is shown in Figures 3.25 and 3.26. This is similar to the interference patterns that dominated the appearance of the chaotic probability distributions. Figures 3.21–3.24 show the effect of interference on the expectation values. One can see that the result of the interference was that the quantum expectation values oscillated about the classical value but the qualitative behaviour was similar.

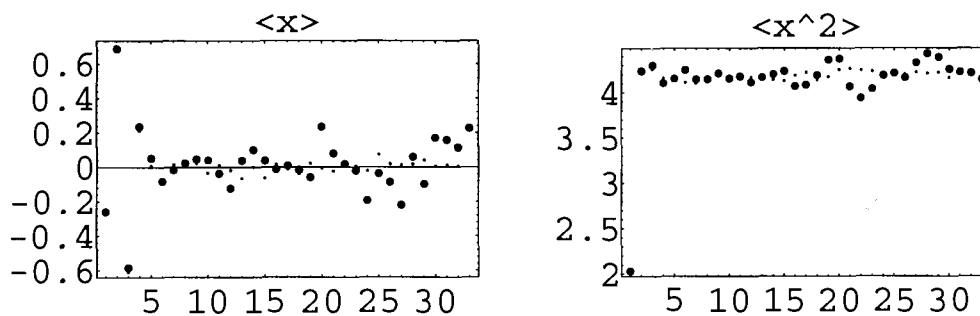


Figure 3.21: Simple Pendulum. Position and position-squared expectation values for quantum and classical ensembles centered at $(-1, 1.7)$ for the simple pendulum. The bigger dots are the quantum values and the smaller dots are the classical values.

Anticipating the chaotic results: knowing the effect of interference on the expectation values allowed differentiation between disagreements that could be attributed simply to interference and those due to other quantum effects. Quantum interference results in oscillations about the classical expectation value.

3.2 Chaotic and Resonant Dynamics

For the parameters $\gamma = -.5$ and $\epsilon = 3$ two ensembles were propagated starting in the chaotic regime. (The appropriate Poincaré section is shown in Figure 2.2.) One was

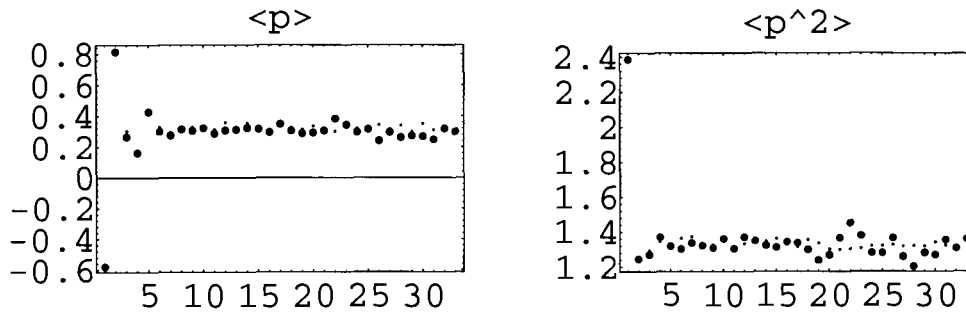


Figure 3.22: Simple Pendulum. Momentum and momentum-squared expectation values for quantum and classical ensembles centered at $(-1, 1.7)$ for the simple pendulum. The bigger dots are the quantum values and the smaller dots are the classical values.

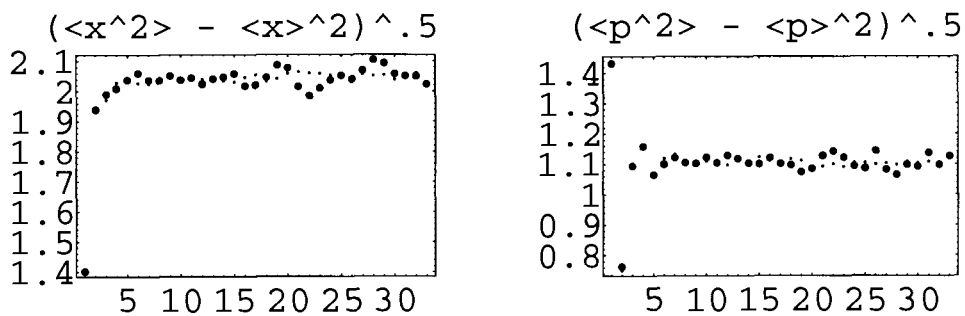


Figure 3.23: Simple Pendulum. The standard deviations for position and momentum for the quantum and classical ensembles centered at $(-1, 1.7)$ for the simple pendulum. The bigger dots are the quantum values and the smaller dots are the classical values.

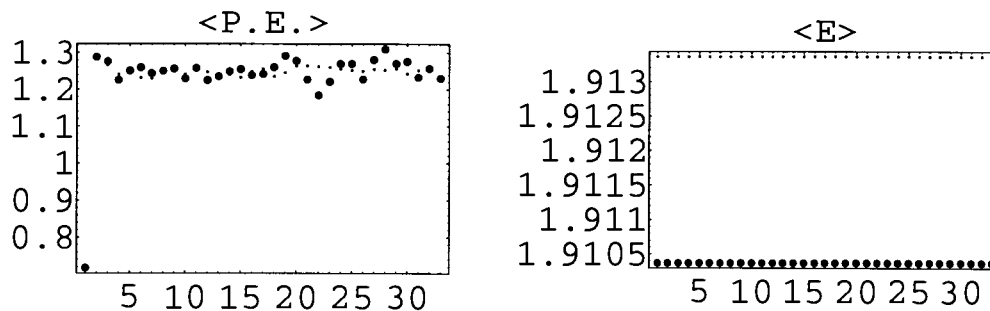


Figure 3.24: Simple Pendulum. The expectation values of kinetic and total energy for quantum and classical ensembles centered at $(-1, 1.7)$ for the simple pendulum. The bigger dots are the quantum values and the smaller dots are the classical values.

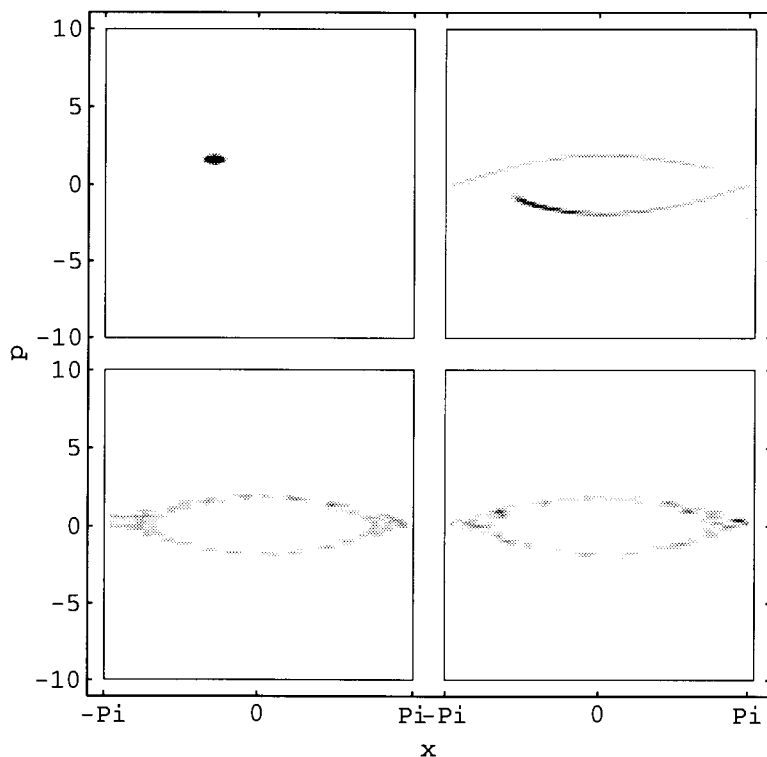


Figure 3.25: Simple Pendulum. Quantum probability distributions for the same ensemble as Figure 3.21. The time runs from left to right, top to bottom, and is at 0, 1, 10, and 30 linear-pendulum periods. Black represents .2 of the initial maximum probability and white represents zero.

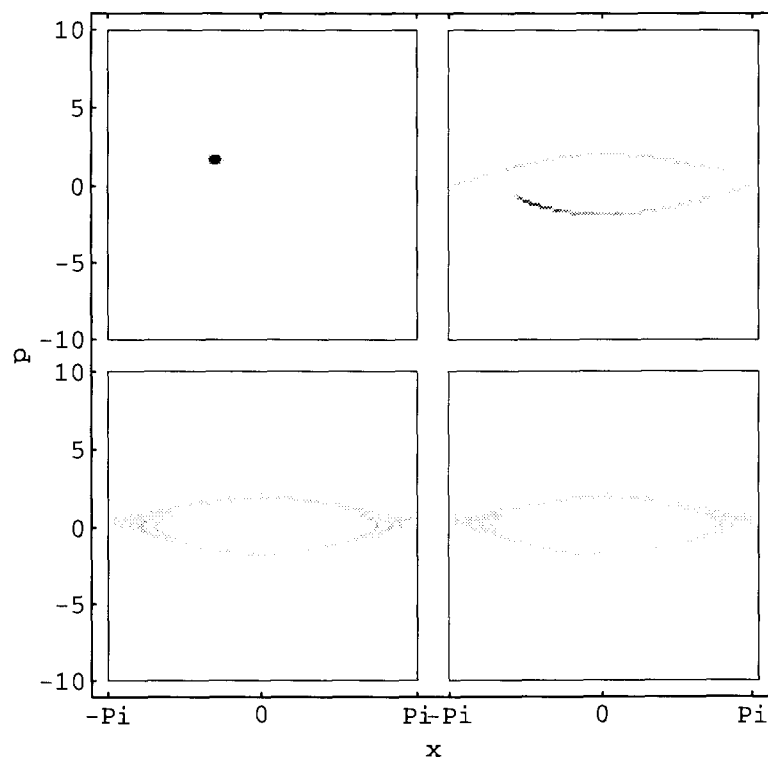


Figure 3.26: Simple Pendulum. Classical probability distributions for the same ensemble as Figure 3.21. The time runs from left to right, top to bottom, and is at 0, 1, 10, and 30 linear-pendulum periods. Black represents .2 of the initial maximum probability and white represents zero.

Centre	Label	γ	ϵ	See Figure	Dynamics	Agreement?
(1.7,3)	Periodic B	-.5	3	2.2	Regular	Very Good
(0.1, 0)	Periodic A	-.5	3	2.2	Regular	Very Good
(-1, 1.7)	Simple Pendulum	0	N/A	N/A	Regular	Very Good
(0, 0)	Inverted A	36.3	11	2.6	Regular	Good
($\pm\pi$, 0)	Inverted B	36.3	11	2.6	Regular	Good
(-3, -1.7)	Chaotic A	-.5	3	2.2	Chaotic	Good
(-2.3, 0)	Chaotic B	-.5	3	2.2	Chaotic	Poor
(0,0)	Resonant	-.5	2	2.4	Chaotic	Poor

Table 3.1: A summary of the results presented in sections 3.1 and 3.2 for the driven pendulum. The Figure column refers to the appropriate Poincaré section. Agreement refers to the how well the classical and quantum expectation values agreed.

initially centred at $(-3, -1.7)$, Chaotic A, and the other at $(-2.3, 0)$, Chaotic B. For the first case there was good agreement between quantum and classical theories for all the expectation values up to 150 drive cycles (see Figures 3.27–3.30). The small oscillations of the quantum values about the classical values may be attributed to interference effects. This is supported by looking at the actual probability distributions (see Figures 3.31–3.34). The quantum distribution shows higher probability in the momentum range -2 to -4 .

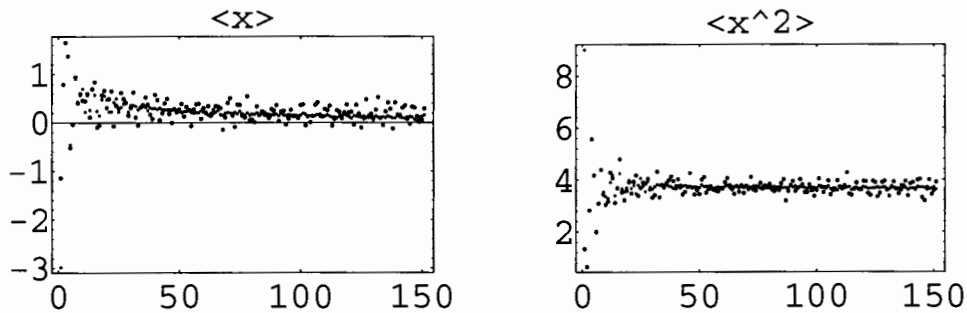


Figure 3.27: Chaotic A. Quantum and classical expectation values for position and position squared. The ensembles were initially centered at $(-3, -1.7)$ and $\gamma = -.5$ and $\epsilon = 3$. The large dots are the quantum values and the small dots are the classical values.

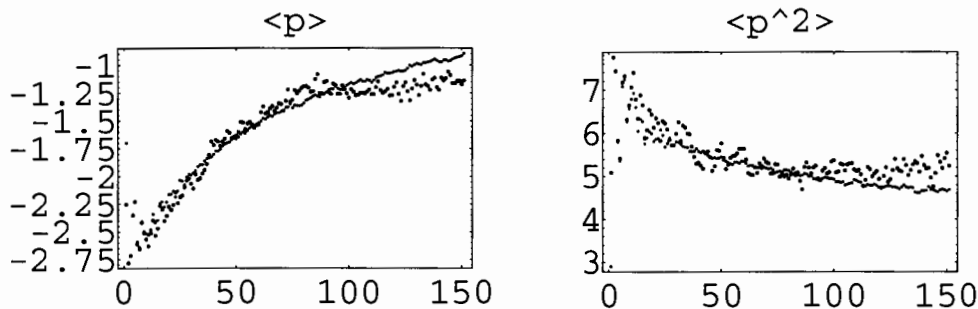


Figure 3.28: Chaotic A. Quantum and classical expectation values for momentum and momentum squared. The ensembles were initially centered at $(-3, -1.7)$ and $\gamma = -.5$ and $\epsilon = 3$. The large dots are the quantum values and the small dots are the classical values.

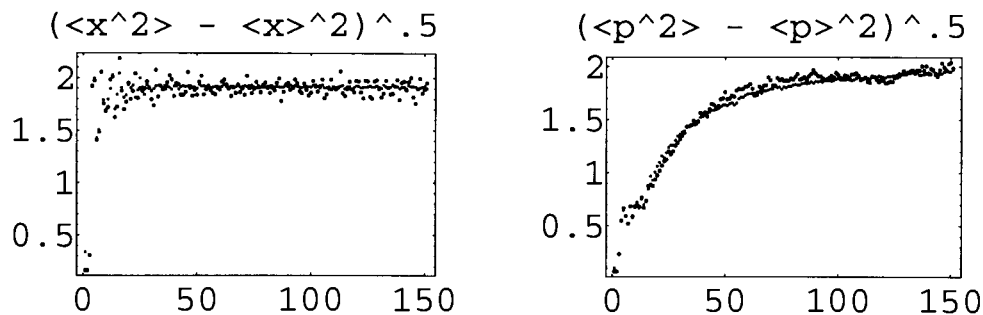


Figure 3.29: Chaotic A . Quantum and classical standard deviations for position and momentum. The ensembles were initially centered at $(-3, -1.7)$ and $\gamma = -0.5$ and $\epsilon = 3$. The large dots are the quantum values and the small dots are the classical values.

The classical ensemble which started at $(-2.3, 0)$ (and referred to as Chaotic B) ended up occupying a similar range in phase space as did the $(3, -1.7)$ (Chaotic A) ensemble. It initially agreed well with the quantum ensemble until the interference effects became widespread. These small disagreements, due to interference, are typical of quantum systems in the chaotic regime.[5][6][10][11][21] However, the classical ensemble disagreed greatly with the quantum ensemble after around 80 drive cycles. (See Figures 3.35–3.38). As can be seen from the actual probability distributions, the disagreement stems from the ability of the classical ensemble to spread into an area of phase space which the quantum mechanical ensemble can not reach. (See Figures 3.39–3.42).

This area is the remnant separatrices in the neighbourhood of ± 2 in momentum that surround the two regular areas in the $(+, +)$ and $(-, -)$ quadrants. The inability of the quantum ensemble to reach this area of phase space occurred even though the other ensemble, which started on this remnant separatrix, quickly covered the starting area of this ensemble. This is reminiscent of the lack of momentum diffusion in the quantum kicked rotor.[24] Here the quantum and classical theories gave measurably different predictions: classically, the driven pendulum will reach momenta greater than two, and quantum mechanically, it will not. The disagreement was postponed to later times, however, when the value of c was raised to 250, see Figures 3.43–3.46. It

occurs earlier when c is lowered to 50, see Figures 3.47–3.50. This suggests that the classical and quantum mechanical descriptions agree longer as the system becomes more classical. In section 3.3, a plausible explanation is given for how two ensembles

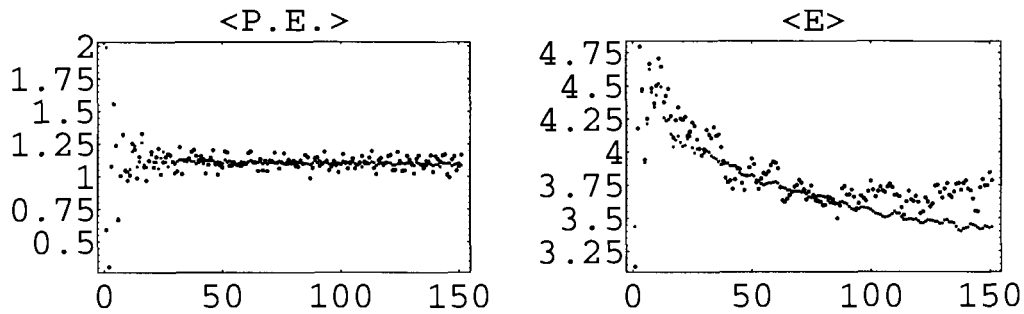


Figure 3.30: Chaotic A. Quantum and classical expectation values for kinetic and total energy. The ensembles were initially centered at $(-3, -1.7)$ and $\gamma = -0.5$ and $\epsilon = 3$. The large dots are the quantum values and the small dots are the classical values.

whose classical fates are indistinguishable should have such different final quantum distributions.

The final chaotic example was under resonant conditions: $\gamma = -0.5$ and $\epsilon = 2$. The centre was initially at the unstable fixed point, $(0, 0)$. In this case the disagreement between the theories occurred in both position and momentum. It started at around 20 drive cycles. (See Figures 3.51–3.54.) However, the early disagreement, between 20 and 60 cycles, was also heavily influenced by the interference fluctuations occurring at the origin. (See Figures 3.55–3.55.) By 60 drive cycles, it was clear that the classical ensemble was continuing to expand in both position and momentum, whilst the quantum ensemble remained bounded in both. This lack of agreement was not ameliorated by increasing c to 250 (thus decreasing the relative value of \hbar) and moving the system closer to the classical regime, see Figures 3.59–3.59. When c was reduced to 50, the quantum ensemble expanded faster than the classical one, as is shown in Figures 3.63–3.66. The quasienergy representation will be invoked in the next section to help explain this quantum behaviour.

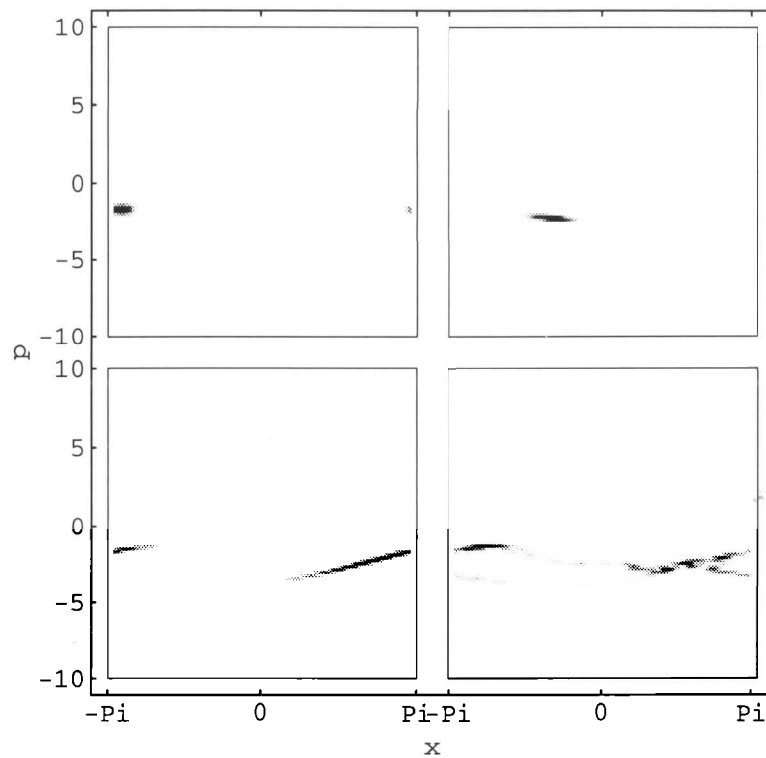


Figure 3.31: Chaotic A . Quantum probability distributions for time = 0, 1, 4 and 8 drive cycles for the same ensemble as in Figure 3.27. The Poincaré section is shown in Figure 2.2. The probability scale runs from black, at .2 of the initial maximum probability, down to white, at zero probability.

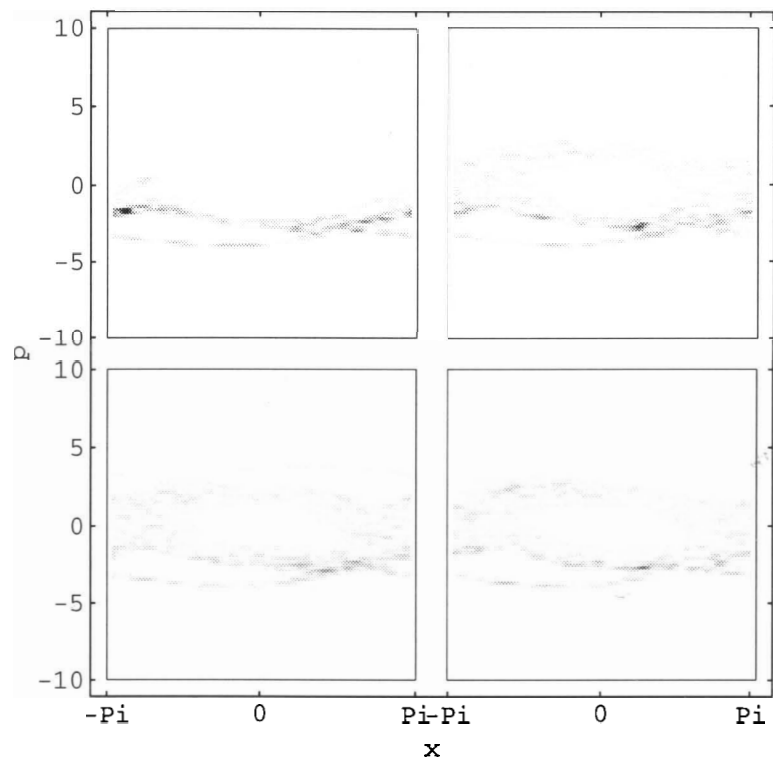


Figure 3.32: Chaotic A . Quantum probability distributions for time = 16, 48, 100, and 150 drive cycles for the same ensemble as in Figure 3.27.

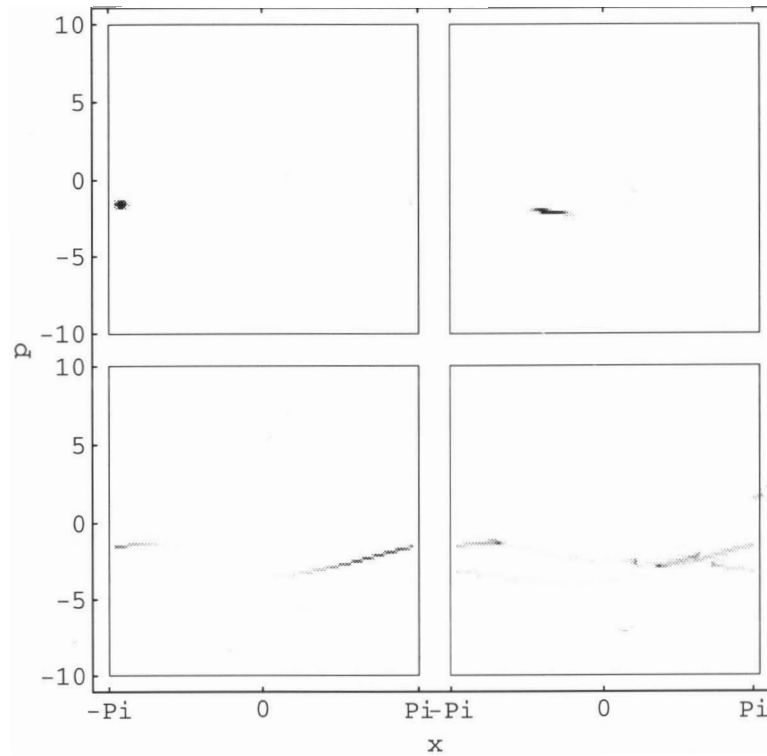


Figure 3.33: Chaotic A . Classical probability distributions for time = 0, 1, 4 and 8 drive cycles for the same ensemble as in Figure 3.27. The Poincaré section is shown in Figure 2.2. The gray scales are set the relative to the initial distribution as in the other probability distributions.

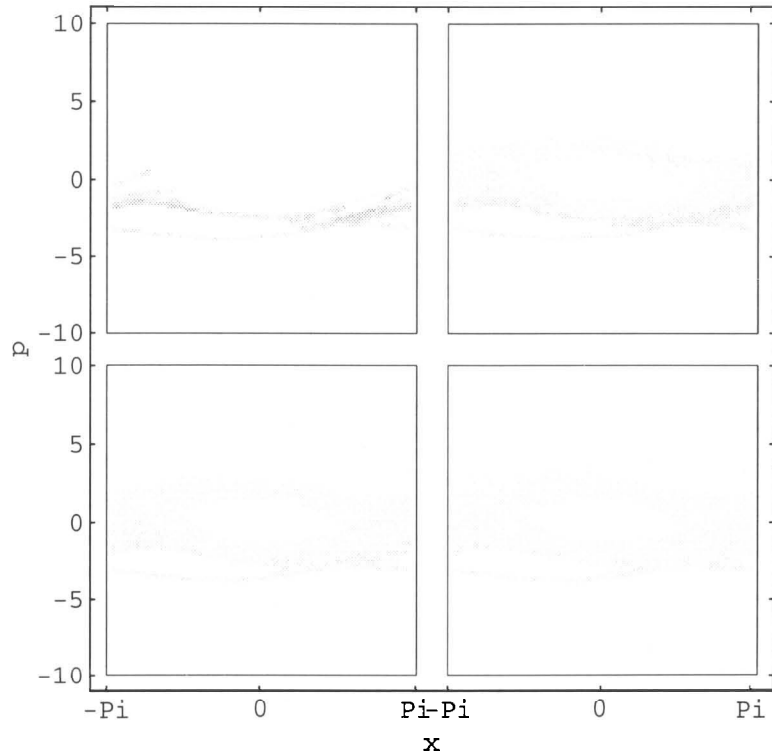


Figure 3.34: Chaotic A . Quantum probability distributions for time = 16, 48, 100 and 150 drive cycles for the same ensemble as in Figure 3.27. The Poincaré section is shown in Figure 2.2. The gray scales are set the relative to the initial distribution as in the other probability distribuions.

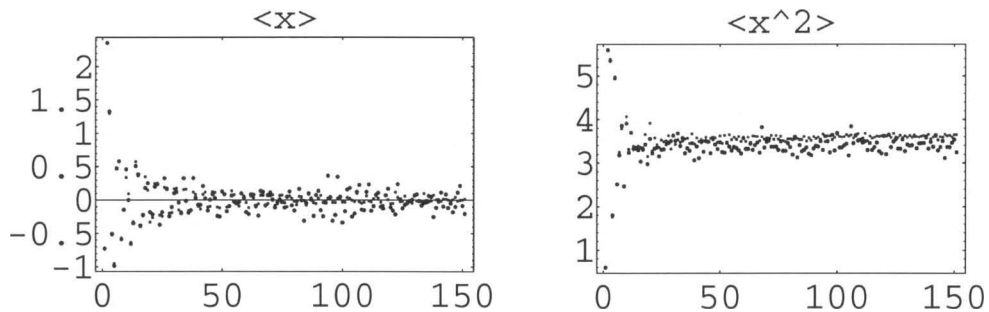


Figure 3.35: Chaotic B. Expectation values for position and position squared for quantum and classical ensembles centered at $(-2.3, 0)$ for $\gamma = -.5$, $\epsilon = 3$ and $c = 100$. The small dots are the classical values and the large dots are the quantum values. The relevant Poincaré section is shown in Figure 2.2.

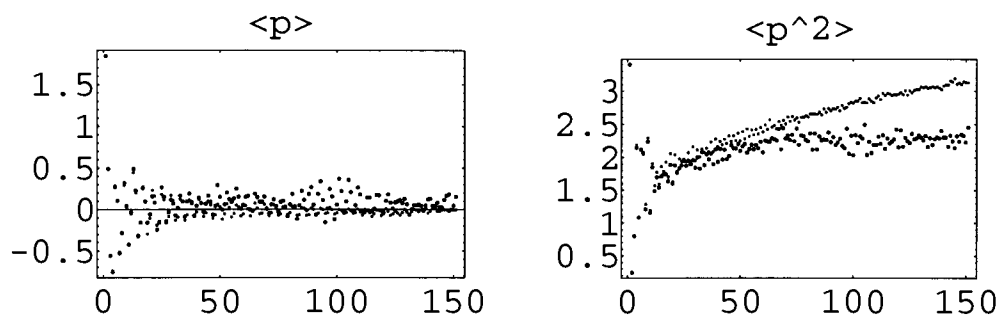


Figure 3.36: Chaotic B. Expectation values for momentum and momentum squared for the same ensemble as Figure 3.35.

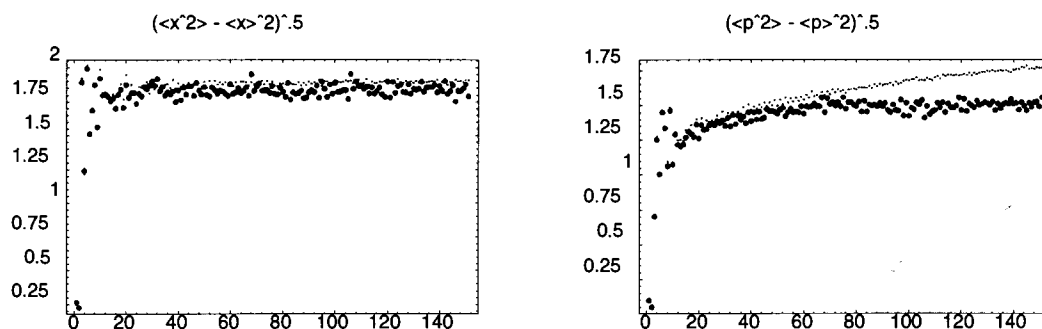


Figure 3.37: Chaotic B. Expectation values for the standard deviation of position and momentum for the same ensemble as Figure 3.35. The classical Poincaré section is shown in Figure 2.2.

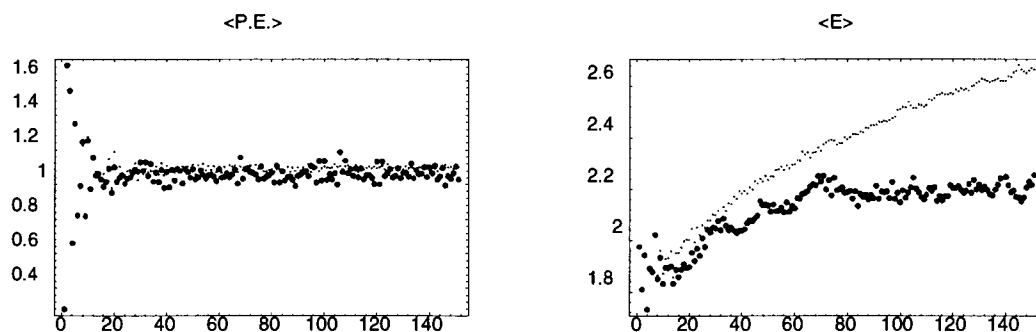


Figure 3.38: Chaotic B. Expectation values for potential and total energy for the same ensemble as in Figure 3.35. The classical Poincaré section is shown in Figure 2.2.

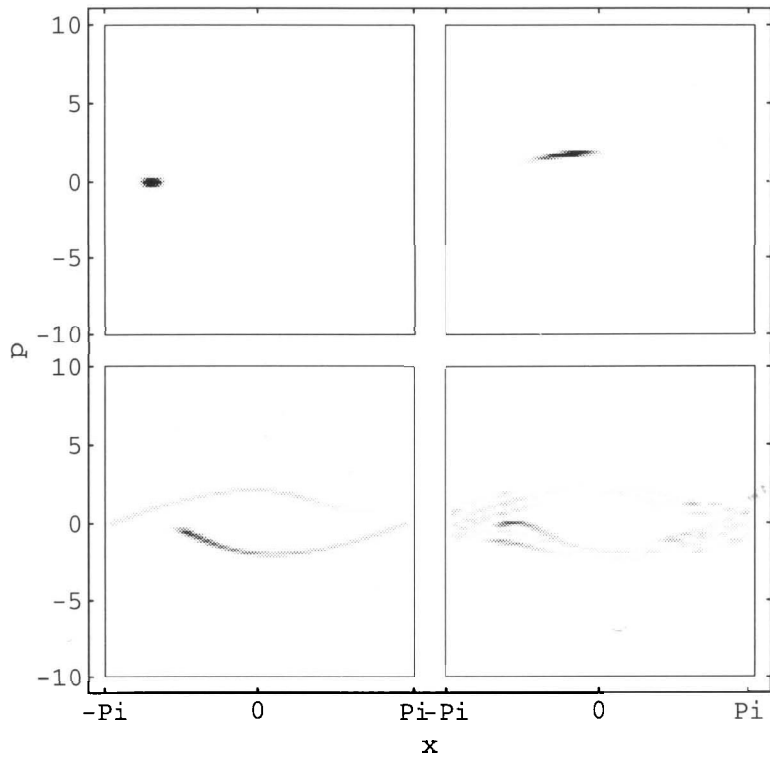


Figure 3.39: Chaotic B. Quantum probability distributions for time = 0, 1, 4, 8 drive cycles for the ensemble centered at $(-2.3, 0)$ for $\gamma = -.5$, $\epsilon = 3$ and $c = 100$. The probability is represented as white for zero, up to .2 of the initial distribution, shown as black. The Poincaré section is found in Figure 2.2.

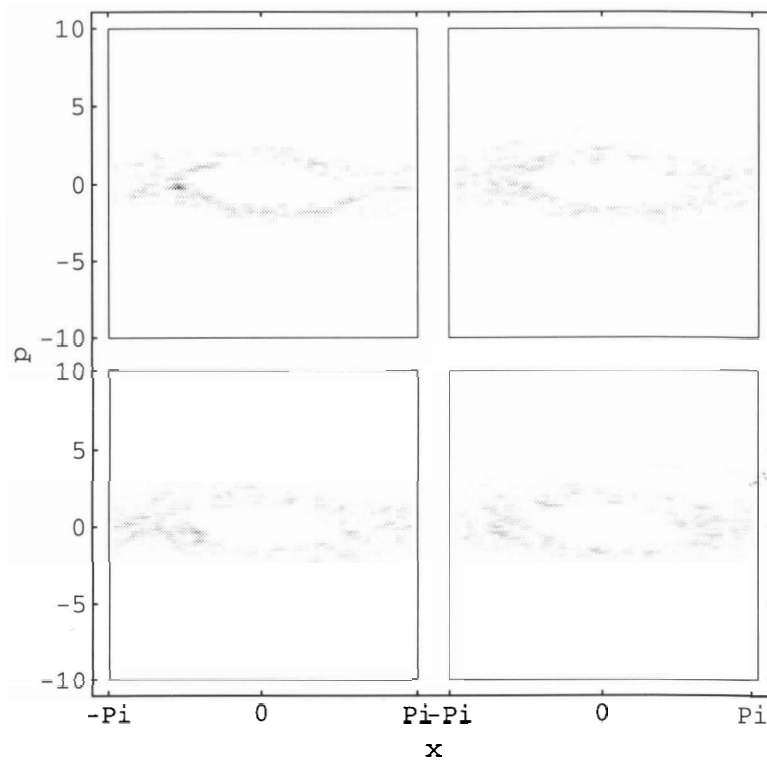


Figure 3.40: Chaotic B. Quantum probability distributions for time = 16, 48, 100, and 150 drive cycles for the same ensembles as in Figure 3.39. The grey scale is the same as in the other probability distributions. The Poincaré section is found in Figure 2.2.

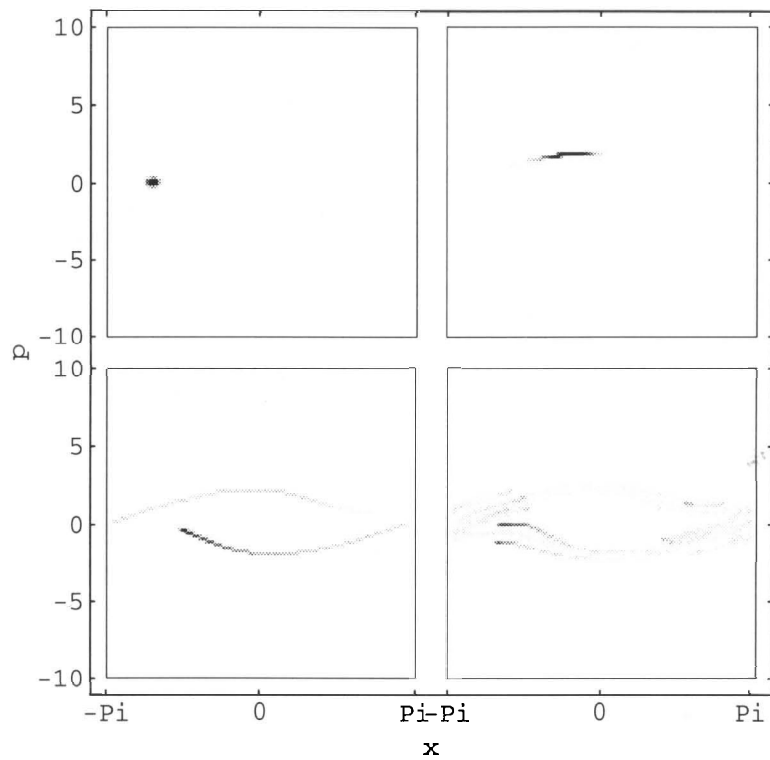


Figure 3.41: Chaotic B. Classical probability distributions for time = 0, 1, 4, and 8 drive cycles for the same ensembles as in Figure 3.39.

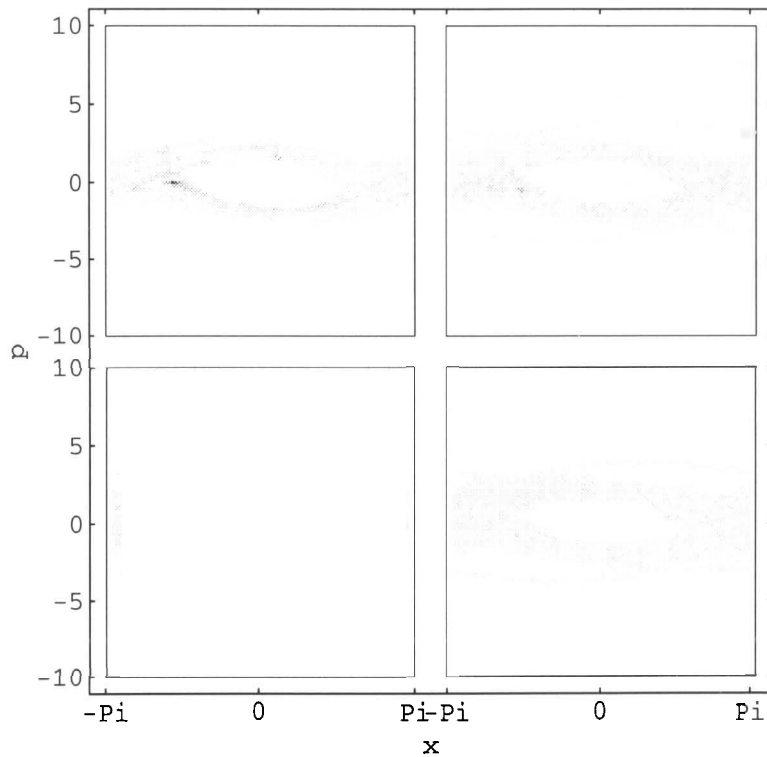


Figure 3.42: Chaotic B. Classical probability distributions for time = 16, 48, 100, and 150 drive cycles for the same ensembles as in Figure 3.39.

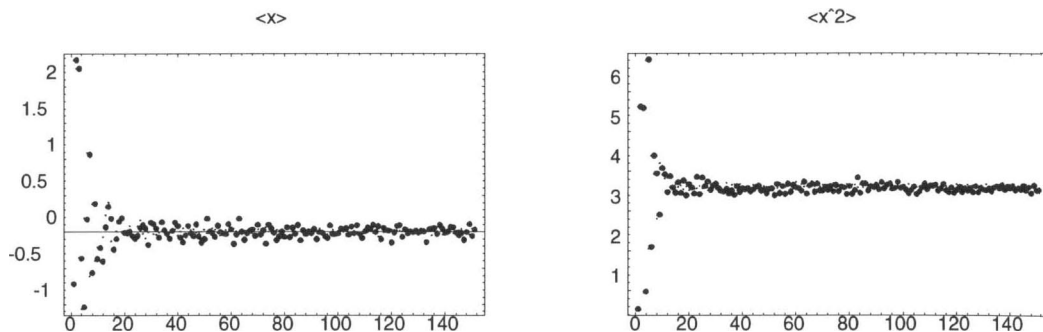


Figure 3.43: Chaotic B. Position and position squared expectation values for quantum and classical ensembles centered at $(-2.3, 0)$ for $\gamma = -0.5$, $\epsilon = 3$ and $c = 250$. The Poincaré section is shown in Figure 2.2.

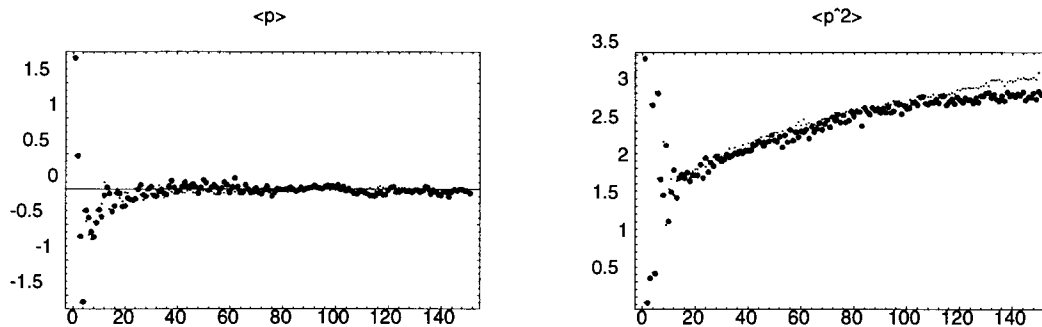


Figure 3.44: Chaotic B. Momentum and momentum-squared expectation values for the same ensembles as Figure 3.43.

3.3 Application of Quasienergies to Results

In the chaotic examples shown above, the boundedness of the quantum $\langle p^2 \rangle$ expectation and/or $\langle x^2 \rangle$ expectation values, compared to their classical equivalents, could not be due to the same mechanism as that of Anderson localization in the kicked rotor. This was clear from the agreement in the $(-3, -1.7)$ Chaotic A case and also from the fact that classically the momentum is bounded by the dynamics and the position by the boundary conditions even when the ensembles disagree. Hence, the argument that leads to the mapping of the kicked-rotor problem onto the Anderson localization problem does not apply at all in the case of the disagreement of $\langle x^2 \rangle$; the momentum in the kicked rotor is unbounded classically. However, it must be true

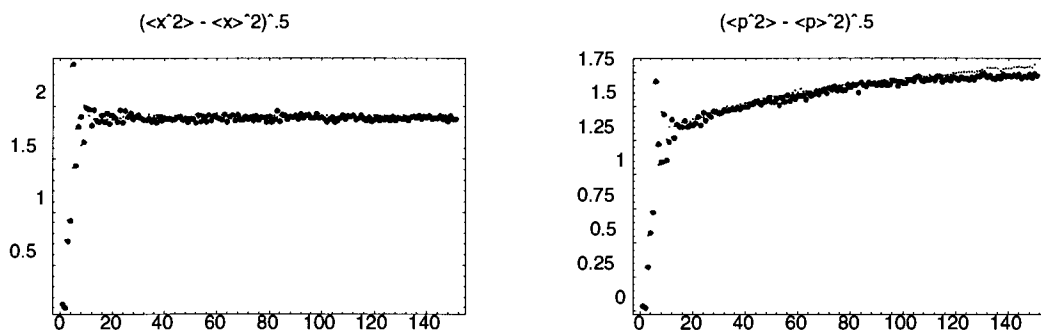


Figure 3.45: Chaotic B. Momentum and position standard deviations for the same ensembles as Figure 3.43.

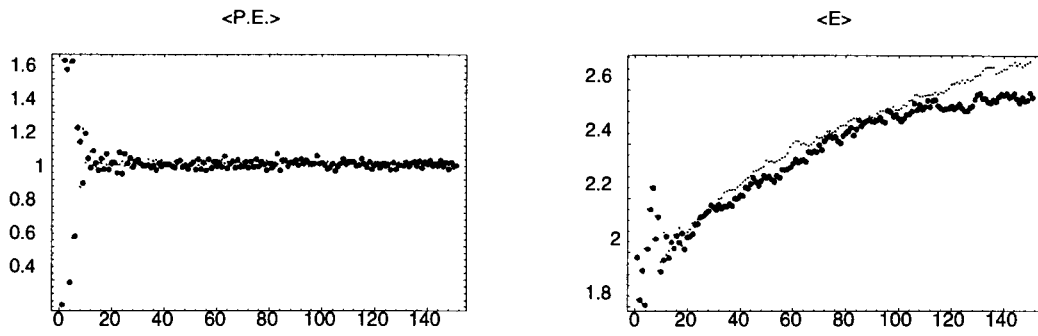


Figure 3.46: Chaotic B. Potential and total energy for the same ensembles as Figure 3.43.

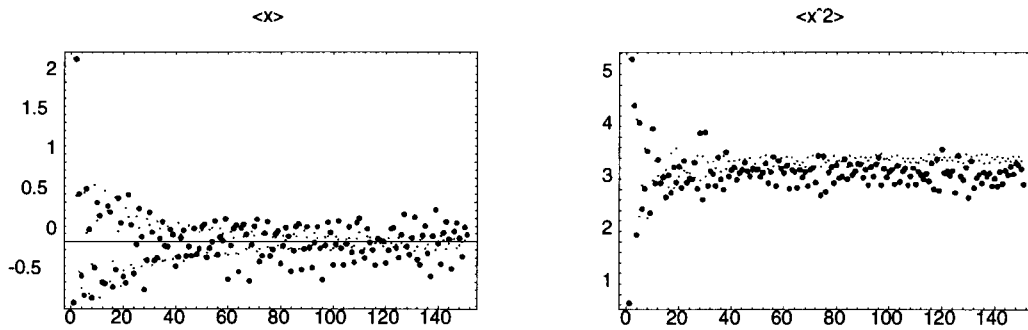


Figure 3.47: Chaotic B. Expectation values of position and position squared for quantum and classical ensembles centered at $(-2.3, 0)$ for $\gamma = -.5$, $\epsilon = 3$ and $c = 50$.

that the quasienergy eigenfunctions for the driven pendulum Hamiltonian were localized in position and momentum, since the wavefunction was at all times a sum (given in equation 1.3) fixed by the initial conditions, of such functions. It would be useful to have knowledge of the quasienergy eigenfunctions that made up this sum for the various cases considered above. If they were bounded in position and/or momentum this would explain the quantum results. The difference between the members of this sum in the $(3, -1.7)$ Chaotic A case and the $(-2.3, 0)$ Chaotic B case would go a long way towards explaining their different behaviour. It would also be nice to know the eigenvalues. Such a calculation is, in method, quite simple.

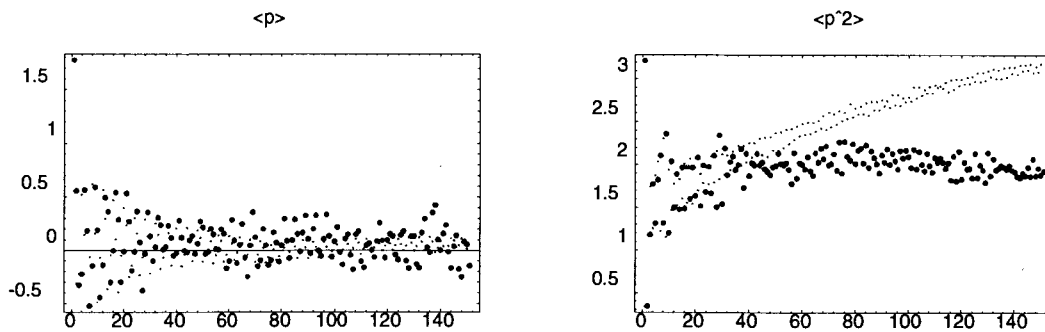


Figure 3.48: Chaotic B. Expectation values of momentum and momentum squared for the ensembles centered at $(-2.3, 0)$ for $\gamma = -0.5$, $\epsilon = 3$ and $c = 50$.

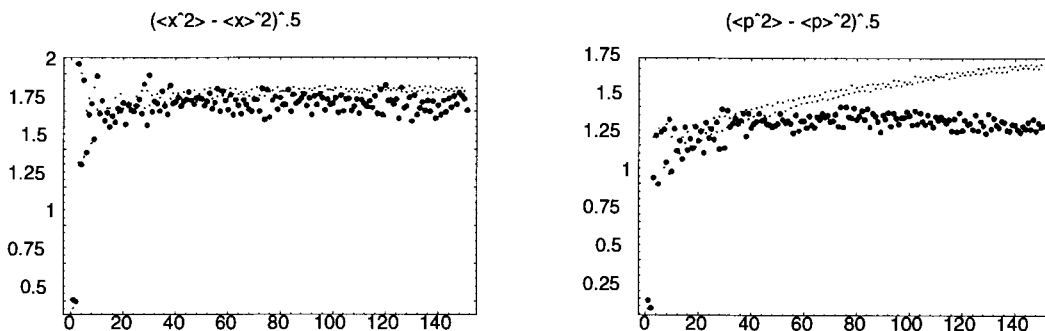


Figure 3.49: Standard deviations for momentum and position for the ensembles centered at $(-2.3, 0)$ for $\gamma = -0.5$, $\epsilon = 3$ and $c = 50$.

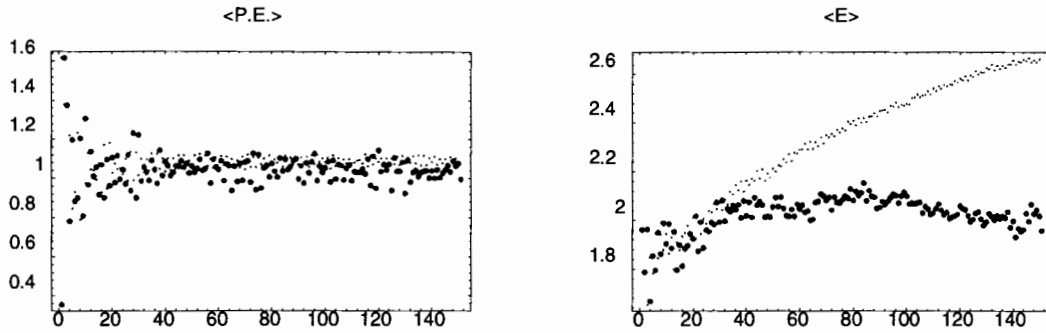


Figure 3.50: Chaotic B. Potential and total energy for the same ensembles as Figure 3.49.

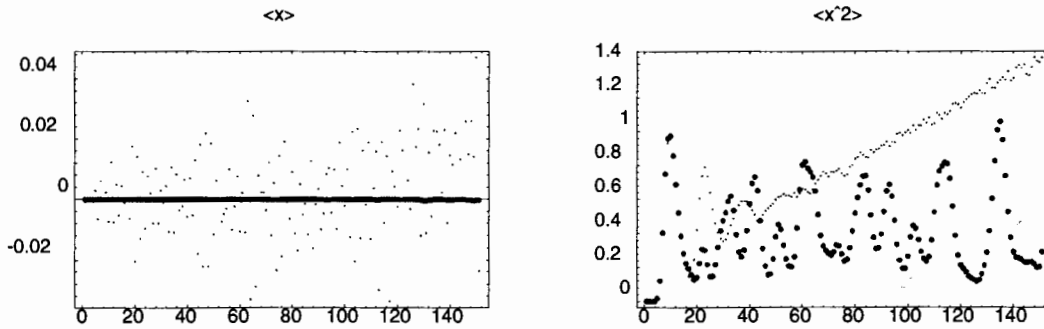


Figure 3.51: Resonant Expectation values of position and position squared for quantum and classical ensembles centered at $(0,0)$ for $\gamma = -.5$, $\epsilon = 2$ and $c = 100$. The Poincaré section is shown in Figure 2.4.

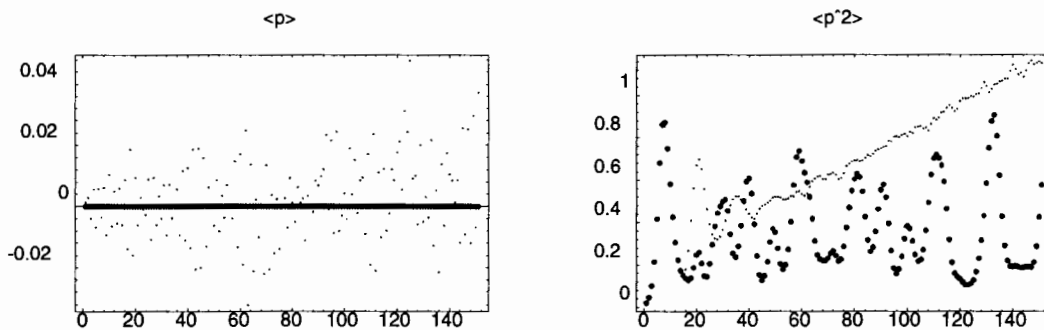


Figure 3.52: Resonant. Expectation values of momentum and momentum squared for the ensembles centered at $(0,0)$ for $\gamma = -.5$, $\epsilon = 2$ and $c = 100$. The Poincaré section is shown in Figure 2.4.

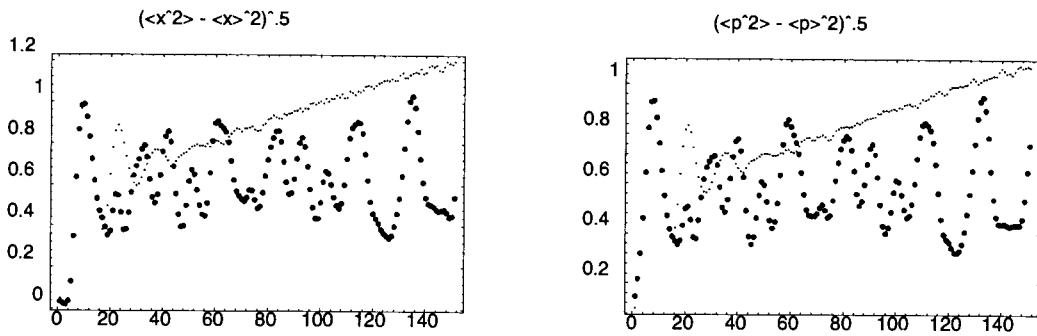


Figure 3.53: Resonant. Standard deviations for position and momentum for the ensembles centered at $(0,0)$ for $\gamma = -.5$, $\epsilon = 2$ and $c = 100$.

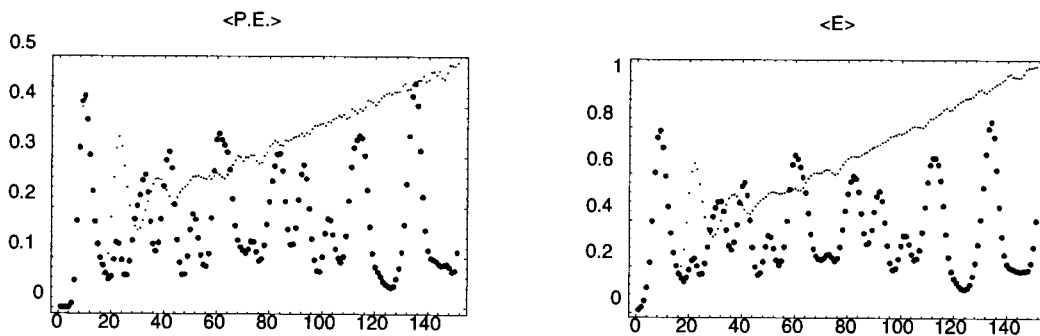


Figure 3.54: Expectation values for kinetic and total energy for the ensembles centered at $(0,0)$ for $\gamma = -.5$, $\epsilon = 2$ and $c = 100$.

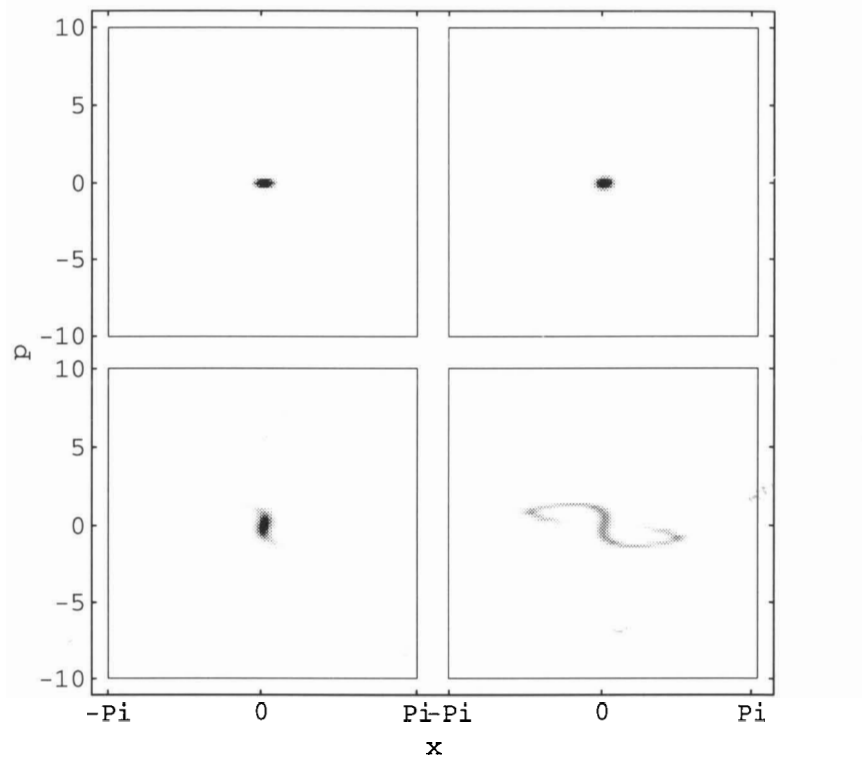


Figure 3.55: Resonant. Quantum probability distributions for the ensemble centered at $(0,0)$ for $\gamma = -0.5$, $\epsilon = 2$ and $c = 100$. Time runs from left to right starting at the top. The times are 0, 1, 4, and 8 periods of the driving force. The scale runs from black, .2 of the initial probability, to white, at zero probability.

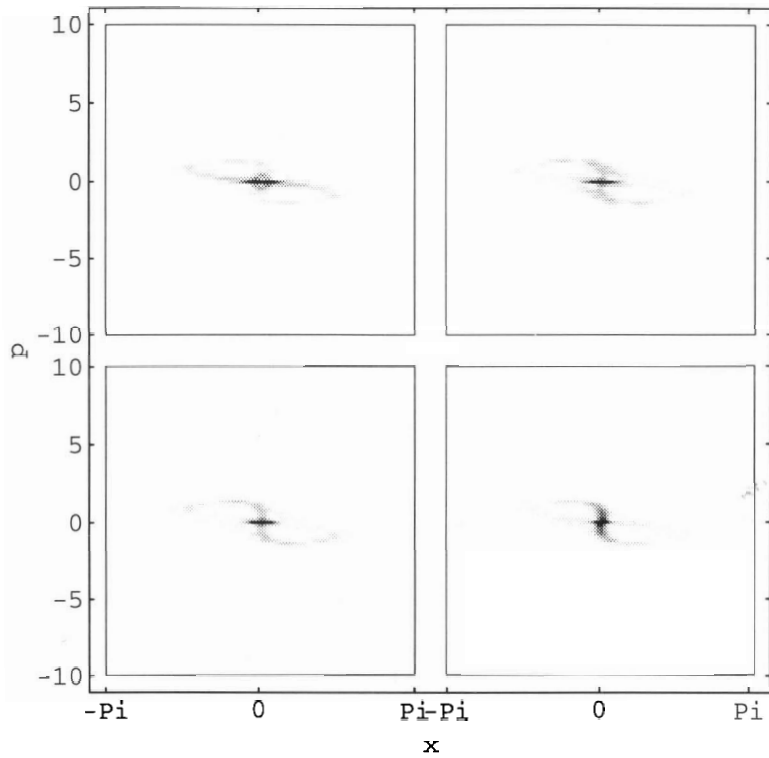


Figure 3.56: Resonant. Quantum probability distributions for the same ensemble as Figure 3.55. Time runs from left to right starting at the top. The times are 16, 48, 100, and 150 periods of the driving force. The scale runs from black, .2 of the initial probability, to white, at zero probability. The Poincaré section is shown in Figure 2.4.

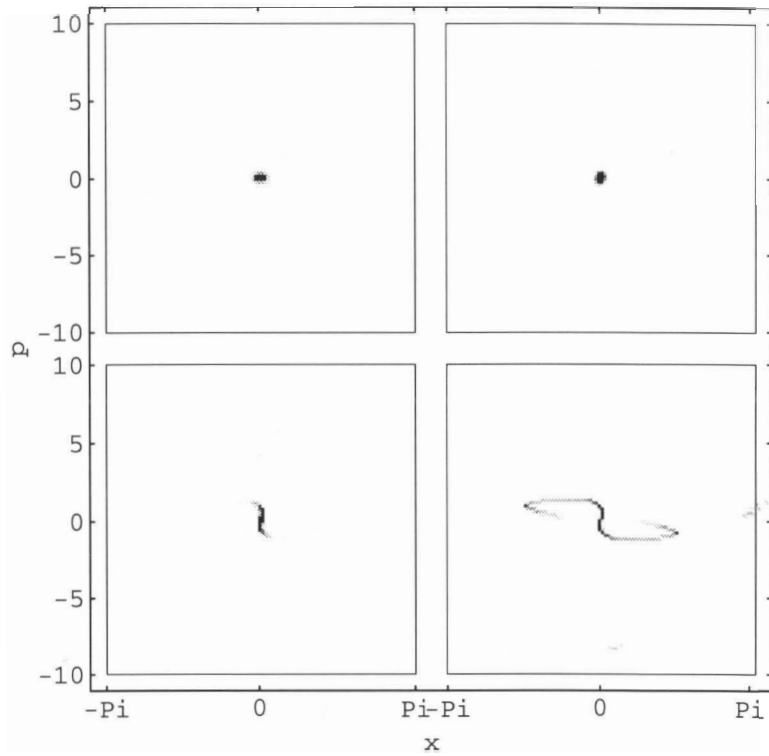


Figure 3.57: Resonant. Classical probability distributions for the same ensemble as Figure 3.55. Time runs from left to right starting at the top. The times are 0, 1, 4, and 8 periods of the driving force. The scale runs from black, .2 of the initial probability, to white, at zero probability. The Poincaré section may be found in Figure 2.4.

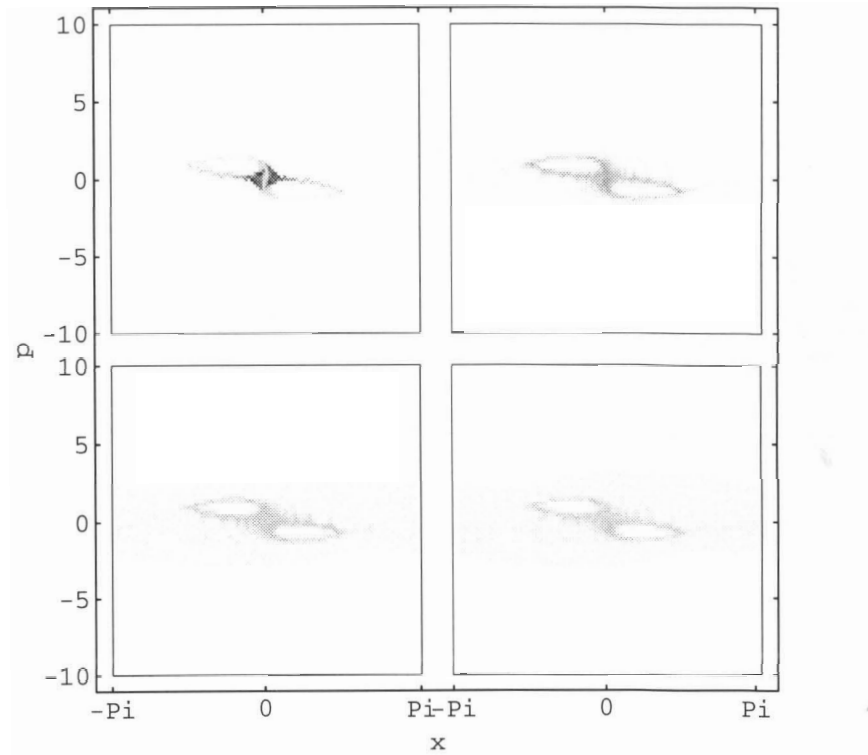


Figure 3.58: Resonant. Classical probability distributions for the same ensemble as Figure 3.57. Time runs from left to right starting at the top. The times are 16, 48, 100, and 150 periods of the driving force. The scale runs from black, .2 of the initial probability, to white, at zero probability.

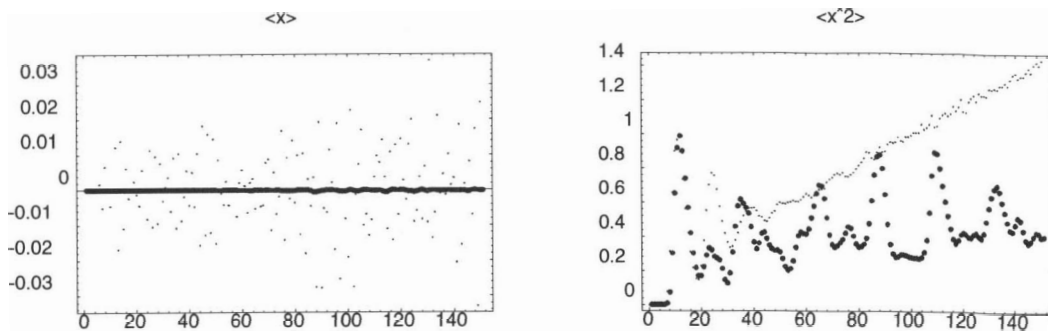


Figure 3.59: Resonant. Position and position-squared expectation values for quantum and classical ensembles centered at $(0,0)$ for $\gamma = -.5$, $\epsilon = 3$ and $c = 250$. The Poincaré section is shown in Figure 2.4.

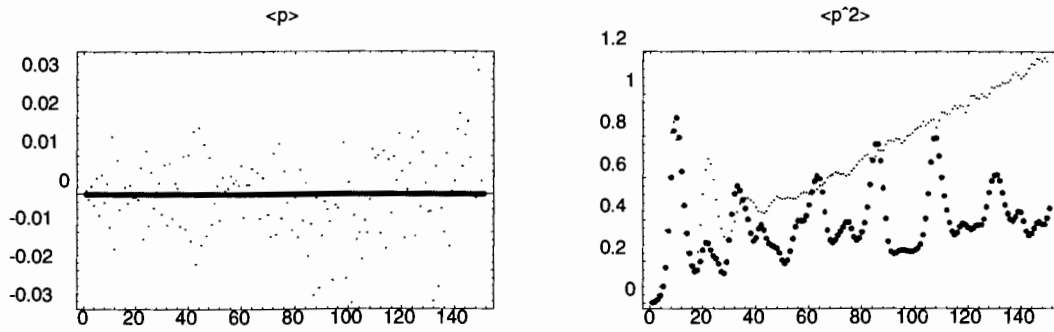


Figure 3.60: Resonant. Momentum and momentum-squared expectation values for the same ensemble as Figure 3.59.

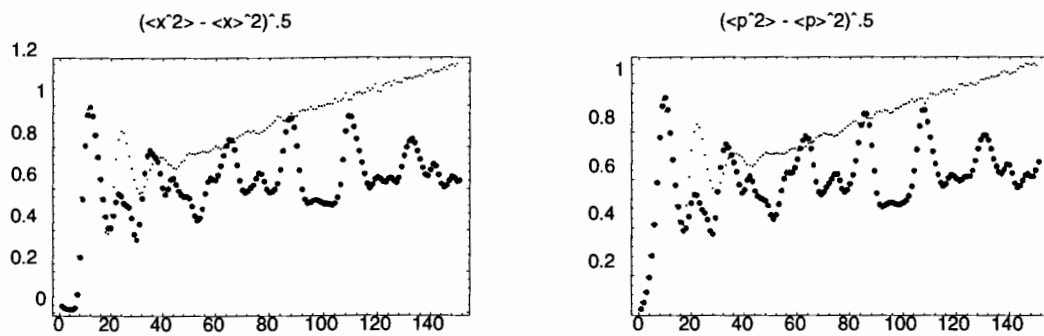


Figure 3.61: Standard deviation of position and momentum for the same ensemble as Figure 3.59.

Consider the discrete-position representation as it is treated numerically. The wavefunction in position representation is a complex-valued row vector with n elements, and the time-development operator is an unknown $n \times n$ matrix. This operator maps the wavefunction at period j to the wavefunction at period $j + 1$.

$$U_T \Psi_j(x) = \Psi_{j+1}(x) \tag{3.1}$$

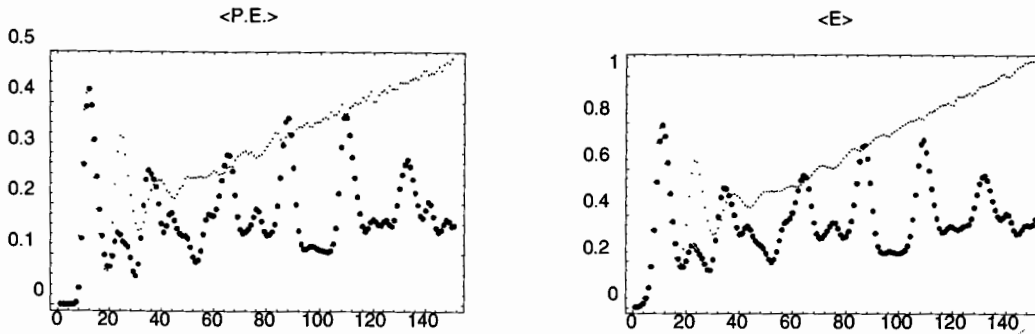


Figure 3.62: Kinetic and total energy expectation values for the same ensemble as Figure 3.59.

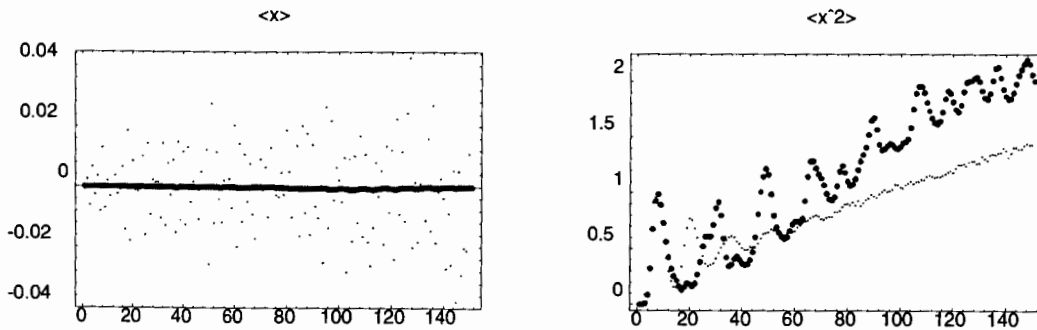


Figure 3.63: Expectation values of position and position-squared for quantum and classical ensembles centered at $(0,0)$ for $\gamma = -0.5$, $\epsilon = 3$ and $c = 50$.

Though the $n \times n$ matrix is unknown, the $\Psi_j(x)$ and $\Psi_{j+1}(x)$ are known by numerically integrating Schrödinger's equation. Thus, equation 3.1 is n equations, in n^2 unknowns. In order to have n^2 equations we need n versions of equation 3.1. That

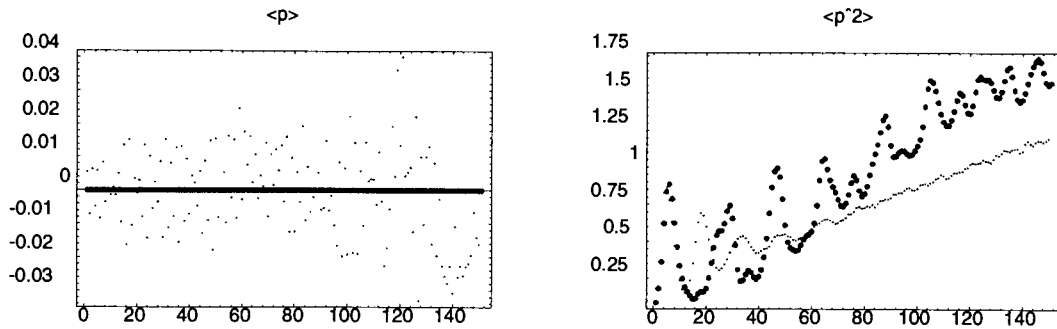


Figure 3.64: Resonant. Expectation values of momentum and momentum-squared for the same ensembles as Figure 3.63

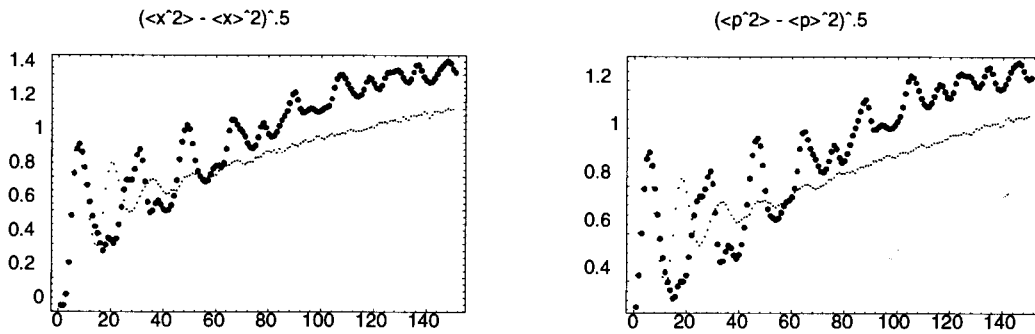


Figure 3.65: Standard deviations for position and momentum for the same ensemble as Figure 3.63.

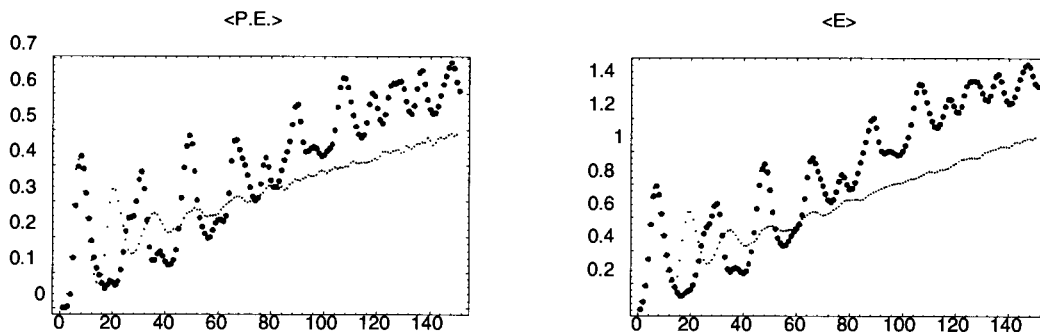


Figure 3.66: Resonant. Kinetic and total energy expectation values for the same ensembles as Figure 3.63.

is, the value of the wavefunction over n periods of the driving force. Solving this set of n^2 equations, we have the unknown matrix, U_T . Then, it is possible to solve for its eigenvalues and vectors: the quasienergy values and functions. The difficulty was that, for $c = 100$, a grid length of $n = 2048$ was required to contain the higher momenta. (See section 2.2.1.) This procedure then requires the system to be numerically propagated for 2048 periods of the driving frequency; this was not feasible. It was feasible to propagate the wave function for 128 periods of the driving potential, as was done for $c = 50, 100, 250$. The difficulty then, is that in order to fit in the higher momenta on a 128 point line, c must be reduced to about 15. At this point, the wavefunction became sufficiently broad in position and momentum that it could not be localized enough to display the behaviour that was wanted.

The effect of U_T , namely to advance the wavefunction one drive period in time, is known and easily calculable numerically. Thus, the one thing that may be calculated from the wavefunctions is the expectation value of the time-development operator. This was the only information about the quasienergy spectrum of the quantum ensemble that I was able to calculate.

The expectation value of the quasienergy is given by:

$$\langle U_T \rangle = \int_{-\pi}^{\pi} \Psi^*(x, nT) U_T \Psi(x, nT) dx \quad (3.2)$$

where we consider the wave function after n periods of the driving function. Operating U_T on Ψ gives:

$$\langle U_T \rangle = \int_{-\pi}^{\pi} \Psi^*(x, nT) \Psi(x, (n+1)T) dx \quad (3.3)$$

This can be implemented numerically quite easily by converting the integral to a sum. From this, $\langle U_T \rangle$ is seen to be a complex number whose magnitude gives the probability that the wavefunction returns back to itself (or itself multiplied by a phase) after one period of the drive function. Invoking the quasienergy representation sheds further light on the properties of this value.

As in equation 1.3, we may represent the wavefunction at any time in terms of the quasienergy eigenfunctions. Whereupon equation 3.3 becomes

$$\langle U_T \rangle = \int_{-\pi}^{\pi} \left(\sum_E e^{iEnT/\hbar} A_E^* \psi_E^*(x) \right) \times \left(\sum_E e^{-iE(n+1)T/\hbar} A_E \psi_E(x) \right) dx \quad (3.4)$$

Centre	Dynamics	Magnitude	Phase
(-1.0,0.0)	Regular	≈ 0	N/A
(-1.5, 0)	Regular	≈ 0	N/A
(0.1, 0)	Regular	.37415	.114469
(-1.7,-3)	Regular	.62393098	1.63971745
(1.7,3)	Regular	.62393098	1.63971745
(0,0)	Regular	.90990324	1.0855218
(-2.3, 0)	Chaotic	1.34×10^{-8}	.834
(-3, -1.7)	Chaotic	≈ 0	N/A

Table 3.2: Magnitude and phase of $\langle U_T \rangle$ for various initial conditions when $\gamma = -.5$ and $\epsilon = 3$. Zero values are meant as zero to within machine precision, *i.e.* of the order of 10^{-14} . The number of digits quoted is the number which were constant over the first five periods.

Here, as in equation 1.3, $\psi_E(x)$ are the eigenfunctions of quasienergy E and the A_E are the time zero expansion coefficients. The quasienergy eigenfunctions are orthogonal.[29] All the cross terms vanish leaving only

$$\langle U_T \rangle = \sum_E \left(e^{-iET/\hbar} |A_E|^2 \int_{-\pi}^{\pi} |\psi_E(x)|^2 dx \right) \quad (3.5)$$

The eigenfunctions of quasienergy are all normalized, thus the integrals in the sum all equal one. This demonstrates that $\langle U_T \rangle$ is independent of time. (T is the period of the Hamiltonian, and thus does not depend on time.) From this it may be seen that the probability that the system returns to its previous state after one driving period is constant. We may interpret equation 3.5 as the sum of the exponentials of the quasienergies each multiplied by its probability. Thus, when the value of $|\langle U_T \rangle|^2$ is close to one it will be the result of one of the following situations. There is a large probability that the system is in a single quasi-energy state and a small probability for the others, or, there is a similar probability for the system to be in several quasienergy states which have closely spaced quasienergies. When $|\langle U_T \rangle|^2$ is close to zero it will be due to either a superposition of a large number of quasienergy states (many phases) or of a few (or one) pairs that are nearly exactly out of phase.

The calculated values of $\langle U_T \rangle$ using equation 3.3 are shown in Table 3.2, for a variety of initial conditions. These results were not as illuminating as one might hope.

The points $(-1.7, -3)$ and $(1.7, 3)$ had the same energy and are also in identical areas of regular orbits. It is likely the second of these things that lead to their identical average quasienergy. Dividing the list into zero and non-zero values shows that this property was not an indication of chaotic or non-chaotic dynamics.


These results do show a difference in the quasienergy spectrum of the $(-2.3, 0)$ and the $(-3, -1.7)$ ensembles. That, by itself, was not enough to tell whether the quasienergy eigenstates that make up the ensembles were different or not, only that, at the very, least the probability of the quasienergies was different. However, the eigenstates contributing to these wavefunctions must have been different because both wavefunctions may be written in the form of equation 1.3. If they differed only by the initial probability coefficient then given enough time they would dephase enough so that the initial destructive interference that was keeping the wavefunction localized would dissipate. The wavefunction would be allowed to explore all momenta which were contained in the quasienergy eigenfunctions. Since the two wavefunctions differed in their ability to reach higher momenta they could not contain only the same quasienergy states.

In the Resonant case centred at $(0, 0)$ with $\gamma = -.5$ and $\epsilon = 2$, see Figures 3.63–3.66, the classical-ensemble expectation values grew faster for $c = 100$ and 250 than the quantum values. This was reversed when c was lowered to 50. This suggests that the form of the quasienergy eigenfunctions is not simply related to c . The results in the Chaotic A and Chaotic B case suggested that the quasienergy expansion was better able to mimic the classical behaviour as c increased and the system became more classical. The Resonant case shows that it is generally not that simple.

Chapter 4

Coupled Pendula

4.1 The Classical System

 In two dimensions, the physically simplest autonomous system that can display chaos is almost certainly the double pendulum: a two-pendulum system where the second pendulum pivots on the bob of the first.[13] The difficulty with this system is that the potential energy of the bottom pendulum depends on the position of the top pendulum. Which is to say that the Hamiltonian cannot be written as only two functions: one of position and one of momentum. Because of these cross terms in the Hamiltonian, it can not be treated by the split-operator method, see section 2.2.1. The coupled pendula model was chosen to avoid this difficulty; it is a simple system that can display chaos and that can be treated by the split-operator method. The two coupled pendula system is two pendula with independent fixed pivots whose bobs are joined by a linear spring. Numerical investigation of this system gave Poincaré sections which display chaotic and regular behaviour.

The displacement of each pendulum may be described by a function $\theta_i(\tau)$, $i = 1, 2$. Here τ is time and $\theta \in [-\pi, \pi]$. The same sign and periodic boundary condition conventions are used for each pendulum. They are also the same as those used for the driven pendulum in section 2.1. As was done for the driven pendulum, we will use dimensionless units of time by taking time in units of the natural frequency of

the first pendulum: $t = \sqrt{\frac{\ell}{g}}$. Here, g is the magnitude of the gravitational field, and the length of the first pendulum is ℓ . All other lengths in the system will be described by their proportion to this length. Thus, the second pendulum's length is $\alpha\ell$. The distance between the pivots is $\gamma\ell$. The unstretched length of the spring is $\delta\ell$. The mass of the first bob is m , and that of the second is βm . Continuing the transition to dimensionless units, we change displacement to $y_i(t) = \theta_i(\tau)$, $i = 1, 2$. The spring-constant of the spring, k , will be replaced with $e = \frac{k\ell}{mg}$.

The system is shown in Figure 4.1.

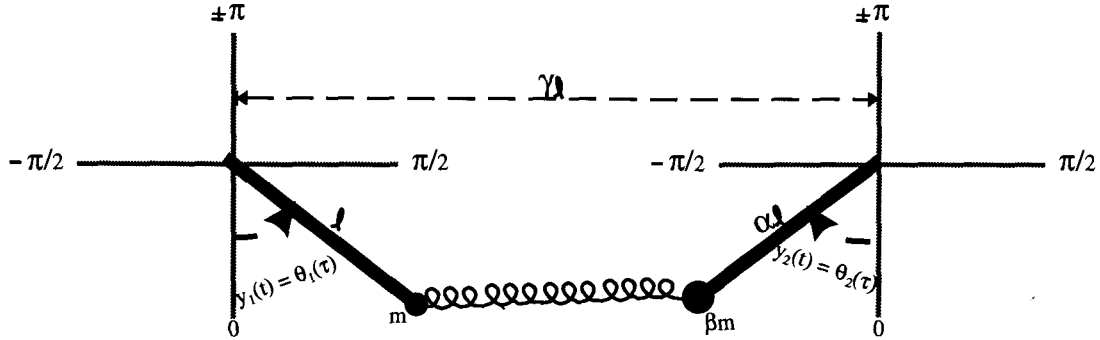


Figure 4.1: The coupled pendula system. The relative lengths of the pendula match the parameters used. The unstretched length of the spring is $\delta\ell$ and the dimensionless spring constant is $e = \frac{k\ell}{mg}$. The relative sizes of the bobs corresponds to their relative masses.

Making the same substitutions for momentum and the Hamiltonian as in the driven pendulum, gives the dimensionless Hamiltonian:

$$\mathcal{H} = \frac{p_1^2}{2} + \frac{p_2^2}{2\alpha^2\beta} + \cos y_1 + \alpha\beta \cos y_2 + e(\delta - G)^2 \quad (4.1)$$

Here

$$G = \{1 + \alpha^2 + \gamma^2 - 2\gamma(\sin y_1 - \alpha \sin y_2) - 2\alpha \cos(y_1 - y_2)\} \quad (4.2)$$

The dimensionless classical equations of motion are:

$$\ddot{y}_1 = -\sin y_1 - e\{A_1(1 - \delta G^{-1/2})\} \quad (4.3)$$

$$\ddot{y}_2 = -\frac{\sin y_1}{\alpha} - \frac{e}{\alpha^2\beta}\{A_2(1 - \delta G^{-1/2})\} \quad (4.4)$$

$$A_1 = 2(-\gamma \cos y_1 + \alpha \sin(y_1 - y_2)) \quad (4.5)$$

$$A_2 = 2(\alpha\gamma \cos y_2 - \alpha \sin(y_1 - y_2)) \quad (4.6)$$

This allows us to consider the mass and length of the first pendulum to be identically one, and the Greek letters as the other lengths and mass, or we may consider the Greek letters as the ratio between the other lengths and mass of the system to that of the first pendulum.

4.1.1 Classical Numerical Methods

The classical equations of motion were numerically integrated to give the positions and momenta as a function of time. An Adams method variable-order variable-time-step ordinary-differential-equation integration routine from the NAG library (D02QFF) was used.[31] As in the case of the driven pendulum, the value for the tolerance was determined by comparing the analytical and numerical results for a two-dimensional harmonic oscillator. However, this gave little reassurance that the routine was working for the coupled pendulum system. A much more compelling test of the accuracy was the comparison of the numerical results from the classical and quantum case as shown in chapter 5.

4.1.2 Classical Dynamics

This system displays a great variety of dynamical behaviours. The following parameter values were studied: $\alpha = .9$, $\beta = 1.4$, $\gamma = .6$, $\delta = 1.6$, $e = 1.7$. The system as it is shown in Figure 4.1 shows these relationships, in that it is drawn with all the correct relative lengths, and the size of the bobs are relative to their mass. The Poincaré section in Figure 4.2 was taken to be the y_1, y_2 plane when the time derivative of the distance between the bobs is passing through zero in the positive direction ($\dot{G} = 0$). Three co-ordinates are sufficient to specify a unique point in this four-dimensional phase space because energy is conserved. This choice of the third co-ordinate, which places the section, is not as odd as it seems. This is one of the few sections through which all orbits must pass. This is not true of simpler, and easier to visualize, choices such as $y_1 = 0$ or $y_2 = 0$. The potential that gives rise to these trajectories consists of a trough with many local minima along its bottom. Displaying only the area within $[-\pi, \pi]$ along each axis and imposing periodic-boundary conditions gives Figures 4.3

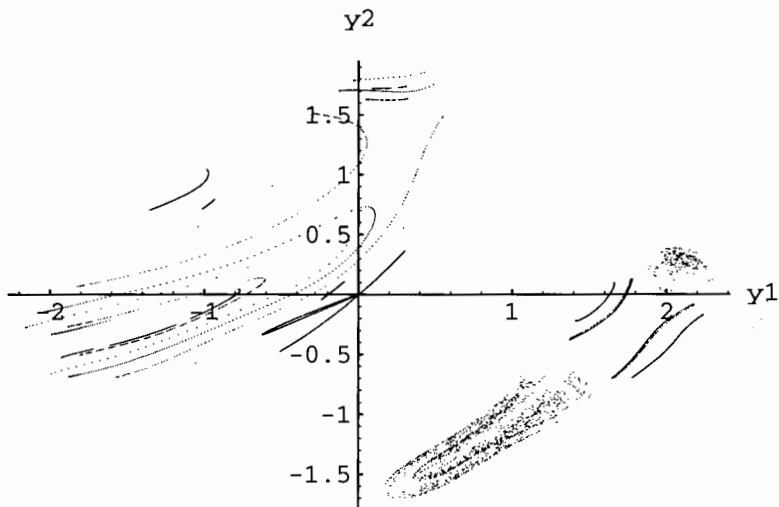


Figure 4.2: Poincaré section for the coupled pendula system when $\alpha = .9$, $\beta = 1.4$, $\gamma = .6$, $\delta = 1.6$, $e = 1.7$.

and 4.4. We may also consider the potential to consist of a double well and a single well divided by a central ridge. The two wells are joined at their ends by the boundaries. The minimum of the potential occurs at -2 .

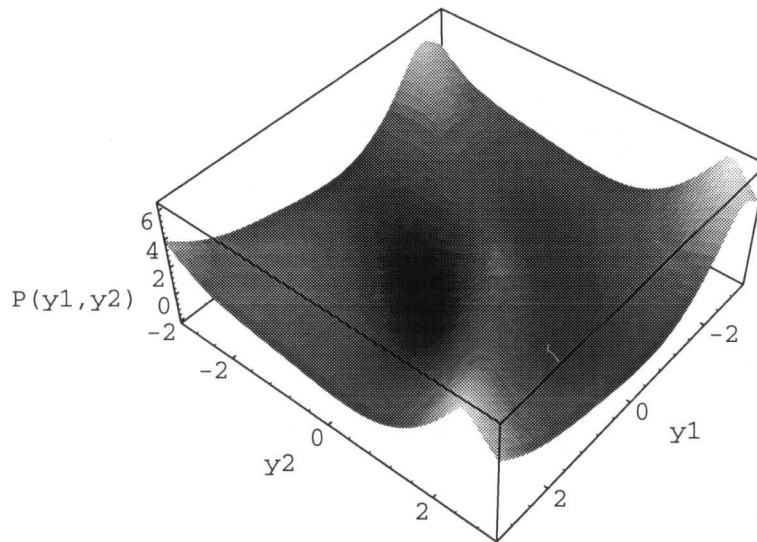


Figure 4.3: Potential for the coupled pendula system with the same parameters as in Figure 4.2.

As can be seen from the Poincaré section in Figure 4.2, the coupled-pendula system displays both regular and chaotic behaviours. The three-dimensional trajectories that give rise to these sections are shown in Figures 4.5–4.10. Here the particles position in three-space is plotted. The three coordinates chosen were (y_1, y_2, \dot{G}) . The trajectories (all of energy -0.55) are quasiperiodic (Figures 4.5, 4.8, 4.8, 4.9, and 4.10) or chaotic (Figures 4.6 and 4.7). All of these trajectories consist of oscillatory motion of both pendula. Neither pendulum makes any complete rotations. The quasi-periodic behaviour occurs in the double well which is on the positive- y_2 of the central ridge in

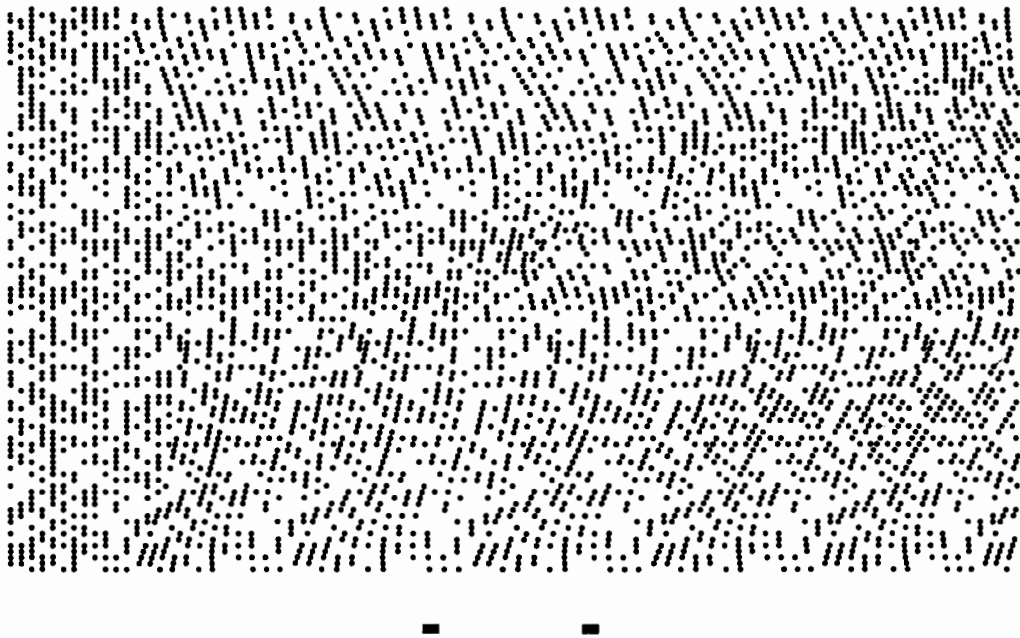


Figure 4.4: A random dot stereogram of the coupled pendula potential. The image may be seen by focusing one's eyes behind the page. An inside-out image may be seen by focusing in front of the page. The axes run from $-\pi$ to π , y_1 runs from left to right and y_2 from bottom to top.

the potential. In the single well, the chaotic behaviour occurs. Due to the periodic-boundary conditions it is possible for a single trajectory of sufficient energy to visit both wells without crossing the central ridge.

The trajectory shown in Figure 4.10 is especially interesting because the surface on which the trajectory travels *appears* to intersect itself. However, the invariant surface that the trajectory travels along may not actually intersect itself. In this case, the surface is not continuous, but takes the form of a cantor set, thus avoiding intersecting itself. A cross section of the trajectory is shown in Figure 4.11.

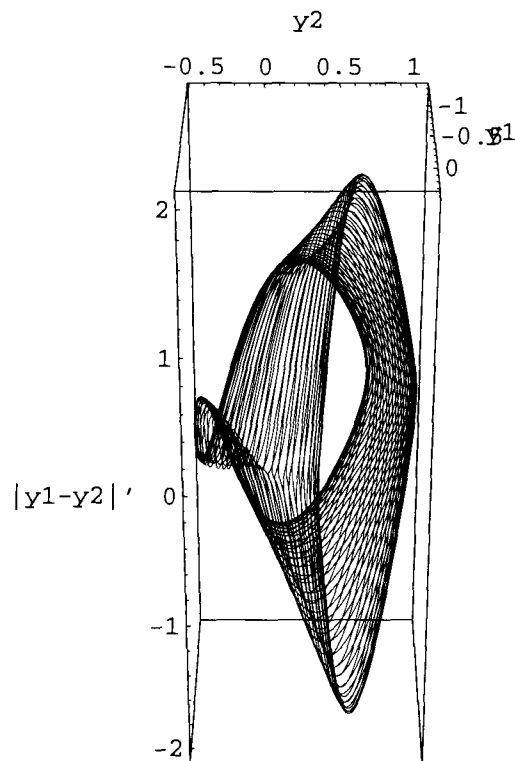


Figure 4.5: Quasi-periodic trajectory with initial conditions $y_1 = .3$, $y_2 = .36$, $p_1 = p_2 = 0$

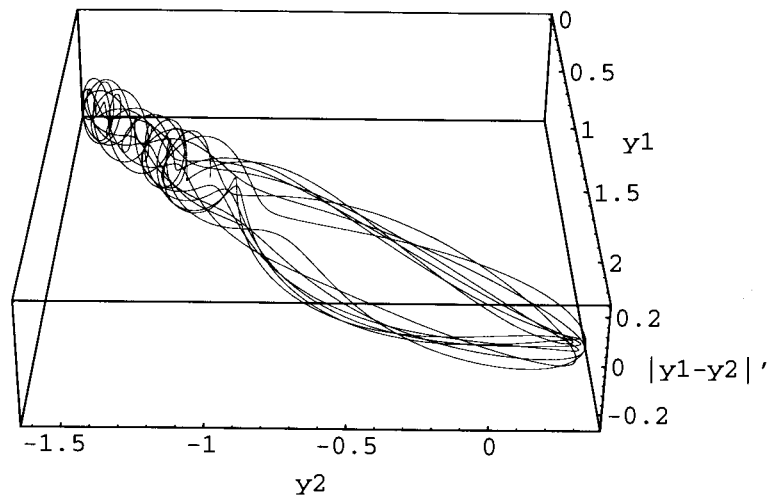


Figure 4.6: Chaotic trajectory with initial conditions $y_1 = .5$, $y_2 = -1.5$, $p_1 = p_2 = 0$

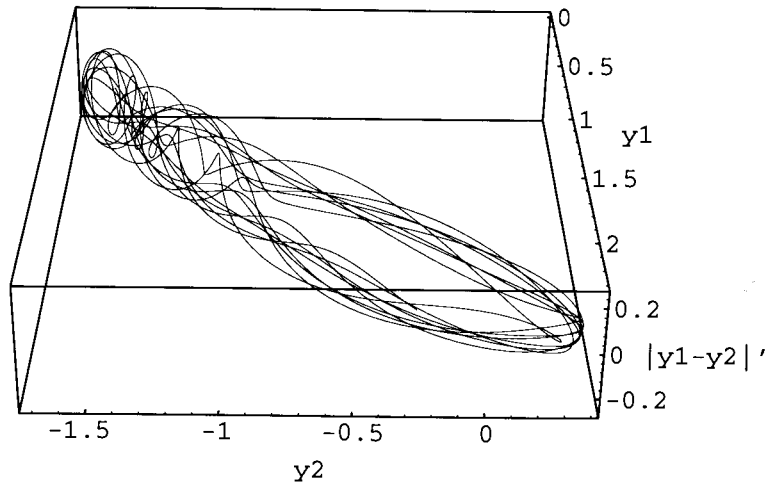


Figure 4.7: Chaotic trajectory with initial conditions $y_1 = 2.0$, $y_2 = .38$, $p_1 = p_2 = 0$

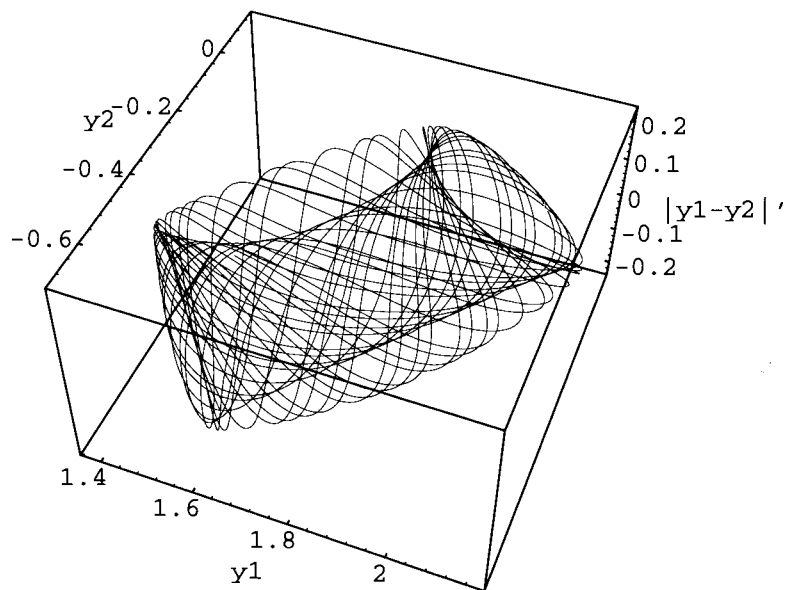


Figure 4.8: Quasi-periodic trajectory with initial conditions $y_1 = 1.7$, $y_2 = -0.3$, $p_1 = 0.5$, $p_2 = 0$

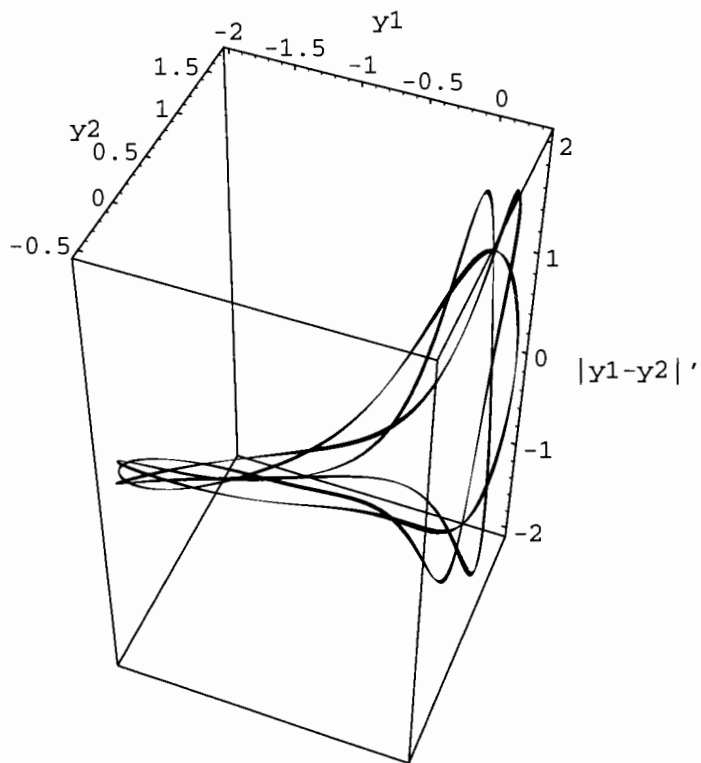


Figure 4.9: Quasiperiod 3 trajectory with initial conditions $y_1 = -1.8$, $y_2 = -0.4$, $p_1 = -0.6$

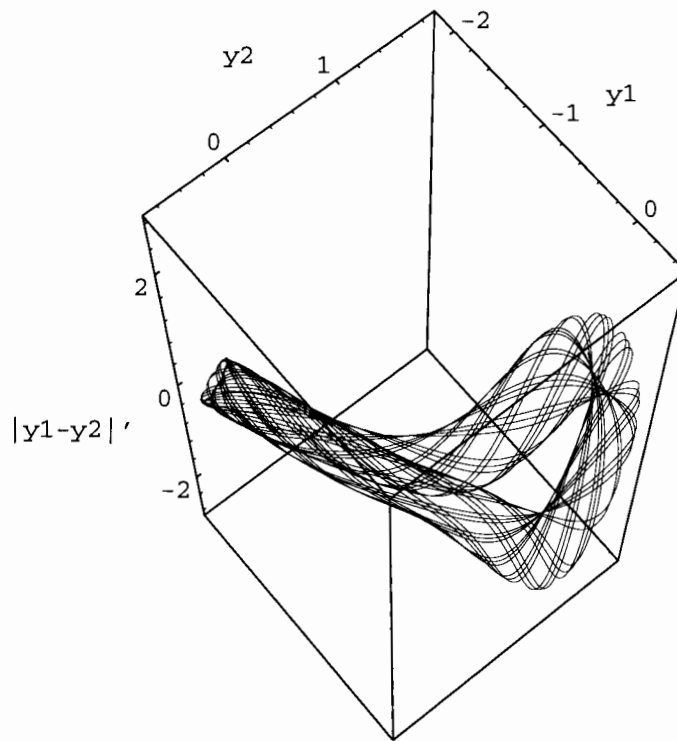


Figure 4.10: Quasi-periodic trajectory with initial conditions $y_1 = -2.0$, $y_2 = -.66$

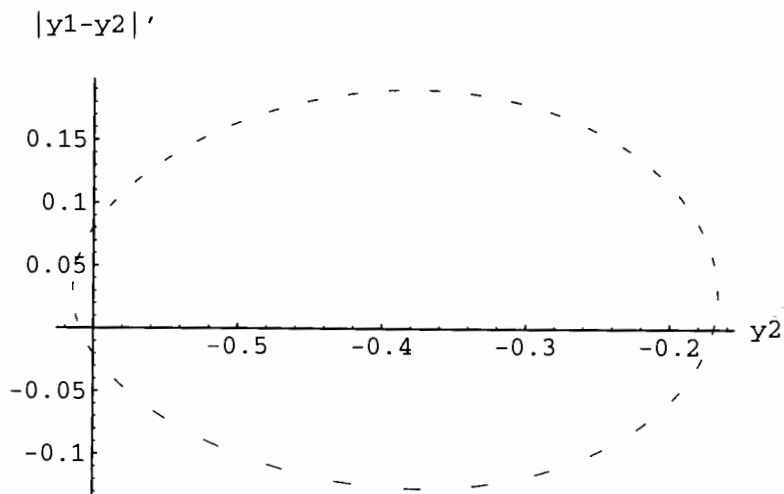


Figure 4.11: A section through the quasi-periodic trajectory shown in Figure 4.10. The slice is taken when $y_1 = 1.85$ and $\dot{y}_1 > 0$.

4.2 The Quantum System

The dimensionless classical Hamiltonian (equation 4.1) was taken directly into quantum representation, by letting the classical variables (y_1, y_2, p_1, p_2) become quantum operators with the usual meaning.

The initial wavefunction was chosen as a two-dimensional Gaussian in position space at time $t = 0$:

$$\Psi(y_1, y_2, 0) = (s\sqrt{2\pi})^{-1} e^{\frac{i}{c}(k_{1o}y_1 + k_{2o}y_2)} e^{-\frac{(y_1 - y_{1o})^2 - (y_2 - y_{2o})^2}{4s^2}} \quad (4.7)$$

This is a two-dimensional Gaussian centred in position space at (y_{1o}, y_{2o}) with a width in both directions of s . The centre in momentum space is $c^{-1}(k_{1o}, k_{2o})$, with a width $(2sc)^{-1}$ in both momenta. The Husimi distribution was not invoked for this system because the time to do each calculation was several hours. It seemed sufficient to compare the theories in position space, especially since the two position operators commute so there was no \hbar limit to the area which could be resolved.

4.2.1 Quantum Numerical Methods

The wave function was propagated using the two-dimensional split-operator method.[34] The only difference from the one dimensional case (outlined in section 2.2.1) was the replacement of x and p by two-dimensional vector operators. In this case, the two-dimensional Fast-Fourier-Transform routine (C06FJF) from the NAG library was used.[31] As in the one-dimensional case the accuracy was determined by adjusting the time-step size and the grid spacing. The value for these was chosen by comparison between the numerical and analytical solutions for the harmonic oscillator. These values were confirmed by the agreement of the two methods (quantum and classical) in the case of the two-dimensional simple pendulum. The two-dimensional FFT is very slow for large grid sizes: the largest practical grid was 128×128 . With this size grid and appropriate time-step it took about one day to propagate the wavefunction the equivalent of one small-angle period of the unit pendulum in time.

In order to keep the wavefunction in momentum space confined on so small a grid it was necessary to choose $c = 15$. (Recall the maximum value of momentum for a

grid of length n , is $\pm \frac{n}{2c}$.)

4.2.2 Quantum-Classical Comparison

To compare the two theories for the coupled pendula system, ensembles were again used. The quantum ensemble was the two-dimensional wave function in position space. This was compared with a classical ensemble whose initial coordinates in the four-dimensional phase space had the same probability distribution as the quantum probability distributions in position and momentum representation. This was done using the random number generator G05DDF from the NAG library.[31] The comparison was then made between the two-dimensional probability distributions in position space, and between the expectation values. The quantum probability distribution is the squared amplitude of the wavefunction. The classical probability distribution was created by dividing the position space into a grid of 100 squares on a side. The number of points in each bin divided by the number of points in the ensemble gave the classical probability for each bin.

The expectation values were calculated as in the one-dimensional case, the difference being that all the sums and integrals were made over two variables.

Chapter 5

Results for the Coupled Pendula System

Quantum and classical ensembles were propagated for times up to thirty unit-pendulum-small-angle-periods. (Hereafter simply referred to as periods or T .) The reason for the short time is two-fold: nothing much of interest happened after the first few periods, and the long computational time for which the quantum system needed to run. (Thirty periods represents around a month of computer time.) The position probability distributions and expectation values were calculated for both ensembles. The expectation values calculated included y_1 , y_2 , p_1 , p_2 , the square of these operators, the standard deviation of these distributions, the total kinetic and potential energy and, by addition, the total energy.

Classical ensembles with identical position and momentum probability distributions (i.e. minimum uncertainty Gaussians) were propagated for a single value of $c = 15$. The width of these Gaussians in both directions in position space (s in equation 4.7) was 10^{-1} . The width in momentum space (again, in both directions) was then 6.6×10^{-2} . The two ensembles were started with zero average momentum for each pendulum and an initial position of $(-2.0, -0.66)$ and $(.5, -1.5)$. The first was in the classically regular regime. A single classical trajectory with the same initial conditions is shown in Figure 4.10. The second was in the chaotic area. A single classical trajectory with the same initial conditions is shown in Figure 4.6. A single

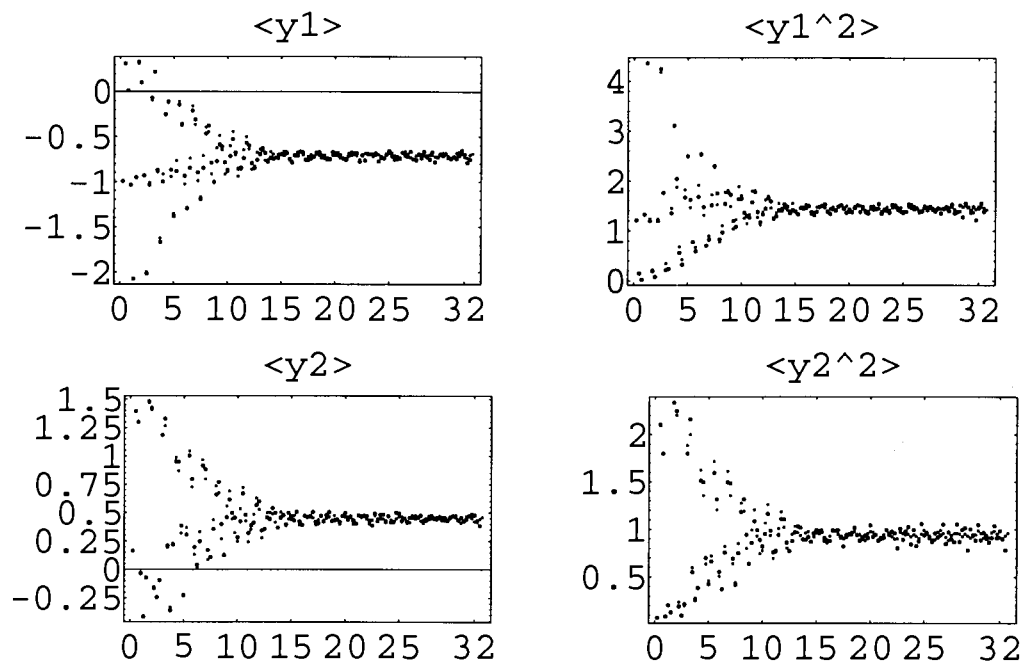


Figure 5.1: The position and position squared expectation values calculated for classical and quantum ensembles initially centered at $(-2.0, -0.66)$, in the quasiperiodic regime, with zero average momentum as a function of time. The large dots are the quantum values and the small dots are the classical values.

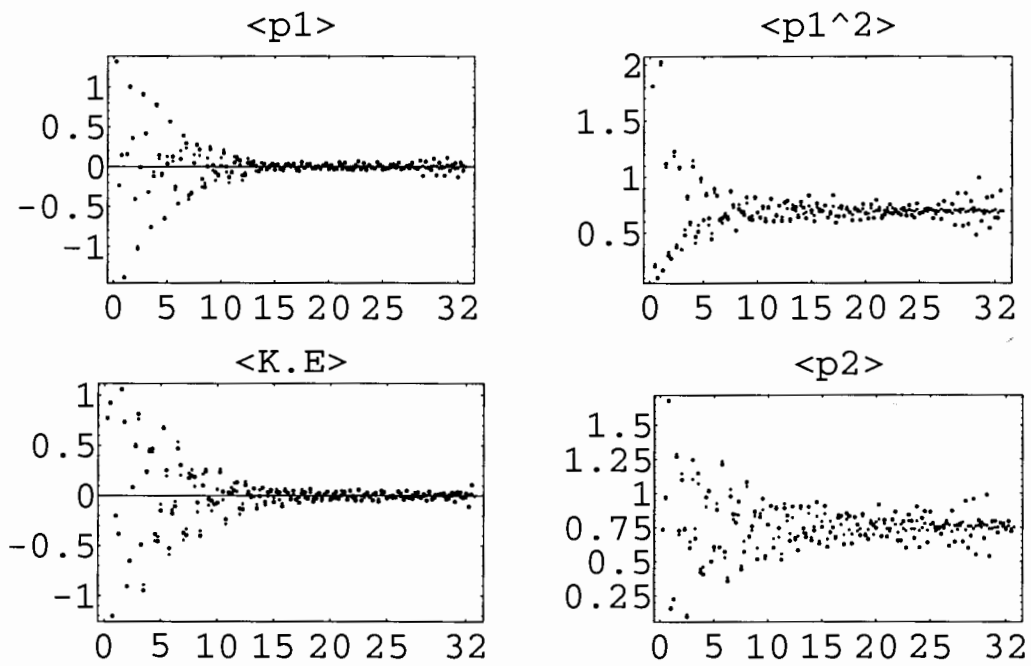


Figure 5.2: The expectation values of momentum and momentum squared, calculated for the quasiperiodic ensembles in Figure 5.1

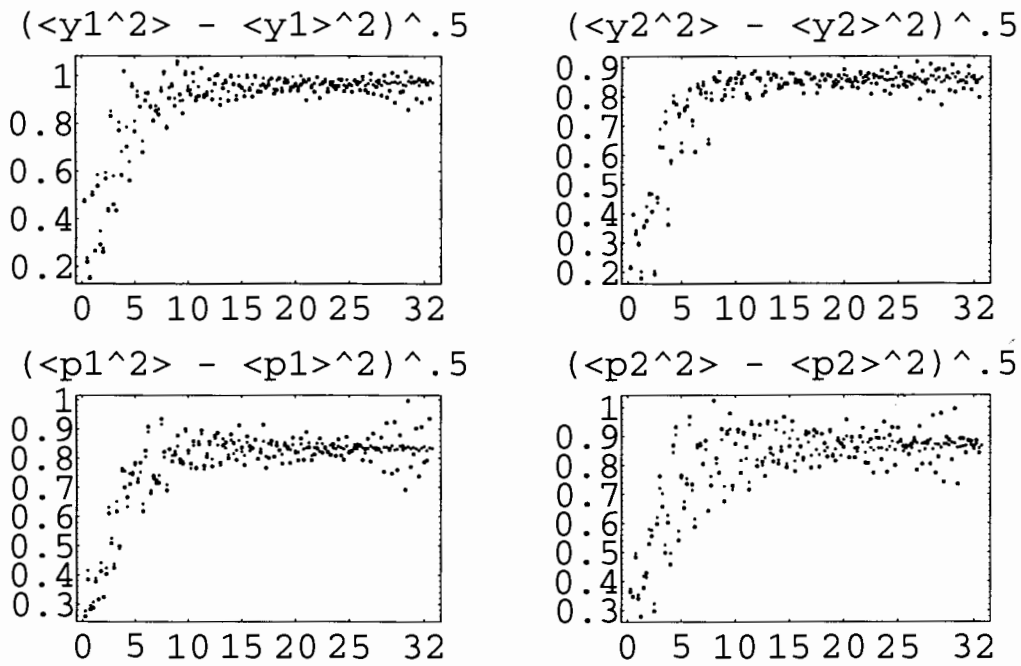


Figure 5.3: The standard deviations for position and momentum, calculated for the quasiperiodic ensembles in Figure 5.1

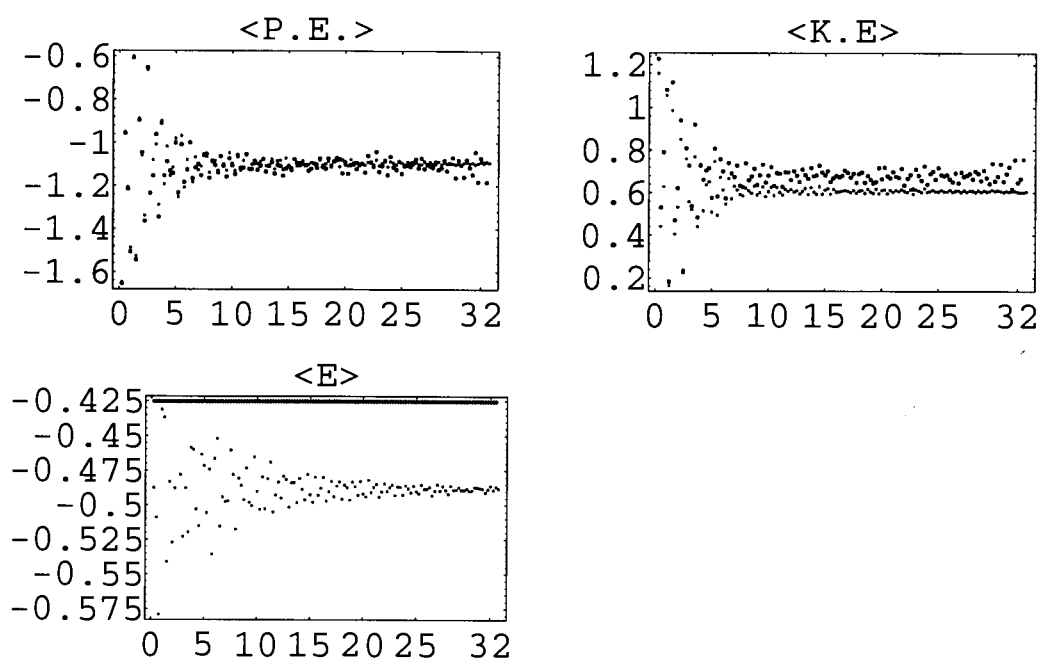


Figure 5.4: The potential, kinetic, and total energy expectation values, calculated for the quasiperiodic ensembles in Figure 5.1

particle with these initial conditions would have a classical total energy of $-.55$. The average energy of these ensembles, however, was $-.43$ in the first case, and $-.20$ in the second. The minimum of the potential was -2.0 .

To get an order of magnitude estimate of the number of energy states excited by these ensembles, assume that the energy spacing for this potential may be approximated by the harmonic oscillator energy levels. In dimensionless units, the harmonic oscillator energy levels ($\hbar\omega$) are c^{-1} . Thus the number of energy states excited was around 23 for the quasiperiodic ensemble and around 27 for the chaotic ensemble. Given that this is an order of magnitude argument, they may be said to have been composed of similar numbers of energy eigenfunctions.

A classical trajectory started at $(-2.0, -.66)$ behaves quasiperiodically as demonstrated in the Poincaré section shown in Figure 4.2 and the trajectory in Figure 4.10. The second initial condition, $(.5, -1.5)$, leads to a chaotic trajectory as seen on the same Poincaré section and in Figure 4.7.

For the quasiperiodic ensemble all of the the quantum and classical expectation values calculated agree – excepting interference effects. This is shown in Figures 5.1, 5.2, 5.3, 5.4. This agreement is also good evidence that the accuracy of the numerical routines is sufficient for these purposes. The agreement between expectation values is supported by the actual probability distributions in position space, see Figures 5.9–5.12. The one exception to the close agreement of the two sets of expectation values is that of the energy. This suggests that the classical method was not as accurate as the quantum one, although it was accurate enough that the rest of the expectation values agreed.

For the ensemble started in the chaotic area of position space the results are similar. Both the expectation values (see Figures 5.5, 5.6, 5.7, and 5.8) and the probability distributions (see Figures 5.13–5.16) agree well, excepting interference effects. Here there was also the same discrepancy in the classical energy, presumably for the same reason.

In the regular regime the wavefunction reached its maximum extension in position and momentum after 10 periods. The chaotic ensemble achieved the same thing in around 3 or 4 periods. The faster expansion of the chaotic ensemble was to be expected

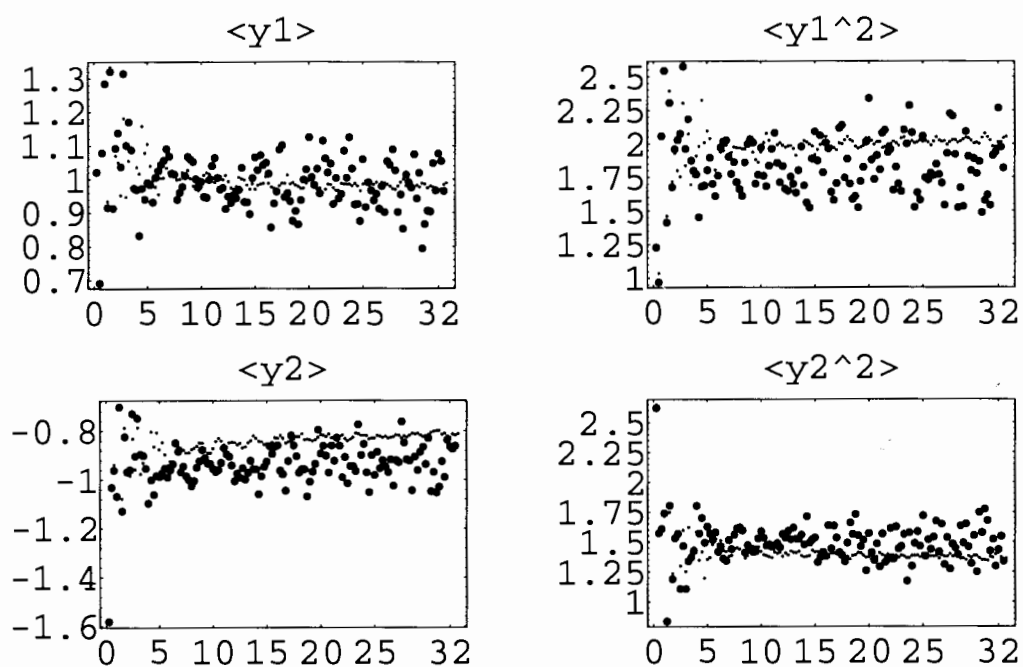


Figure 5.5: The position and position squared expectation values calculated for classical and quantum ensembles, initially centered in the chaotic regime at $(.5, -1.5)$ in position, with zero average momenta, as a function of time. The large dots are the quantum values and the small dots are the classical values.

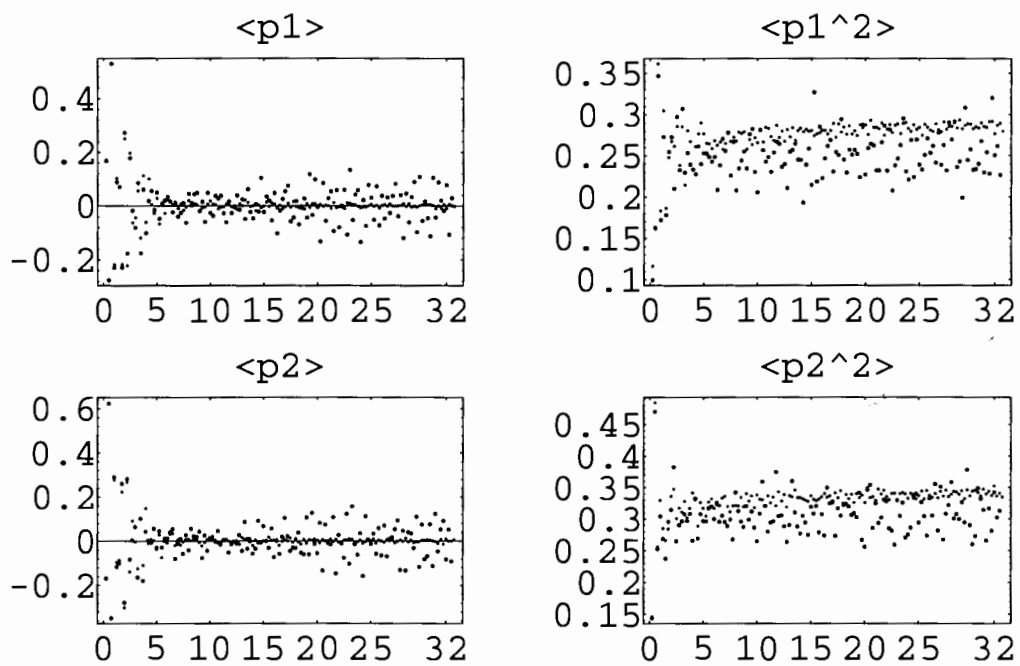


Figure 5.6: The momentum and momentum squared expectation values calculated for the same chaotic ensembles as in Figure 5.5.

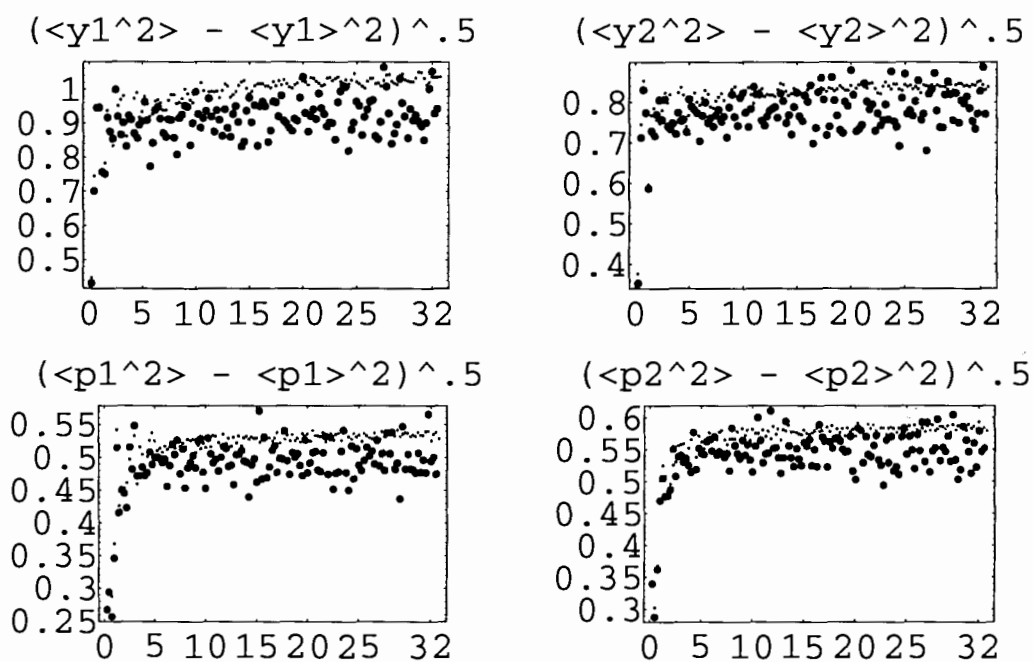


Figure 5.7: The standard deviations of position and momentum expectation values calculated for the same chaotic ensembles as in Figure 5.5. The large dots are the quantum values and the small dots are the classical ensembles.

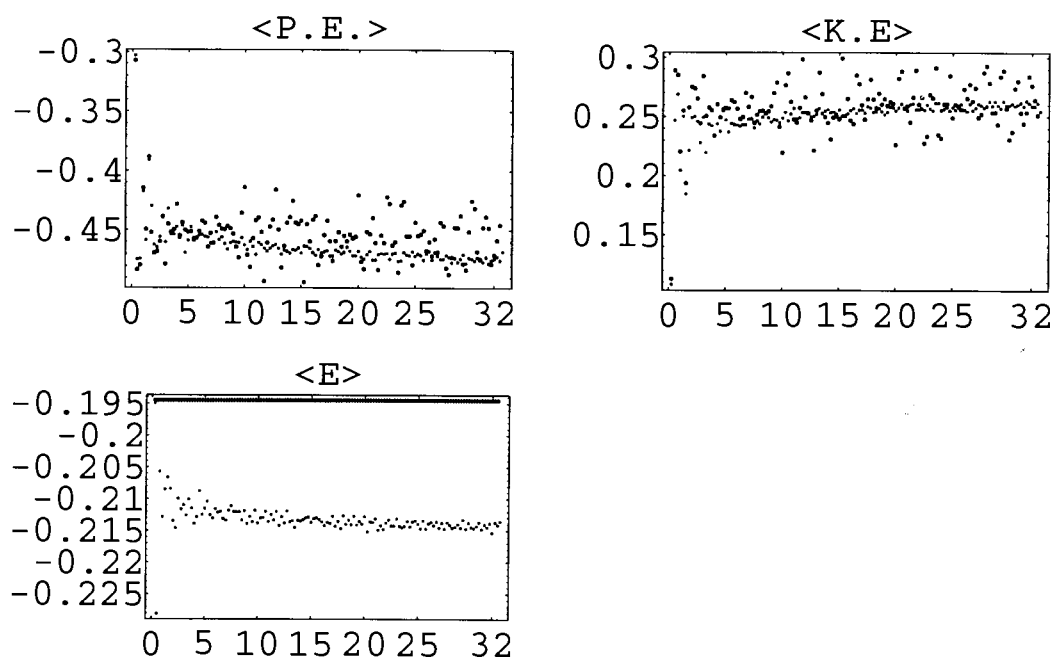


Figure 5.8: The expectation values for potential, kinetic, and total energy for the same chaotic ensembles as in Figure 5.5.

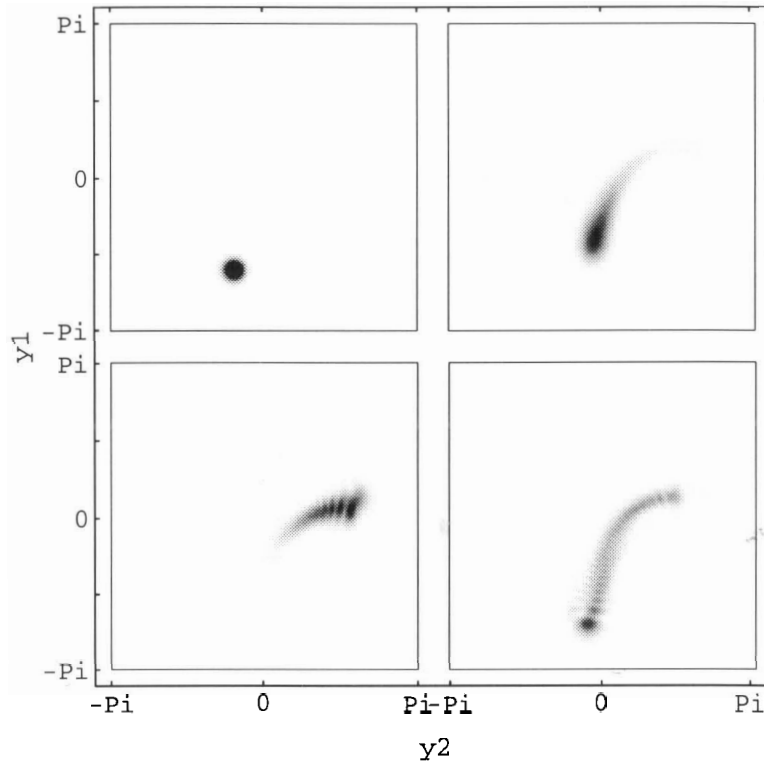


Figure 5.9: The probability distributions in position space for the quasiperiodic quantum ensemble centered at $(-2.0, -0.66)$. This is for time = 0, 1, 2, and 4 periods. The time ordering is from right to left and from top to bottom. The position expectation values are shown in Figure 5.1. The black represents .2 of the initial greatest probability. Zero probability is white. The same grey scale scheme is used for all the probability distributions in this chapter.

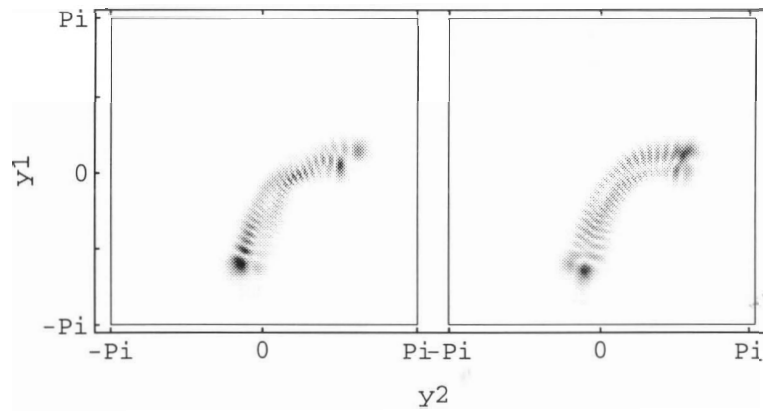


Figure 5.10: More probability distributions in position space for the quantum ensemble centered in the quasiperiodic regime at $(-2.0, -.66)$ This is for time = 10, and 32 periods. The position expectation values are shown in Figure 5.1.

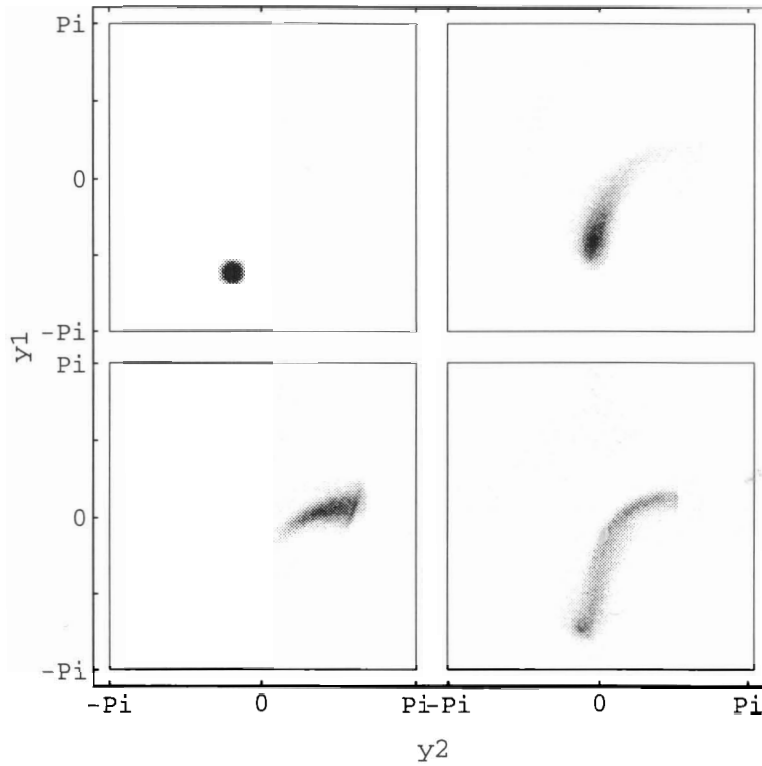


Figure 5.11: The probability distributions in position space for the classical ensemble centered in the quasiperiodic regime at $(-2.0, -0.66)$. This is for time = 0, 1, 2, and 4 periods. The position expectation values are shown in Figure 5.1.

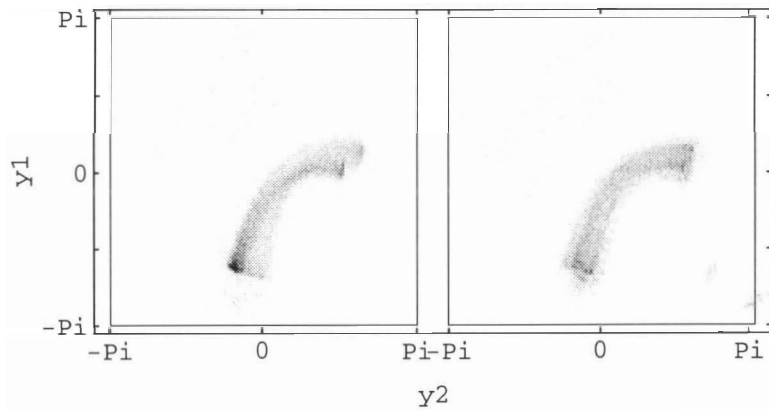


Figure 5.12: More probability distributions in position space for the classical ensemble centered at $(-2.0, -0.66)$ in the quasiperiodic regime. This is for time = 10, and 32 periods. The position expectation values are shown in Figure 5.1.

due to the exponential divergence of nearby trajectories in classical chaos. Both here and in the driven pendulum quantum mechanics was initially able to provide the same behaviour for its ensemble. In the coupled pendula system, both classical and quantum ensembles expanded out to the same limits in position and momentum.

For both cases computer time limited the number of periods to which the calculation could be made to thirty. Compared to the driven pendulum where the calculations were made up to 150 drive cycles it can be seen that this is a very short time. However, if both cases have reached a steady state—and unlike the driven pendulum at similar times, they give every indication that they have—then this short time is long enough.

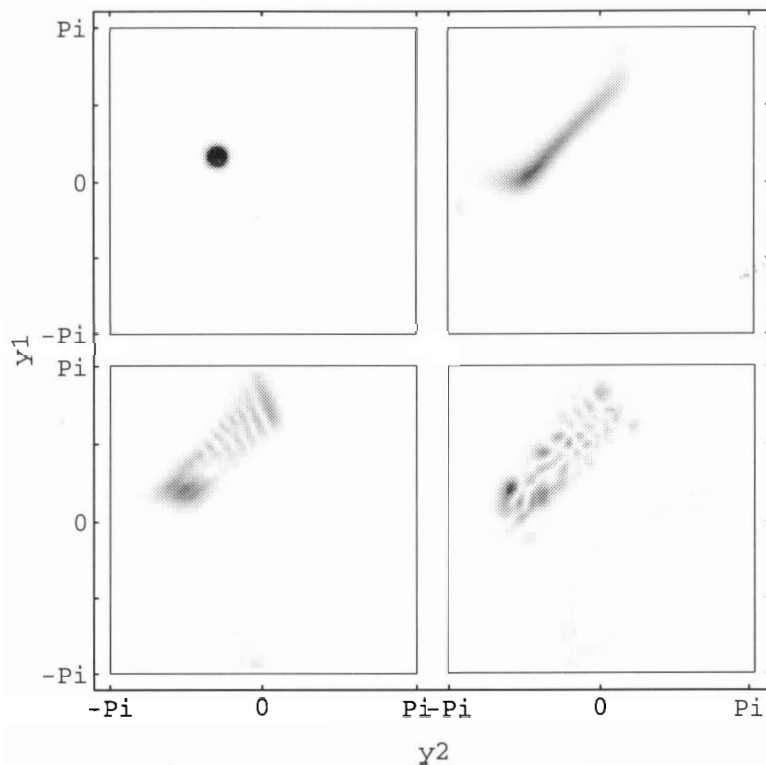


Figure 5.13: The probability distributions in position space for the quantum ensemble centered in the chaotic regime at $(.5, -1.5)$. This is for time = 0, 1, 2, and 4 periods. The time ordering is from left to right and from top to bottom. The position expectation values are shown in Figure 5.5.

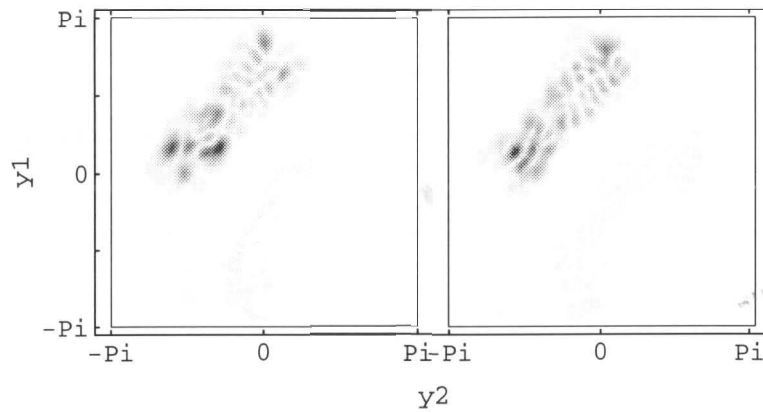


Figure 5.14: More probability distributions in position space for the chaotic quantum ensemble centered at $(.5, -1.5)$ Reading from left to right this is for time = 10 and 32 periods. The position expectation values are shown in Figure 5.5.

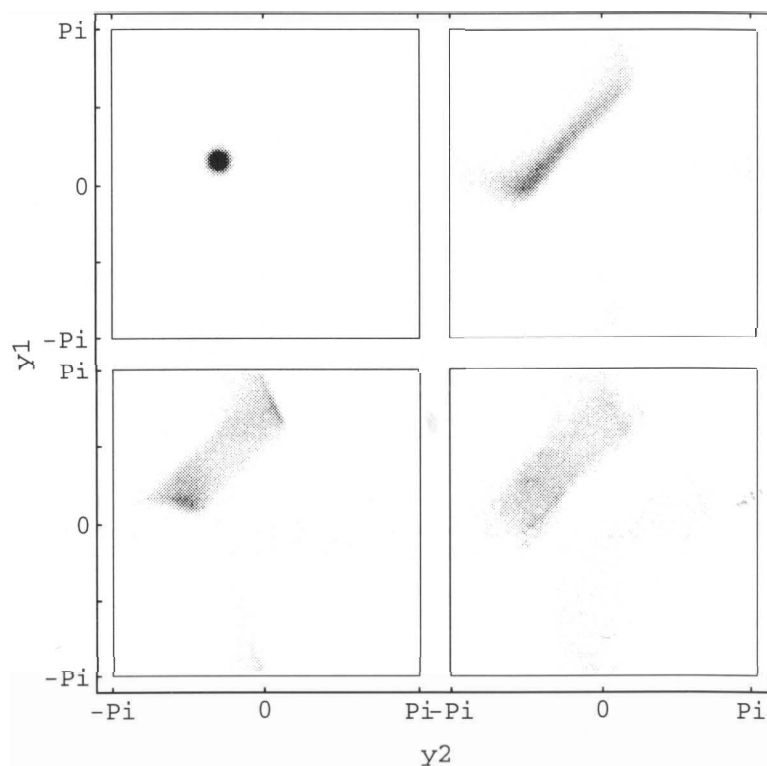


Figure 5.15: The probability distributions in position space for the chaotic classical ensemble centered at $(.5, -1.5)$. Reading from left to right and top to bottom, this is for time = 0, 1, 2, and 4 periods. The position expectation values are shown in Figure 5.5.

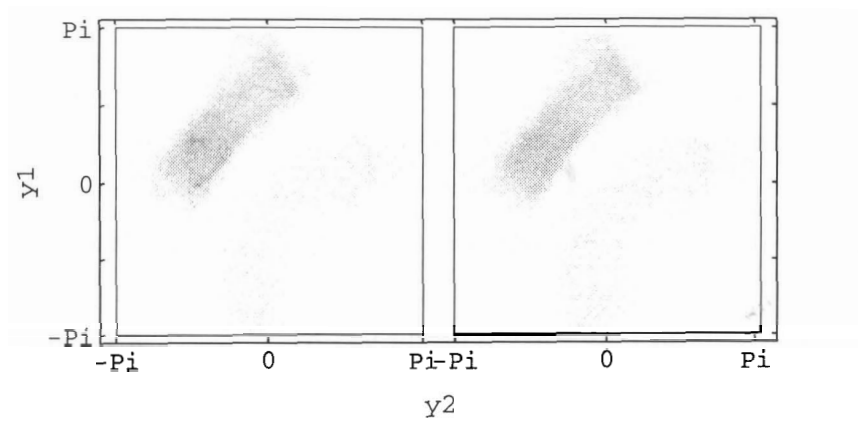



Figure 5.16: More probability distributions in position space for the classical ensemble centered at $(.5, -1.5)$ This is for time = 10, and 32 periods. The position expectation values are shown in Figure 5.5.

Chapter 6

Conclusion

 In this thesis, a comparison between quantum and classical mechanics was made for two systems whose classical behaviour can be chaotic. This was done to investigate the possibility of a disagreement between the predictions of the two theories in the classically chaotic regime. The comparison was made using numerical simulations, without recourse to taking limits such as \hbar going to zero. Instead, a dimensionless ratio, $c = \frac{m\ell^{3/2}g^{1/2}}{\hbar}$, of the physical constants of the system to \hbar was varied as an indication of how classical the system was.

The two systems studied were a driven pendulum and a pair of pendula joined by a spring. For these systems, the quantum and classical expectation values for a number of observables were computed, as were the probability distributions in phase space.

For the periodic regime of the driven pendulum, it was found that the theories agreed well for times up to 150 driving periods. This may be explained using Ehrenfest's theorem. Loosely, it states that if the width of the wavefunction (Δy) is sufficiently small compared to the length scale of variations in the potential then the centroid, $\langle y \rangle$, of the quantum ensemble will follow a classical trajectory.[38] The regular regimes of the classical driven pendulum consist of concentric regular trajectories in phase space. The members of the classical ensemble, including the centroid, must then follow these trajectories. The time evolution of $\langle y \rangle$ in both theories is then the same. The same argument may be made for $\langle p \rangle$ and thus for all the

functions of y and/or p . However, the agreement continues after the width of the distribution is large enough that Ehrenfest's theorem no longer applies.

Similar agreement between quantum and classical behaviour was found for initial conditions whose classical behaviour was chaotic, but only for times up to a few tens of driving periods. For short times of 10 periods or less, both classical and quantum ensembles grew rapidly in phase space, after which, interference effects dominated the quantum behaviour. This early agreement between the theories, while the ensembles are still spreading in phase space, is explained with the same reasoning as in the regular case. In this case also, the agreement continues beyond the time at which the ensembles are too wide for Ehrenfest's theorem to apply. This observation suggests the following generalization: For as long as the value of $\langle y \rangle$ continues to be a useful indication of the centre of a moving ensemble, the quantum and classical values will agree, even when this involves times beyond which Ehrenfest's theorem applies. This rapid growth of the ensembles followed by large scale interference, has been seen in a number of other systems.[6][2][10][17]

For longer times, it was found that the quantum system was limited to values in position and/or momentum that were lower than those in the classical system. A possible explanation was given in terms of the quasienergy expansion: the limits of the wavefunction in position and momentum must reflect similar limits of the quasienergy eigenfunctions which make up these wavefunctions.

The numerical methods used in this thesis were unable to determine the form of these eigenfunctions. The form of the eigenfunctions would have been useful for two reasons. The quantum evolution of wavefunctions is simple in the quasienergy expansion for periodically driven systems, thus knowledge of the eigenfunctions would have aided the numerical approach. The second use would be to determine the effect of chaotic dynamics on these eigenfunctions and on the classical equivalent of these eigenfunctions.

Quantum and classical mechanics differed in their predictions for the chaotic driven pendulum. The time at which the disagreements occurred was extended as c was increased and the system became more classical. This suggests that the disagreement occurs at longer and longer times as the system approaches the classical regime.

However, the largest value of c studied was only 250. The realm of everyday objects with dimensions of a single meter and masses of a kilogram has a value of $c = 10^{34}$. The realm of optically microscopic (a length of 1000nm, and a density of water) pendula occurs for $c = 10^{10}$. The results from this thesis are still far from the truly classical regime.

In the two-dimensional system, there was consistently good agreement between the quantum and classical analysis, both in the chaotic and the regular regimes. Several qualifications need to be made. The first is that the systems were run for less than thirty linear-pendulum periods. This was small compared to the 150 drive cycles for which the driven pendulum was run. Because of processing time, the value of c was kept very small so that the system was even closer to the quantum regime (by an order of magnitude) than the driven pendulum. Also because of the small value of c , the area of the Gaussians that were used was very large, thus removing the system even further from simulating a narrow classical ensemble. It is still very interesting to note how well, excepting interference, the classical ensemble mimics the behaviour of the quantum wavefunction this deep into the quantum regime. The predictions made by the two theories are represented by the expectation values and the probability distributions. The predictions of the two theories are nearly identical under these circumstances.

The last issue to be addressed is the question as to why the two theories agree so well in the chaotic regime for the coupled-pendula system and so poorly at long times in the chaotic regime for the driven-pendulum system. The least satisfying answer is to suggest that the short runs in the coupled-pendula case ended before the disagreements could appear. To explain the differences in quantum and classical behaviour in the chaotic driven pendulum as due to the quasienergy eigenfunctions that make up the wavefunction is only to rephrase the question without attempting to answer it. I do not know why the structure and extent of the quasienergy eigenfunctions should be limited as it was. This result may be tied to the difference between them and the energy eigenfunctions. In autonomous systems, the classical ensembles that are the equivalents to the quantum energy eigenfunctions are the trajectories of each energy. The equivalents to the eigenvalues are the classical energies. Similarly for the

quasienergy, the classical equivalents are the trajectories on the Poincaré section. The classical equivalent to the quasienergy itself is unknown. Solving this problem would go a long way to explaining what happens to the quantum quasienergy functions as the classical regime is approached, and perhaps suggest why the two theories disagree.

Bibliography

- [1] Eric J. Heller. Bound-state eigenfunctions of classically chaotic hamiltonian systems: Scars of periodic orbits. *Physical Review Letters*, 53(16):1515–1518, 1984.
- [2] K.M. Atkins and G.S. Ezra. Quantum-classical correspondence and the transition to chaos in coupled quartic oscillators. *Physical Review E*, 51(3):1822–1836, 1995.
- [3] Robert L. Waterland, Jian-Min Yanun, et al. Classical-quantum correspondence in the presence of global chaos. *Physical Review Letters*, 61(24):2733–2736, 1988.
- [4] Roderick V. Jensen. Quantum chaos. *Nature*, 355:311–318, 1992.
- [5] L.E. Ballentine, Yumin Yang, and J.P. Zibin. Inadequacy of Ehrenfest’s theorem to characterize the classical regime. *Physical Review A*, 50(4):2854–2859, 1994.
- [6] James P. Zibin. The Approach to Classical Chaos in an Anharmonic Quantum Oscillator. Master’s thesis, Simon Fraser University, 1995.
- [7] Mikito Toda. Phase retrieval problem in quantum chaos and its relation to the origin of irreversibility I. *Physica D*, 59:121–141, 1992.
- [8] L. Benet, T.H. Seligman, and H.A. Weidenmüller. Quantum signature of classical chaos: Sensitivity of wavefunctions to perturbations. *Physical Review Letters*, 71(4):529–532, 1993.
- [9] Martin C. Gutzwiller. *Chaos in Classical and Quantum Mechanics*. Springer-Verlag, Berlin, 1990.

- [10] B.S. Helmkamp and D.A. Browne. Structures in classical phase space and quantum chaotic dynamics. *Physical Review E*, 49(3):1831–1839, 1994.
- [11] B.S. Helmkamp and D.A. Browne. Inhibition of mixing in chaotic quantum dynamics. *Physical Review E*, 51(3):1849–1857, 1995.
- [12] Joseph Ford and Giorgio Mantica. Does quantum mechanics obey the correspondence principle? Is it complete? *American Journal of Physics*, 60(12):1086–1097, 1992.
- [13] Joseph Ford and Matthais Ilg. Eigenfunctions, eigenvalues and time evolution of finite, bounded, undriven quantum systems are not chaotic. *Physical Review A*, 45(9):6165–6173, 1992.
- [14] Joseph Ford, Giorgio Mantica, and Gerald H. Ristow. The Arnol'd cat: Failure of the correspondence principle. *Physica D*, 50:439–520, 1991.
- [15] Stefan Weigert. Quantum chaos in the configurational quantum cat map. *Physical Review A*, 48(3):1780–1798, 1993.
- [16] Ronald F. Fox and T.C. Elston. Chaos and a quantum-classical correspondence in the kicked top. *Physical Review E*, 50(4):2553–2563, 1994.
- [17] Ronald F. Fox and T.C. Elston. Chaos and the quantum-classical correspondence in the kicked pendulum. *Physical Review E*, 49(5):3683–3696, 1994.
- [18] Alexander Bobenko, Nadja Kutz, and Ulrich Pinkall. The discrete quantum pendulum. *Physics Letters A*, 177:399–404, 1993.
- [19] E. Eisenberg and N. Shnerb. Suppression of chaos, quantum resonance, and statistics of a nonintegrable system. *Physical Review E*, 49(2):R941–R944, 1994.
- [20] W.A. Lin and L.E. Ballentine. Quantum tunneling and regular and irregular quantum dynamics of a driven double well oscillator. *Physical Review A*, 45(6):3637–3645, 1992.

- [21] N. Ben-Tal, N. Moiseyev, and H.J. Korsch. Quantum versus classical dynamics in a periodically driven anharmonic oscillator. *Physical Review A*, 46(3):1669–1672, 1992.
- [22] N. Ben-Tal, N. Moiseyev, S. Fishman, and F. Bensch. Weak localization in a chaotic periodically driven anharmonic oscillator. *Physical Review E*, 47(3):1646–1649, 1993.
- [23] D.R. Grempel, R.E. Prange, and Shmuel Fishman. Quantum dynamics of a nonintegrable system. *Physical Review A*, 29(4):1639–1647, 1984.
- [24] D.L. Shepelyansky. Some statistical properties of simple classically stochastic quantum systems. *PhysicaD*, 8:208–222, 1983.
- [25] D.L. Shepelyansky. Localization of quasienergy eigenfunctions in action space. *Physical Review Letters*, 56(7):677–680, 1986.
- [26] Mikito Toda, Satoshi Adachi, and Kensuke Ikeda. Dynamical aspects of quantum-classical correspondence in quantum chaos. *Progress of Theoretical Physics Supplement*, (98):323–375, 1989.
- [27] T.P. Spiller and J.F. Ralph. The emergence of chaos in an open quantum system. *Physics Letters A*, 194:235–240, 1994.
- [28] R.H. Parmenter and L.Y. Yu. Quantum mechanics and deterministic chaos. *Physics Letters A*, 174(3):233–236, 1993.
- [29] Ya B. Zel’dovich. The quasienergy of a quantum-mechanical system subjected to a periodic action. *Soviet Physics JETP*, 24(5):1006–1008, 1967.
- [30] S.P. Hastings and J.B. Mcleod. Chaotic motion of a pendulum with oscillatory forcing. *American Mathematical Monthly*, 100(6):563–572, 1993.
- [31] *The NAG Fortran Library Manual—Mark 13*, 1988.
- [32] L.D. Landau and E.M. Lifshitz. *Mechanics*. Pergamon Press, 1976.

- [33] James A. Blackburn, H.J.T. Smith, and N. Grønbech-Jensen. Stability and Hopf bifurcations in an inverted pendulum. *American Journal of Physics*, 60(10):903–908, 1992.
- [34] M.D. Feit, Jr. J.A. Fleck, and A. Steiger. Solution of the Schrödinger equation by a spectral method. *Journal of Computational Physics*, 47:412–433, 1982.
- [35] L.E. Ballentine. The statistical interpretation of quantum mechanics. *Reviews of Modern Physics*, 42(4):358–381, 1970.
- [36] K. Husimi. *Proceedings of the Physico-mathematical Society of Japan*, 22:264, 1940.
- [37] S.B. Lee and M.D. Feit. Signatures of quantum chaos in Wigner and Husimi representations. *Physical Review E*, 47(6):4552–4555, 1993.
- [38] Leslie E. Ballentine. *Quantum Mechanics*. Prentice-Hall, Inc., Toronto, 1990.